Contributions to a
Yb$^+$ Single-Ion Optical Frequency Standard

Von der Fakultät für Mathematik und Physik

der Gottfried Wilhelm Leibniz Universität Hannover

zur Erlangung des Grades

Doktor der Naturwissenschaften

Dr. rer. nat.

genehmigte Dissertation

von

Dipl.-Phys. Björn Stein

geboren am 28.01.1979 in Salzgitter

2010

Meinen Eltern Erika und Siegfried
sowie meinem Bruder Hagen

Kurzzusammenfassung

Eine Paulfalle in zylindrischer Endkappengeometrie mit geplanter Brechung der Radialsymmetrie wird vorgestellt. Die Speicherung von einzelnen Ytterbiumionen und Ionenwolken wird gezeigt. Die Falle wird hinsichtlich Quadrupolstärke, Mathieuparametern und Säkularfrequenzen charakterisiert.

Der Einfluß von streufeldkompensierenden Elektroden wird untersucht. Die Kompensation des Dipolstreufeldes kann zur Erzeugung statischer Quadrupolfeldern von mehr als $1\,\mathrm{V/mm^2}$ führen, die für Präzisionsspektroskopie problematisch sind. Eine Geometrie sich gegenüberstehender Kompensationselektroden entschärft diese Problematik.

Die Harmonizität des Wechselspannungsfallenpotentials wird durch Suche nach einer Amplitudenabhängigkeit der Säkularfrequenzen von Ionenwolken geprüft. Die Ist-Abmessungen der Falle lassen eine Duffingoszillation erwarten. Experimentelle Daten zeigen qualitativ das erwartete Verhalten. Quantitative Übereinstimmung zwischen Theorie und Experiment wird nur mit Fitparametern ausserhalb bekannter Rahmenbedingungen erzielt.

Ferner wird die durch Verwendung von Gauß-Hermite-Moden erzielbare Verringerung des auf Brownsche Bewegung zurückgehenden thermischen Rauschens von ULE-Resonatoren untersucht. Die bekannte, aber bisher nur auf rotationssymmetrische Moden angewandte Theorie wird vorgestellt. Sowohl relative Skalierungsfaktoren als auch Absolutwerte des Rauschens für in optischen Uhren einesetzten ULE-Resonatoren wird berechnet. Eine $\mathrm{TEM}_{30,30}$-Mode enthält demnach 14 % der im Spiegelsubstrat und 7 % der in der Spiegelbeschichtung entstehenden Rauschleistungsdichte der fundamentalen Gaußschen Mode.

Die Erzeugung von Gauss-Hermite-Moden aus einer fundamentalen Gaußschen Mode mittels eines räumlichen Modulators für Licht (spatial light modulator). Die erzeugten Moden werden mit einem optischen Resonator analysiert. Die selektive Anregung einer $\mathrm{TEM}_{18,0}$- und einer $\mathrm{TEM}_{4,3}$-Mode wird gezeigt. Die Wiedergabetreue als Verhältnis der optischen Leistung in der gewünschten Resonatormode zur Gesamtleistung aller angeregten Resonatormoden ist in beiden Fällen etwa 90 %. Ein Vorgehen zum Verringern ungewünschter Modenbeimischung wird anhand einer $\mathrm{TEM}_{8,8}$-Mode demonstriert.

Stichworte:

- Ionenfalle

- Thermisches Rauschen

- Frequenzstabilisierung

Abstract

A quadrupole ion trap in the cylindrical endcap geometry with intentional radial symmetry breaking is presented. Trapping of single Ytterbium ions and of ion clouds is demonstrated. The trap is characterised in terms of quadrupole strength, Mathieu parameters, and secular frequencies.

The influence of stray-field compensating electrodes is investigated. It is found that compensating the stray dipole field can cause static quadrupole fields exceeding 1 V/mm^2, which are a concern in precision spectroscopy. A geometry of opposing compensation electrodes mitigates this problem.

The harmonicity of the AC trapping potential is tested by searching for an amplitude dependence of secular frequencies in ion clouds. From the trap's measured actual dimensions, a Duffing oscillation is expected theoretically. Experimental data matches this prediction qualitatively. Quantitative agreement is obtained only with fit parameters outside known constraints.

Further, the reduction in the Brownian motion thermal noise of ULE resonators achievable by using high-order Gauss-Hermite modes is investigated. Known calculation methods, previously only applied to rotationally symmetric modes, are presented. Both the relative scaling factors with mode indices and the absolute value of Brownian motion noise for ULE resonators used in optical clock experiments are calculated. A $\text{TEM}_{30,30}$ mode is found to carry 14 % of the substrate-originating, and about 7 % of the coating-originating power spectral noise of the fundamental Gaussian mode.

The generation of Gauss-Hermite modes from a fundamental Gaussian mode using a spatial light modulator is demonstrated. The generated modes are analysed in an optical resonator. The selective excitation of a $\text{TEM}_{18,0}$ and a $\text{TEM}_{4,3}$ mode is demonstrated. The fidelity as ratio of the power in the desired resonator mode to the power in all resonator modes is about 90 % in both cases. A scheme to reduce undesired mode content is demonstrated in a $\text{TEM}_{8,8}$ mode.

Key words:

- Ion trap

- Thermal noise

- Frequency stabilisation

Contents

Contents

List of Figures

List of Figures

x

List of Tables

Acknowledgements

1 Introduction

The art of timekeeping has had a profound impact on science and civilisation from prehistoric times to the present day. Early sun dials and astronomically aligned edifices such as Stonehenge are examples of Neolithic devices suitable for measuring and keeping track of time on a daily or a seasonal timescale. Early break-through innovations in clock design, such as the Chinese water clock and the Egyptian sand clock, have already been achieved thousands of years ago.

Driven largely by the demands of navigation, communication and science, the art of timekeeping has far surpassed the measuring accuracy achieved for all other SI units. Today, the most accurate primary clocks, frequency standards based on a microwave transition in Caesium, can measure the passage of time to a relative accuracy of better than 10^{-15}. This corresponds to an error of less than one cycle of the microwave transition frequency per day.

In achieving this remarkable level of accuracy, the internal oscillation period of clocks has increased from the diurnal or annual periods of astronomical observations to the microwave transition frequency of Caesium clocks. A natural next step is to increase this frequency further. During the past ten years, the use of optical transition frequencies in precision measurements has been greatly facilitated by the invention of the frequency comb, replacing elaborate frequency chains for coherently linking microwave and optical frequencies with a commercially available device.

1.1 Operating Principle of Current Frequency Standards

A modern frequency standard consists of an oscillator, an atomic reference, and a locking mechanism to keep the oscillator running on a frequency defined by the atomic reference. This frequency is the output of the frequency standard. Measurements are comparisons between this and another frequency source. As such a comparison may contribute a significant uncertainty, the comparison mechanism, which may involve frequency dividers, mixers and counters, should be considered part of a clock. If the frequency comparison is omitted (or made to a zero frequency), the counter's output is that traditionally associated with a clock, namely the elapsed time in units of the period associated with the atomic transition frequency. A general schematic of such a frequency standard is shown in Figure 1.1.

Apart from technical qualities such as reliability and cost, the quality of a frequency standard can largely be described by two quantities, its stability and its accuracy. These qualities are illustrated in Figure 1.2. The accuracy is the relative systematic difference between the mean output frequency and the true atomic reference frequency. The effects limiting accuracy include a conceivable locking offset and systematic errors such as Stark
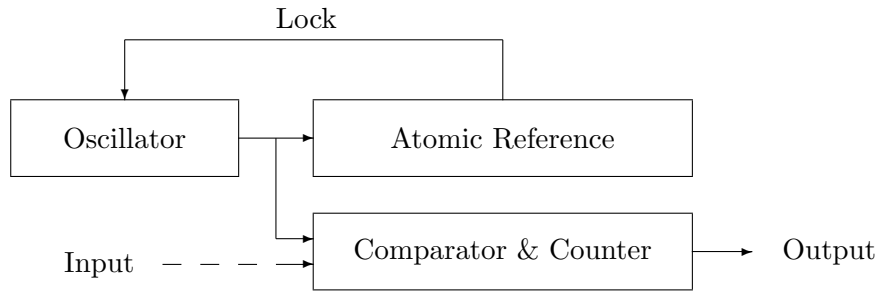
Figure 1.1: General schematic of a frequency standard. For a frequency comparison the complete setup must include a measurement input and an output for the measurement result. The everyday concept of a clock is recovered if no input (or a frequency of zero) is applied and a counter (divisor) setting for producing a one Hz output frequency ("second tick") is chosen.

and Zeeman shifts on the atomic transition. The stability is determined by statistical fluctuations of the output frequency. It is influenced by noise in the oscillator and the lock, including the interrogation of the atomic reference.

1.1.1 Microwave Frequency Standards

In a Caesium clock, the oscillator is a microwave source. The atomic reference is a hyperfine transition in Caesium atoms. Traditionally, the oscillator at the 9.192631770 GHz transition frequency is based on a quartz resonator at approximately 5 MHz as this technology and frequency results in the lowest purely electronically achievable relative frequency noise in the free running oscillator. Recently, the use of microwaves derived from optical clock resonators, to be explained later, as oscillator with even lower noise was demonstrated (Weyers et al., 2009).

The hyperfine transition is traditionally probed in a thermal beam of atoms. Before passing through the microwave interaction region, the atoms are state-selected by magnetic deflection. The detection is traditionally also done in this manner. Alternatively, state-preparation and detection can be performed by optical spectroscopy. By additionally replacing the atomic beam with magneto-optically cooled Caesium clouds periodically injected vertically through a microwave interaction region (for a double-pass during upwards and downwards travel), the most advanced form of Caesium clocks, the Fountain clock, is realized.

Microwave clocks can be based on other species. These either operate analogously to a Caesium clock (such as Rubidium clocks) or incorporate the oscillator at least partially into the atomic reference, such as the hydrogen maser.

Low Stability   High Stability

Low Accuracy
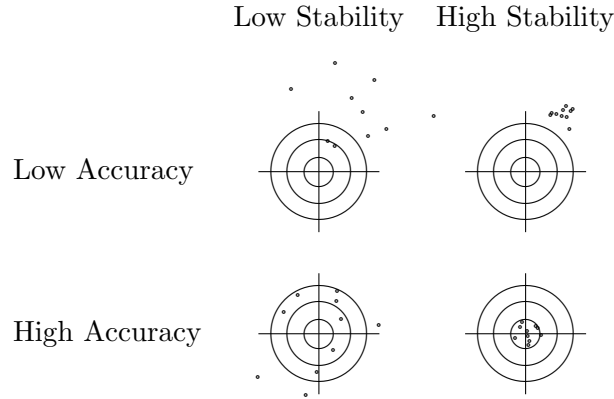
High Accuracy

Figure 1.2: Stability and accuracy. A stable measurement has low deviation, like a rifle achieving low shot-to-shot deviation. This is regardless of accurately reproducing the measured quantity. A high measurement accuracy corresponds to a rifle's shot being on aim, regardless of its shot-to-shot deviation. As in a rifle, in a clock both stability and accuracy is sought.

1.1.2 The Appeal of Optical Frequency Standards

A frequency standard operated with periodic interrogations of an atomic reference ideally achieves a fractional instability of (Santarelli et al., 1999; Weyers et al., 2009)

$$\sigma_y(\tau) = \frac{1}{\pi} \frac{1}{Q} \frac{1}{S/N} \sqrt{\frac{T}{\tau}} \tag{1.1}$$

after a measurement (averaging) time τ. Here the instability is given as Allan deviation, a common measure to be used again and briefly introduced in Section 3.3.3. The reference transition's quality factor $Q = \nu/\Delta\nu$ is the ratio of transition frequency ν to effective linewidth $\Delta\nu$, which is at best the Fourier limit for the period T of an interrogation cycle. Finally, the achievable frequency depends on the signal-to-noise ratio S/N. Assuming no squeezing, quantum projection noise (Itano et al., 1993) leads to a signal-to-noise ratio that scales with the inverse square root of the number of atoms probed.

The instability, as given in Eq. (1.1), is most effectively reduced by the choice of a high transition frequency ν. Using optical as opposed to microwave frequencies, an improvement of the instability at a given measurement time of up to five orders of magnitude over Caesium clocks can be envisioned. The implicit assumption is that the effective linewidth $\Delta\nu$ is not increased. As a highly forbidden optical transition can be used, the natural linewidth, ranging from Hz down to nHz in experimentally investigated clock transitions, need not be a practical limitation. The true limitation to a low $\Delta\nu$ in optical frequency standards is the difficulty of providing a low-noise (and hence small linewidth) oscillator, or clock reference laser, at this frequency.

Single-ion Optical Frequency Standards

Obtaining a high accuracy from an optical frequency standard requires that the atomic reference is not disturbed by the environment. A single ion trapped in quadrupole traps is one such ideal system (Dehmelt, 1981), because the ion can be localised in a field-free region in free space. Laser cooling allows a reduction of the ion's motion and hence the Doppler effect. In principle, it can be eliminated entirely by ground-state cooling.

Using only a single ion as atomic reference also incurs a drawback in signal-to-noise ratio, which can become unity at best. The signal-to-noise ratio can be improved upon by using many atoms or ions. To maintain high accuracy, the mutual effect upon each other must be minimized. This is difficult with ions due to their strong Coulomb interaction.

Lattice Clocks

Atoms can be stored in an optical lattice formed by a standing laser wave, essentially free of interaction with other atoms. But the standing light wave leads to an intensity-dependent frequency shift, which is wavelength-dependent. It can be arranged to use a "magical" wavelength that causes zero frequency shift (to first order in intensity), as proposed by Katori et al. (2003).

1.2 Scope of this Thesis

This thesis is divided into two further chapters. Chapter 2 details the design and the characterisation of an optimised quadrupole ion trap geometry. The role of the ion trap in a single-ion frequency standard is to sufficiently isolate the ion from environmental effects to limit systematic frequency shifts whilst reliably storing it to enable continuous operation of the frequency standard. In particular, the heating rate of the ion should be kept low, which is advantageous for two reasons. Firstly, laser cooling is impossible during the interrogation of the clock transition. Secondly, a low heating rate leads to a high storage time, limiting the number of times a new ion has to be loaded into the trap. As loading an ion into the trap may require significant atomic vapour pressure, it has the undesirable side effect of coating the surfaces of the trap and the vacuum system. Departures from the ideal quadrupole potential are unnecessary for trapping and could be avoided.

Chapter 3 addresses a current limitation in optical clocks, the thermal noise in the clock reference laser. This noise arises in the pre-stabilisation (before the lock shown in Figure 1.1) to a passive optical resonator with mirrors undergoing thermally driven Brownian motion. Figure 1.3 illustrates the generic setup. Locking to a reference resonator has been demonstrated at the mHz level (Salomon et al., 1988), yet clock lasers are far from achieving a correspondingly low linewidth (e.g., Young et al., 1999; Sherstov et al., 2010). For the usual choice of a fundamental Gaussian resonator mode, this discrepancy has been explained quantitatively by Brownian motion (Numata et al., 2004a). I calculate the noise reduction achievable by employing high-order Gauss-Hermite modes and demonstrate the selective excitation of such modes.
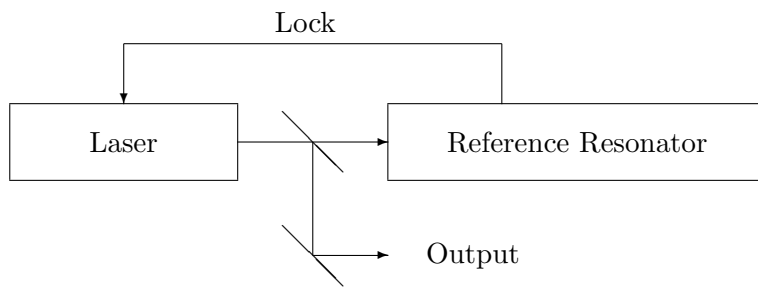
Figure 1.3: Generic clock reference laser setup. A laser, usually an external cavity diode laser or a dye laser, is locked to a reference resonator.

2 Paul Trap with reduced Anharmonicity

Earnshaw Theorem

Confining an ion with electrostatic forces alone is impossible: the ion must move in a charge-free region. The externally generated electric potential Φ thus conforms to the Laplace equation

$$\frac{\partial^2}{\partial x^2}\Phi + \frac{\partial^2}{\partial y^2}\Phi + \frac{\partial^2}{\partial z^2}\Phi = 0. \tag{2.1}$$

Confinement of a charge q in all spatial directions requires restoring spring constants

$$k_x = q\frac{\partial^2}{\partial x^2}\Phi > 0, \qquad k_y = q\frac{\partial^2}{\partial y^2}\Phi > 0, \qquad k_z = q\frac{\partial^2}{\partial z^2}\Phi > 0 \tag{2.2}$$

in all spatial directions, a contradiction to Eq. (2.1). Earnshaw (1842) advanced this argument to exclude pure $1/r$ potentials for a stable arrangement of constituent particles, as observed in matter or then assumed for a hypothetical ether. It is now known as "Earnshaw theorem."

Quadrupole Trap

A solution for confining an ion is to use an alternating electric field. This puts the charge q in a ponderomotive potential

$$U_P = \frac{q^2}{4m\Omega^2}\left(\nabla\Phi_{\text{peak}}\right)^2. \tag{2.3}$$

To satisfy the condition Eq. (2.2) applied to the ponderomotive potential U_P, the magnitude of the electric field, $|-\nabla\Phi|$, must grow in all directions away from the point where the ion shall be stored. There the corresponding ponderomotive potential U_P has a minimum. The lowest order electric multipole fulfilling this requirement is the quadrupole. The quadrupole trap was invented by Paul et al. (1958); see also Paul (1990).

Organisation

I first elaborate on the theory of quadrupole traps in the ensuing Section 2.1. Others (Straubel, 1955; Schrama et al., 1993) have modified Paul's quadrupole trap design for better optical access. I introduce a design in Section 2.2 that addresses the drawback incurred in Schrama's endcap design, a higher multipole content of the trap, at the penalty of a further reduction of the quadrupole strength. This design was built. Its

experimental characterisation is described in Section 2.3. A signature of higher multipole content is expected in the resonance lineshape of secular motion. The investigation of this lineshape in Section 2.4 concludes this chapter.

2.1 Theory

This theory-laden section first presents the properties of an idealised quadrupole trap in Section 2.1.1. Since, for early traps, much attention had been paid to creating as perfect a quadrupole field as possible, this discussion can also be considered a treatment of the traditional Paul trap design. In this sense I follow history as I turn to imperfections of the trapping field in Section 2.1.2 on page 10. Consequences for ion motion are addressed in the pseudopotential approximation, to which Section 2.1.3 on page 12 is devoted.

2.1.1 The Ideal (Traditional) Paul Trap

Paul's trap design using hyperbolic electrodes produces the electric potential

$$\Phi(V_t) = 2a_{20}\left(\frac{1}{2} + \frac{1}{2}\left(\frac{z}{z_0}\right)^2 - \frac{1}{4}\left(\frac{r}{z_0}\right)^2\right)V_t. \tag{2.4}$$

in cylinder coordinates (r, z) with axial electrode separation $2z_0$, where the radial electrode is grounded and a voltage V_t is applied to both axial electrodes. The quadrupole coefficient $2a_{20}$ is unity for this geometry; keeping it simplifies the transition to other trap geometries in Section 2.1.2. For operation as a trap, the applied voltage is

$$V_t = U + V \cos\ \Omega t \tag{2.5}$$

Equation of Motion

The equation of motion of the ion can be separated into independent axial and radial parts, each of which is

$$\frac{\partial^2 x}{\partial \tau^2} + (a - 2q\cos 2\tau)\,x = 0 \tag{2.6}$$

with $\tau = t\Omega/2$ and appropriate parameters a and q. These differ for radial (index r) and axial (index z) directions:

$$q_z = -2q_r = -4a_{20}\frac{e}{mz_0^2\Omega^2}V, \tag{2.7a}$$

$$a_z = -2a_r = 8a_{20}\frac{e}{mz_0^2\Omega^2}U. \tag{2.7b}$$

Sign and appearance of these equations differ from the usual convention (e.g., March and Todd, 1995). The sign differs because I express the potential given by Eq. (2.4) for both AC and DC voltages applied to the same (axial) electrodes. The same physical situation naturally retains the same set of $|q|$, a parameters, where the sign of q can be freely
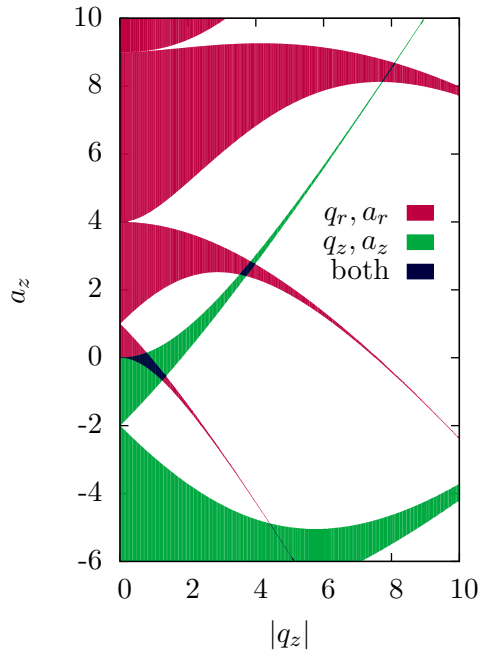
Figure 2.1: Stability diagram. Regions of q_z, a_z parameters are shaded where stable solutions exist for the radial motion (with Mathieu parameters $q_r = -q_z/2$, $a_r = -a_z/2$), for the axial motion (q_z, a_z) and for both.

chosen due to the invariance of Eq. (2.6) under the transform $q \to -q$, $\tau \to \tau - \pi/2$ (choosing the opposite polarity and half a period delay for the AC voltage results in the same physical situation). I have further expressed q and a parameters in terms of the axial half-electrode spacing z_0 instead of the radial one, such that Eq. (2.7) can be applied to a trap geometry that lacks a radial ring electrode in Sections 2.2 and 2.3.

The Mathieu equation, Eq. (2.6), arises in a multitude of physical problems. It was first treated by Mathieu (1868) and its solution has since been discussed in great detail (Horn, 1905; McLachlan, 1951; Meixner and Schäfke, 1954; Abramowitz and Stegun, 1972, and many others). For the purpose of this thesis, only a few general properties of the solution are needed, which are summarised in books on ion trapping, e.g., March and Todd (1995); Major et al. (2005).

Bound Ion Solution

The Mathieu equation has periodic solutions only for certain regions of the parameter space (q, a). Both (q_r, a_r) and (q_z, a_z) must lie in such a region for an ion to be trapped. The stability diagram of Figure 2.1 comprises some of these stability regions. The

periodic solution can be written as:

$$x(\tau) = \sum_{n=-\infty}^{+\infty} C_n \exp\left(-\imath \frac{1}{2}(2n+\beta)\,\tau\right) + \text{c.c.}, \tag{2.8a}$$

$$\beta^2 = a + \cfrac{q^2}{(\beta+2)^2 - a - \cfrac{q^2}{(\beta+4)^2 - a - \cdots}} + \cfrac{q^2}{(\beta-2)^2 - a - \cfrac{q^2}{(\beta-4)^2 - a - \cdots}}, \tag{2.8b}$$

$$\frac{C_{n\pm1}}{C_n} = -\cfrac{q^2}{(2 \mp 0 + \beta)^2 - a - \cfrac{q^2}{(2n \mp 2 + \beta)^2 - a - \cfrac{q^2}{(2n \mp 4 + \beta)^2 - a - \cdots}}}. \tag{2.8c}$$

Traps for single ion storage usually operate in the $|q|, a \ll 1$ regime where the C_0 term is large compared to all other C_n. The motion associated with the C_0 term has the lowest frequency and is called secular motion. The smaller remaining motion at higher frequency is then, by amplitude, dominated by the C_1 term and called micromotion. The secular frequencies are

$$\omega_r = \frac{1}{2}\beta_r\Omega \approx \frac{1}{2}\Omega\sqrt{\frac{1}{2}q_r^2 + a_r} \qquad \text{and} \qquad \omega_z = \frac{1}{2}\beta_z\Omega \approx \frac{1}{2}\Omega\sqrt{\frac{1}{2}q_z^2 + a_z}. \tag{2.9}$$

The approximations are valid for $|q|, |a| \ll 1$. Their fractional error is less than 5 % for $|q_z| \le 0.4$ and $-0.2\,q^2 \le a \le 0.4\,q^2$, which only excludes a_z parameters close to the boundaries of stability at $a_z \approx -0.25\,q_z^2$ and $a_z \approx 0.5\,q_z^2$.

2.1.2 Imperfect Quadrupole Traps

No physical realization can be perfect. For the traditional Paul trap with hyperbolic electrodes, an obvious departure from this mathematical shape is necessary because the difference in the electric potential requires a minimum separation whereas the design calls for an asymptotical touching. In practice, significant departures from the hyperbolic shapes are often made to facilitate the fabrication and to enlarge the optical access to the trapping region (e.g., Beaty, 1986b) or even specifically to create desired deviations from the pure quadrupole field (e.g., Syka, 1995).

These intentional deviations from the electrically perfect electrode geometry alter the electric potential inside the trap. In this section, I lay a foundation for quantifying these imperfections.

Electric Potential

Eq. (2.4) contains a quadrupole term $V_t(2z^2 - r^2)/4$ and a constant term $V_t/2$. Other electrode geometries will, in general, also produce other multipole potentials to some

extent. An interior spherical multipole expansion of the trap potential $\Phi(V_t)$ in spherical coordinates r, θ, ϕ with the trap centre at the origin yields

$$\Phi(V_t) = V_t \sum_{l=0}^{\infty} \sum_{m=-l}^{l} a_{lm} \, A_{lm}(r, \theta, \phi),$$
$$A_{lm}(r, \theta, \phi) = \sqrt{\tfrac{4\pi}{2l+1}} \left(\tfrac{r}{z_0}\right)^l Y_{lm}(\theta, \phi). \tag{2.10}$$

This is valid for locations (r, θ, ϕ) inside the electrodes' surface charge distribution with $(2l)$-pole moment $I_{lm} = 4\pi \, \epsilon_0 \, V_t \, a_{lm}$. This situation is different from the more commonly encountered exterior spherical multipole expansion, which describes the potential outside of a bounded charge distribution; hence the radial dependence is r^l rather than r^{-l-1}. For the spherical harmonics Y_{lm}, the usual complex-valued choice in quantum mechanics, $Y'_{l,m} = N_{lm} e^{im\phi} P_{ml}(\cos\,\theta)$, is not convenient here. Instead, I use the real-valued spherical harmonics

$$Y_{lm} = \begin{cases} Y'_{0,0} & m = 0 \\ 2^{-1/2} \left(\quad Y'_{l,m} + \ (-1)^m \, Y'_{l,-m} \right) & m > 0 \\ 2^{-1/2} \left(-\imath Y'_{l,m} + \imath \, (-1)^m \, Y'_{l,-m} \right) & m < 0. \end{cases} \tag{2.11}$$

Symmetries

Minimising many undesired multipoles in the trap potential can be achieved by choosing an appropriately symmetrical electrode geometry. Plane symmetry defines a trap axis along the plane's normal direction. I will refer to the symmetry plane as radial plane. In a spherical coordinate system with the trap axis as polar axis, this symmetry is only met by multipoles A_{lm} with an even sum $l + m$.

Inversion symmetry about the origin, when present additionally to the radial plane symmetry, results in a further inversion symmetry about the trap axis. This implies a periodicity at every half turn about the trap axis (180° in azimuth angle ϕ), met by multipoles with even m.

Any additional symmetry plane perpendicular to the radial plane must contain the trap axis because of the inversion symmetry. In a coordinate system where the new symmetry plane has an azimuth angle $\phi = 0$, the trap's potential is an even function of the azimuth angle. The consequence depends on the choice of spherical multipole functions. For the common complex-valued $Y'_{l,m}$, it follows that $a'_{l,m} = a'^{\dagger}_{l,-m}$. For my choice of real-valued spherical harmonics $Y_{l,m}$, it restricts m to be non-negative.

All trap designs mentioned in this thesis fulfil all of above-mentioned symmetries, as they have identical upper and lower electrodes (inversion symmetry at proper alignment) with additional plane symmetries. The following selection rules for non-zero coefficients a_{lm} result:

$$l, m \text{ even},$$
$$m \geq 0. \tag{2.12}$$

Many trap designs are further rotationally symmetric about the trap axis. For these, only the $m = 0$ terms do not vanish.

2.1.3 Pseudopotential

For many purposes, describing the exact motion of an ion in a Paul trap is unnecessarily complicated. It is then helpful to ignore micromotion on the timescale of the driving frequency Ω and only consider secular motion. The effective potential created by the driving potential $\Phi(V \cos \Omega t)$ is the ponderomotive potential

$$U_P(V, \Omega) = \frac{e^2}{4m\Omega^2} \left(\nabla \Phi(V)\right)^2. \tag{2.13}$$

Together with the static electric potential $\Phi(U)$, the effective potential seen by the ion is the pseudopotential

$$U_{\text{eff}} = U_P(V, \Omega) + e\,\Phi(U). \tag{2.14}$$

Pure Quadrupoles

A trap containing only the quadrupole terms a_{20} and a_{22} creates the electric potential, in Cartesian coordinates (x, y, z):

$$\Phi_2(V_t) = \frac{a_{20}}{2z_0^2} \left(2z^2 - (1-\epsilon)\,x^2 - (1+\epsilon)\,y^2\right) V_t, \qquad \epsilon = \sqrt{3}\,\frac{a_{22}}{a_{20}}. \tag{2.15}$$

The resulting pseudopotential for a singly charged, positive ion of mass m is

$$
\begin{aligned}
U_{\text{eff},2} = \quad & \frac{a_{20}}{z_0^2} \frac{eU}{2} \left(2z^2 - (1-\epsilon)\ x^2 - (1+\epsilon)\ y^2\right) \\
+ & \frac{a_{20}^2}{z_0^4} \frac{e^2 V^2}{4m\Omega^2} \left(4z^2 + (1-\epsilon)^2\, x^2 + (1+\epsilon)^2\, y^2\right).
\end{aligned}
\tag{2.16}
$$

This is a harmonic potential

$$U_{\text{eff},2} = \sum_{\xi \in \{x,y,z\}} \frac{m}{16\Omega^2} \left(q_\xi^2 - 2a_\xi\right)\xi^2, \qquad q_{x,y} = q_r\left(1 \mp \epsilon\right), \qquad a_{x,y} = a_r\left(1 \mp \epsilon\right), \tag{2.17}$$

causing uncoupled motion along each of the Cartesian coordinate axes with resonance frequencies

$$\omega_{x,y,z} = \frac{1}{2}\Omega\sqrt{\frac{1}{2}q_{x,y,z}^2 + a_{x,y,z}}. \tag{2.18}$$

Comparing to Eq. (2.9), the pseudopotential picture turns out to be the approximation of truncating the continued fraction of Eq. (2.8b) in the first denominator such that $\beta \approx \sqrt{q_{x,y,z}^2/2 + a_{x,y,z}}$.

Perturbation by Dipoles

The dipole terms $a_{1m}A_{1m}$ vanish for a trap with plane symmetries about Cartesian axes. Even if manufacturing tolerances disturb these symmetries, dipole terms have no practical influence. They describe a constant electric field (gradient of the potential), which vanishes for an ion stored at the potential minimum. To reflect this in the multipole

expansion, the origin for the expansion must be chosen to be at the true minimum of the potential.

Beaty (1986b) points out both this mathematical change of origin and the option to modify the ratio of driving voltages for upper and lower electrodes to zero the dipole terms in realizations of trap designs. The former approach technically modifies the calculated higher-order multipoles, but small manufacturing deviations imply small modifications. The latter approach can be used to zero the axial a_{10} dipole, but not simultaneously possible radial $a_{0\pm1}$ dipoles.

To experimentally have an ion indeed stored at the minimum of the potential produced by the trap electrodes, no net additional forces may act on it. This implies that stray electric fields—those not proportional to the voltage applied to the trap's electrodes—must be compensated by externally generated fields.

Perturbation by Higher Multipoles

The lowest-order departure from the quadrupole pseudopotential Eq. (2.16) caused by a multipole term $a_{lm}A_{lm}$ can be deduced from the radial dependence of A_{lm} defined in Eq. (2.10). The static potential $e\,\Phi(U)$ directly inherits its r^l dependence, whereas for the ponderomotive potential Eq. (2.13), the mathematically lowest order term is $a_{1m'}a_{lm}r^{l-1}$, arising from cross-terms with the $a_{1m'}A_{1m'}$ dipoles. The preceding arguments for vanishing effects arising from these dipoles also apply to these cross-terms.

The next higher order modification to the quadrupole ponderomotive potential arises from coupling to the quadrupole term $a_{20}A_{20}$ and has a $a_{20}a_{lm}r^l$ dependence. Since A_{20} is the trapping quadrupole, its strength a_{20} will be large compared to the strength of other multipoles.

A $(2l)$-pole departure from the quadrupole electric trap potential will thus cause a r^l perturbation to the pseudopotential. This perturbation in general couples the secular motion along principal axes of the quadrupole trap.

Octupole Perturbation

As the dipole A_{1m} and the hexapole A_{3m} are not present in a trap with symmetries about the radial plane ($z \to -z$) and inversion ($\vec{r} \to -\vec{r}$), the octupole is the leading perturbation inherent to the trap design to be presented in Section 2.2. The axially symmetric octupole term $a_{40}A_{40}$ causes a deviation from the ideal pseudopotential of

$$
\begin{aligned}
\Delta U_{\text{eff}} = \ & \frac{a_z}{64}\frac{a_{40}}{a_{20}}\frac{m\Omega^2}{z_0^2}\left(3x^4 + 3y^4 + 6x^2y^2 - 12x^2z^2 - 12y^2z^2 + 8z^4\right) \\
& + \frac{q_z^2}{16}\frac{a_{40}}{a_{20}}\frac{m\Omega^2}{z_0^2}\left(-3\left(1-\epsilon\right)x^4 - 3\left(1+\epsilon\right)y^4 + 6x^2y^2 \right. \\
& \qquad\qquad \left. - 12\left(1+\epsilon\right)x^2z^2 - 12\left(1-\epsilon\right)y^2z^2 + 16z^4\right).
\end{aligned}
\tag{2.19}
$$

For a quadrupole trap, this octupole term is a small perturbation. Thus, oscillation along the Cartesian axes is a good picture for secular motion, with a slight coupling between these oscillations given by the cross terms x^2y^2, x^2z^2 and y^2z^2 in Eq. (2.19), where the surprising sign of ϵ in the final two such terms is correct.

The octupole term $a_{40}A_{40}$ also adds a nonlinearity to the secular oscillations along each axis, such that the equations of motion, to first order in the radial symmetry breaking ϵ and neglecting the coupling between them, become

$$0 = \ddot{\chi} + \omega_\chi^2 \chi - \frac{3}{8} \frac{a_{40}}{a_{20}} \frac{\Omega^2}{z_0^2} \left(a_\chi + 8q_\chi^2\right) (1+\epsilon)\, \chi^3, \qquad \chi \in \{x, y\}\,, \tag{2.20a}$$

$$0 = \ddot{z} + \omega_z^2 z + \frac{1}{2} \frac{a_{40}}{a_{20}} \frac{\Omega^2}{z_0^2} \left(a_z + 8q_z^2\right) z^3. \tag{2.20b}$$

These differ from the equation of motion of the harmonic oscillator only by giving the restoring spring constant $k = -m\ddot{\chi}/\chi$ an amplitude dependence $k = k_0 + k_2\chi^2$. This kind of nonlinearity is relevant for many practical oscillators, such as the pendulum. It is known as Duffing oscillator because of a comprehensive investigation by Duffing (1918). It will be treated in Section 2.4.1 to analyse experimental resonance spectra of secular motion.

2.2 Design

2.2.1 Introduction

Goals

For laser spectroscopy of a nHz-linewidth transition in $^{171}\text{Yb}^+$, a trap offering a large viewing angle and long storage time for a single ion is required. It can be hypothesised that departures from the desired trapping field, evident as anharmonicities in the trap's pseudopotential, contribute to the heating of the ion and limit its storage time. Thus a trap with reduced anharmonicity was aimed for.

Further, an intentional departure from rotational symmetry was planned to facilitate laser cooling. In the rotationally symmetric case, there is no preferred direction in the radial plane: the two radial secular oscillations are degenerate and the ion can undergo a radial oscillation perpendicular to any given cooling beam direction. As laser cooling only works for motion along the beam axis, the rotationally symmetric case would necessitate a second cooling beam.

Prior Art

Good optical access can be achieved by the endcap design of Schrama et al. (1993). The radial electrode of a traditional Paul trap is split into an upper and lower half, which are moved axially outwards, becoming two hollow cylinders, one around each axial electrode. This structure has a large unobstructed field of view at the radial plane. Being a compromise between optical and electrical requirements, this trap design produces a less perfect quadrupole trapping field: The quadrupole coefficient a_{20} is reduced by a factor of 1.7 compared to the electrically ideal design. For a practical and easily machined realization of the classical Paul trap by Beaty (1986b), this reduction

factor is only 1.1. Further, higher multipoles are present to a larger degree in Schrama's trap than in Beaty's.

Higher multipole content creates a slightly anharmonic trap and might increase the heating rate. It is known and exploited in the mass spectrometry community that trap anharmonicities can influence the sensitivity of trapped ion clouds to ejection by a sweeping radio-frequency excitation of secular motion (Franzen et al., 1995). This effect is caused by an amplitude-dependent resonance frequency shift that causes the resonance to either shift with the sweep, staying resonant and destabilising the ion cloud, or to shift against it, avoiding the resonance and stabilising the cloud. This particular effect of trap anharmonicity is not relevant for the trapping stability in the absence of a sweeping excitation.

2.2.2 Method for Calculation of the Trap Potential

I have modified Schrama's endcap design to further minimise higher multipole content in the trap's electric potential. I calculated the potential by solving Poisson's equation $\nabla^2 \Phi = -\frac{\rho}{\epsilon_0}$ with the boundary condition of fixed potentials on the electrodes, using the commercial finite element software ANSYS. The simulation volume, shown in Figure 2.2, was restricted to one-eighth of the trap by exploiting the three plane symmetries (about the planes spanned by the three desired principal axes of secular motion).

The calculated potential is available on a number of nodes, approximately 300 within a radius of $z_0/10$. Extracting multipole coefficients a_{lm} by fitting to multipole potentials
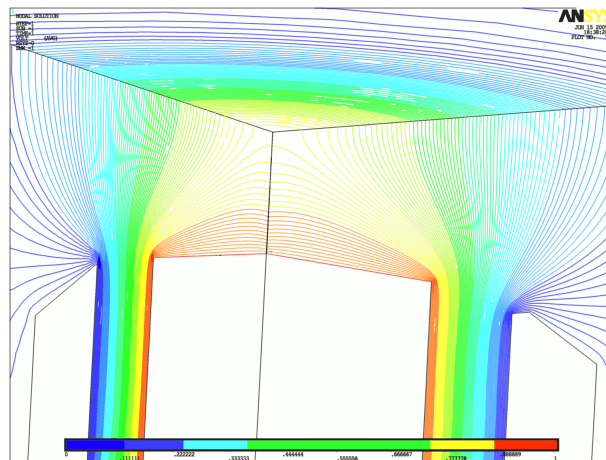
Figure 2.2: Equipotential lines for the trap design. Shown is the surface of the one-eighth space simulation volume, a cube with one corner at the trap's centre in the upper centre of image. The facet seen on top lies in the radial plane. The edge extending towards the bottom is the trap axis, whilst the stronger radial trap axis is shown extending to the top left. The remaining edge, extending to the right, is the weaker radial trap axis because of the cut in the outer electrode. The electrodes' cross sections appear in solid white.

introduces an error as the fit tries to approximate high-order multipole moments not included in the fit model by lower multipoles. An alternative approach is based on the fact that the multipoles $A_{l,m}$ form an orthogonal basis system. The multipole coefficients a_{lm} of Eq. (2.10) can thus be directly integrated from the potential $U(\vec{r}, V_t)$ by

$$a_{l,m} = \frac{\int\limits_{r<R} \mathrm{d}^3 r\ A_{l,m}(\vec{r})\ U(\vec{r}, V_t)}{V_t \int\limits_{r<R} \mathrm{d}^3 r\ A_{l,m}^2}. \tag{2.21}$$

This result is valid for any radius R, provided the spherical integration volume is charge-free. To apply this method, the volume v_i of each finite element i was extracted along with the potential $U_{i,n}(V_t)$ on each of its N_i nodes located at $\vec{r}_{i,n}$ and Eq. (2.21) was approximated by the discrete sum

$$a_{l,m} = \frac{\sum\limits_{|\vec{r}_{i,n}| \leq R} \frac{v_i}{N_i} A_{l,m}(\vec{r}_{i,n})\ U_{i,n}(V_t)}{4V_t \int\limits_{|\vec{r}| \leq R} \mathrm{d}^3 r\ A_{l,m}^2}. \tag{2.22}$$

2.2.3 Geometry and Calculation Results

Design Compromises

As a design compromise, I have allowed the quadrupole term to drop to a value 2.3 times lower than in the ideal case of hyperbolic electrodes. To break the rotational symmetry of the trapping field, I have incorporated a notch into the outer electrodes. The resulting geometry is shown in Figure 2.3. The notch produces a quadrupole term $a_{22}A_{22} = \frac{1}{2}a_{22}\sqrt{3}(x^2 - y^2)$ leading to the desired potential Eq. (2.15), but it also introduces small octupole terms a_{42} and a_{44}.

2.2.4 Numerical Results

I have calculated potentials in endcap traps for three parameter sets, namely for the design, for actual dimensions of a trap built to this design and for the design by Schrama et al. (1993). They have presented such results by plotting the fractional anharmonicity of the electric potential, which is its relative deviation from the desired quadrupole potential. Figure 2.5 shows such a plot for my calculation results. This completely characterises a radially symmetric design, as each radially symmetric multipole A_{l0} has a unique radial scaling r^l. An entire radially symmetric trap potential can thus in principle be deduced from the fractional anharmonicity curve along the axial direction.

The fractional anharmonicity along a coordinate axis does not capture all aspects of a trap with radial symmetry breaking. Deviations from the desired potentials may be considerable in directions other than the coordinate axes. For my design, the calculation
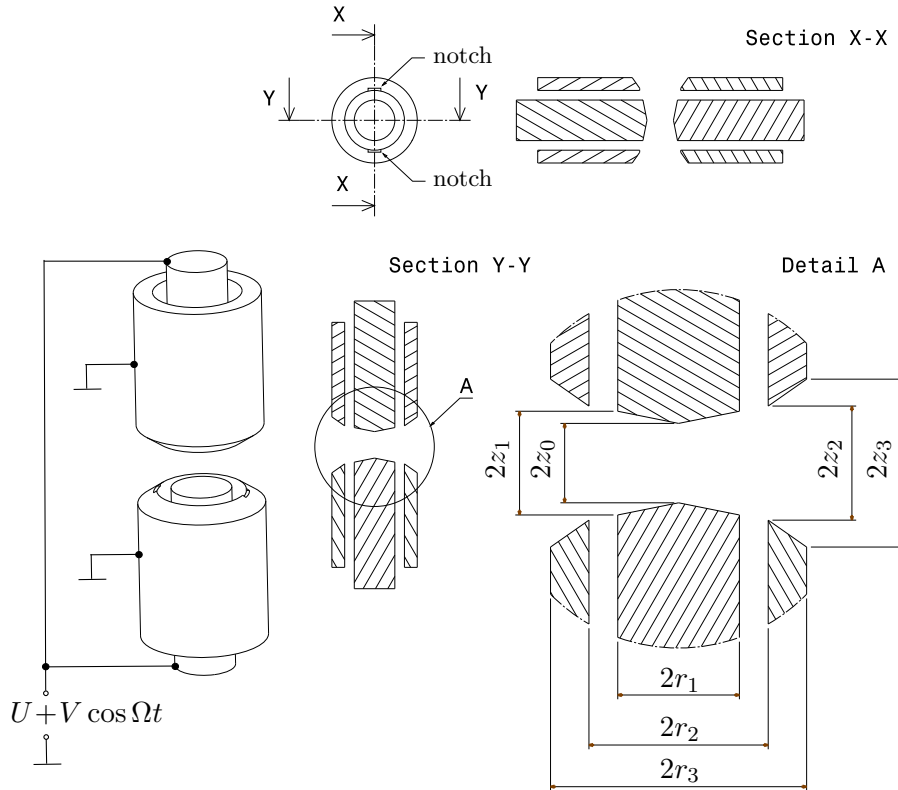
Figure 2.3: Trap schematics. The sectional drawings are oriented along the stronger (Y-Y) and weaker (X-X) radial axes. The central electrode separation $2z_0$ is 620 μm. Other named dimensions are listed in Table 2.1. The unnamed dimensions of the radial-symmetry breaking notches in the outer electrodes are a width of 300 μm and a depth of 35 μm.

shows this to be the case for the diagonal direction between the strong radial and the axial one. The calculated values of all multipole terms and the shape of the leading deviation produced by the design are shown in Table 2.2. This design was obtained by minimising these calculated values.

Table 2.3 gives results for other published Paul trap geometries, where I give both values calculated myself using the same method as for my own designs and literature values. Since the literature values have been obtained by a more specialised method better suited for these designs and exploiting their rotational symmetry, I take the difference between my values and those from literature as an error estimate for my own calculations. This error is probably a systematic effect, as the calculated multipole coefficients for my trap design were stable enough at small parameter changes to allow optimisation to numerically much lower calculated higher multipole coefficients than are significant by this error estimate.

I have also recalculated the multipole coefficients for the dimensions of the actual
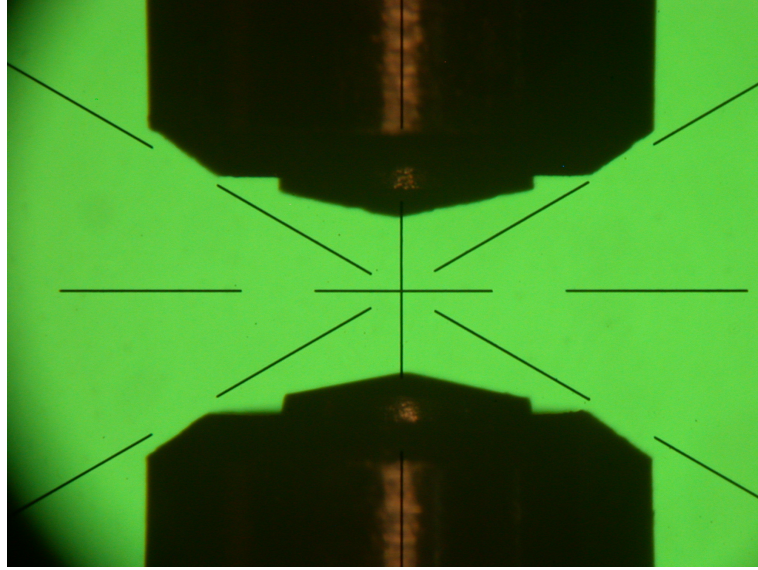
Figure 2.4: Microscope image of the trap electrode structure.

	Design	Workshop Design	Actual	Assumed for Recalculation
$2z_0$	620	620	610	610
$2z_1$	819	819		809
$2z_2$	900	900	925	925
$2z_3$	1320	1320		1345
$2r_1$	950	990		990
$2r_2$	1400	1400	1387–1405	1400
$2r_3$	2000	2000		2000

Table 2.1: Trap dimensions in µm. The first column corresponds to the original design for which the calculated potential is presented in Table 2.2. Because of a change in mounting the inner trap electrode, this was altered into the workshop design of the next column for fabrication. The next column lists measured distances. The axial distances (upper part of table) are based on microscope images such as shown in Figure 2.4. Of the radial distances (lower part of table), the inner diameter of the outer electrode was measured in a piece of the tubing from which the trap was built. As it is not round, a range of diameters was found. The final column shows the dimensions used for calculating the potential expected for the actual trap, see Table 2.4.
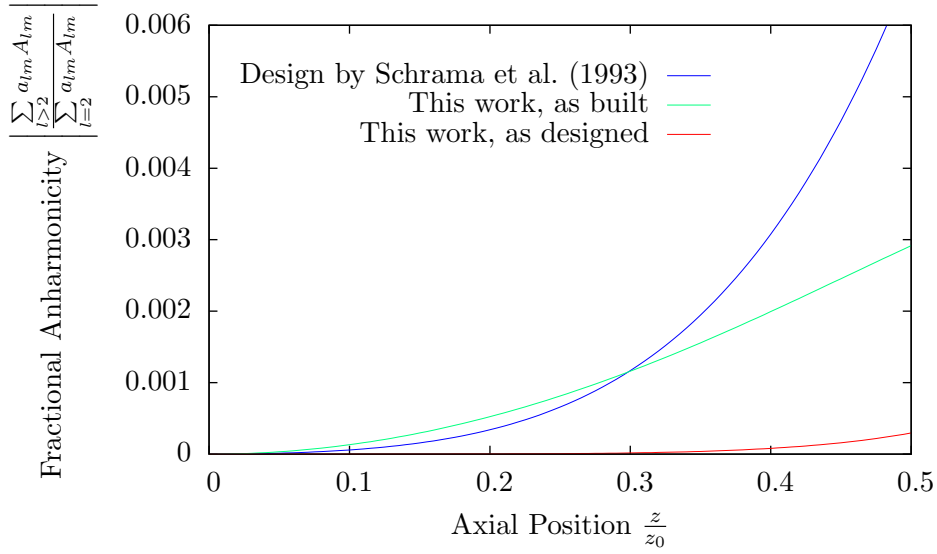
Figure 2.5: Calculated fractional anharmonicity of the electric potential. The potentials produced by the design of Schrama et al. (1993), the design presented in this thesis and that calculated for actual dimensions are compared in this plot.
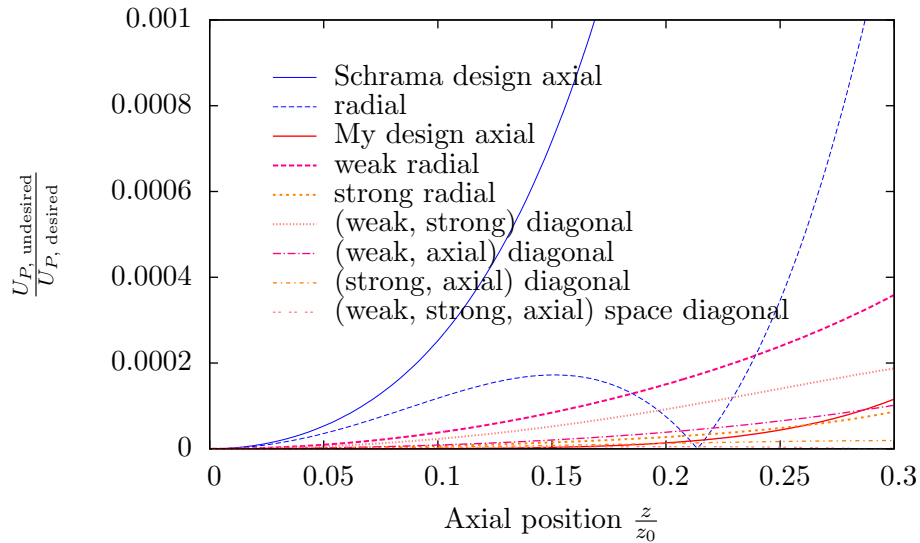
Figure 2.6: Calculated fractional anharmonicity of the ponderomotive potential $U_{P,\text{undesired}}/U_{P,\text{desired}}$. My design and that by Schrama et al. (1993) are compared for different directions away from the trap's centre. The surprising return to zero for the radial direction of the Schrama design occurs where octupole ($l = 4$) and duodecapole ($l = 6$) potentials cancel.

19

	$m = 0$	$m = 2$	$m = 4$	$m = 6$	$m = 8$
$l = 0$	0.767416				
$l = 2$	0.217632	0.000619			
$l = 4$	0.000000	-0.000075	0.000082		
$l = 6$	0.00016	-0.00003	0.00000	0.00000	
$l = 8$	0.0030	0.0000	0.0000	0.0000	0.0000
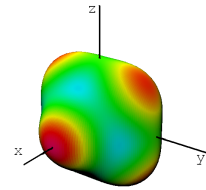
Table 2.2: Calculated multipole coefficients a_{lm} for the trap design with symmetry breaking. The deformed sphere (radius $r = 5 - Y_{42} + \sqrt{5/9}\,Y_{44}$) illustrates the directional effect of the octupole $-A_{42} + A_{44}$, which is the leading undesired multipole. The greatest deviations (red) occur along the weaker radial trap axis (x), and along the diagonal between the stronger radial (y) and the axial axis (z). Despite the almost equally strong deviation in potential along these two directions the effect on the pseudopotential is very different as one creates a field deviation parallel to the desired field, whilst the other creates one perpendicular to it. Some deviation of opposite sign in potential (cyan) also occurs along the diagonals between the radial trap axes, and on the diagonal between the weaker radial and the axial axes. All values are given to the significance to which they could be extracted from the finite element calculation; their true accuracy may be three orders of magnitude lower (see Table 2.3).

	Schrama		Beaty #1		Beaty #4	
	(calc.)	(literature)	(calc.)	(literature)	(calc.)	(literature)
a_{00}	0.720906		0.545613	0.545486	0.526559	0.524285
a_{20}	0.305489	0.29	0.425702	0.425798	0.453348	0.454473
a_{40}	-0.00152		-0.00099	≈ 0	-0.001600	≈ 0
a_{60}	-0.0270		0.00006	≈ 0	0.00037	≈ 0
a_{80}	-0.002		0.0059	0.1110	0.0006 (2)	0.0033

Table 2.3: Multipole coefficients a_{l0} for radially symmetric trap designs: The design by Schrama et al. (1993) is also an endcap trap, whilst those by Beaty (1986b) have a traditional ring geometry. The calculated coefficients were obtained with the same method as those given in Table 2.2. The discrepancy can be seen as an accuracy estimate of my calculation method. Beaty's literature values were obtained using a boundary element calculation, which for these rotationally symmetric geometries reduces to a 1-dimensional grid of calculation nodes (Beaty, 1986a), whilst the finite element method used here requires nodes on a 3-dimensional grid.

	$m = 0$	$m = 2$	$m = 4$	$m = 6$	$m = 8$
$l = 0$	0.79187				
$l = 2$	0.19773	0.00055			
$l = 4$	-0.0027	-0.0001	0.0001		
$l = 6$	0.001	0.000	0.000	0.000	
$l = 8$	0.00	0.00	0.00	0.00	0.00
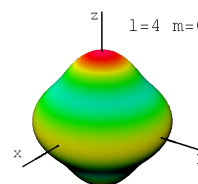
Table 2.4: Multipole coefficients a_{lm} calculated for measured dimensions, see Table 2.1. One more digit is given than presumed accurate from the comparison of Table 2.3. The deformed sphere ($r = 5 + Y_{40}$) illustrates the shape of the leading undesired multipole: The greatest effect is visible in the axial direction, where it increases (red) the potential, making the trap stronger axially. A smaller increase (orange) also occurs in the radial direction, weakening the trap radially as the trapping quadrupole is negative radially. A decrease (cyan) in potential occurs diagonally between any radial direction and the trap axis.

realization of the trap. The results are shown in Table 2.4. Here the deviation from the quadrupole potential is almost entirely due to multipole terms with radial symmetry.

It is not possible to cleanly generalise the fractional anharmonicity of the potential to arbitrary spatial directions because there are points in the trapping region where the desired quadrupole potential vanishes ($x^2 + y^2 = z^2$ for a radially symmetric trap). Even if a trap design produces only an infinitesimally small potential at such points, it would have infinite fractional anharmonicity. One could instead compare to the maximum desired quadrupole potential achieved at that radius, which occurs in the axial direction. However, such a definition underestimates the influence of some deviations, e.g., in a radial direction the same absolute deviation in electric potential compares to a lower pseudopotential than if it were on the axis.

To compare the anharmonicity along different directions in the trap design, Figure 2.6 shows the fractional anharmonicity of the ponderomotive force calculated for the trap design. A similar approach was chosen by Beaty (1986b), who plotted the square root of this measure, the "fractional error of the electric field." In my trap design, the greatest effect occurs along the weak radial trap direction, along which a notch is cut away from the outer electrode for radial symmetry breaking, whilst the anharmonicity along the strong radial trap direction is much lower.

2.2.5 Size of the Trap

The results presented in the previous section are true for any overall sizing scale of the trap. The chosen size, as listed in Table 2.1, satisfies practical constraints related to the trap's intended application in an optical frequency standard.

Lamb-Dicke Regime

Laser cooling on a 20 MHz FWHM transition such as the $^2\text{S}_{1/2}$–$^2\text{P}_{1/2}$ transition in $^{171}\text{Yb}^+$ limits the final temperature to about 1 mK (Blythe, 2005; Schneider, 2005). The trap must confine an ion of this temperature sufficiently strongly to reach the Lamb-Dicke regime $\langle x^2 \rangle^{1/2} \ll \lambda$. The mean displacement in a harmonic oscillator is related to the mean thermal energy by

$$\frac{1}{2}m\omega^2 \langle x^2 \rangle = \frac{1}{2}k_B T. \tag{2.23}$$

Thus the secular frequencies must be large compared to 80 kHz. The value of 700 kHz of an existing trap in our laboratory (Schneider, 2005) was set as a design goal.

Ion Heating

A low heating rate is advantageous because heating limits the period of time during which the ion will remain in the Lamb-Dicke regime without laser cooling. Deslauriers et al. (2006) found experimentally that heating rates in a quadrupole trap scale as the electrode distance to a power of -3.5 ± 0.1. To take advantage of this scaling, the trap should be built as large as possible. Doubling its size with no other change of experimental parameters requires quadrupling the drive voltage to maintain the same secular frequencies. Such scaling will eventually lead to a discharge as electron emission from the electrodes occurs. Secondary charge emission makes this a runaway process. Its onset is hard to predict, as it depends on the electric field at the electrodes' surface, a function of the microscopic surface roughness of the electrodes. A normal operating voltage of at most 600 V_{pp} was sought.

Resonances

A limit on the q_z parameter is imposed by the resonances between harmonics of the secular frequencies with the trap drive frequency. These occur at certain combinations of (a_z, q_z) parameters. Franzen et al. (1995) point out that choosing $q_z < 0.2$ is sufficient to avoid all resonances created by perturbations to the trapping potentials up to and including the 20-pole which transfer energy between the trapping field and the secular motion. As the number of 20 is a somewhat arbitrary choice, I have compromised about the q_z parameter, choosing it to be about 0.23.

Design Values and Implications

The requirement to minimise the q_z parameter with secular frequency and drive amplitude fixed determines the driving frequency. The geometry of the trap (shape-influenced a_{20} and size z_0) determines the value of the q_z parameter Eq. (2.7). A later abandoned plan of separating inner and outer electrodes by ceramic spacers limited the choice to diameters appropriate for premachined ceramic tubes, resulting in an inner electrode diameter of $2r_1 = 0.95$ mm and outer electrode diameters of 1.4 mm and 2.0 mm. This allowed a design with a predicted 700 kHz radial secular frequency at parameters $q_z = 0.23$,
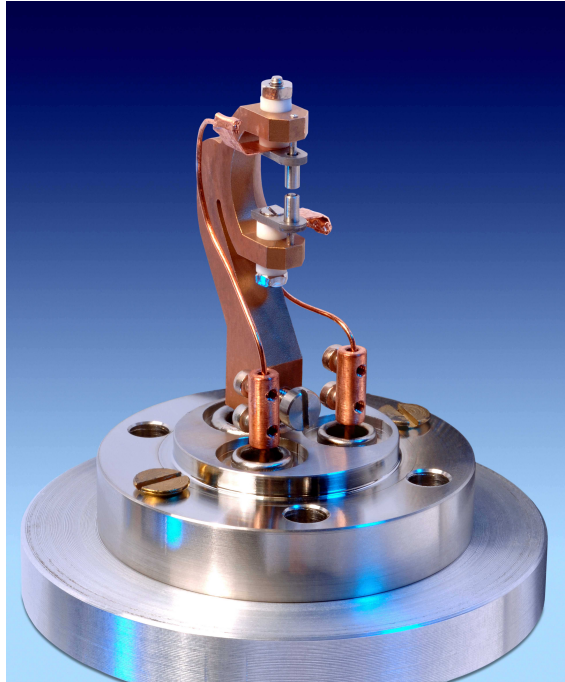
Figure 2.7: Photograph of the trap assembly, including a CF35 vacuum flange.

$a = 0$ for a driving voltage of $500\,\mathrm{V_{pp}}$ at $16.5\,\mathrm{MHz}$. The radial frequency splitting is predicted to be $2\epsilon = 1.0\,\%$. A schematic of the trap is shown in Figure 2.3 on page 17 and a microscope image of the physical realization in Figure 2.4 on page 18.

2.2.6 Construction

The trap was built with free-standing electrodes without a ceramic spacer close to the trapping region. This choice reduces patch potentials and heating of the electrodes, to which the RF power dissipation in ceramic spacers would contribute. A photograph of the finished assembly is shown in Figure 2.7.

The free-standing electrodes required a departure from the designed inner electrode diameter, which was built at $0.99\,\mathrm{mm}$ instead of the design value of $0.95\,\mathrm{mm}$. For the alignment of upper versus lower electrodes, the electrode spacings have been measured. The dimensions for the trap design as calculated and as built are compared in Table 2.1 on page 18.

Copper beryllium was chosen as material for the support structure of the free-standing trap because of its high conductivity, and good mechanical properties. For the actual trap electrodes, molybdenum was used because of better workability and the rare coincidence that its oxide has essentially the same work function as does the metal. This may reduce patch potentials but will not eliminate them as surface contaminations other than oxidation can occur, as the structure is exposed to Ytterbium vapour when loading the trap and continuously to residual gas in the vacuum chamber.

2.3 Characterisation

This chapter explains the experimental characterisation of the trap. The following section describes the setup, giving details about trap driving, external electrodes for field compensation, ion cooling and detection. Section 2.3.2 on page 27 reports on secular motion frequency measurements used to calibrate the translation between trap parameters and voltages applied to the trap. The calculated quadrupole strength is verified, but the radial symmetry breaking is found to vary strongly with compensation voltages. This effect is further examined experimentally in Section 2.3.3 on page 31 and compared to calculation in Section 2.3.4 on page 36. Finally, Section 2.4.2 on page 42 investigates the shape of secular motion resonances and links these to anharmonicities, concluding the comparison between predicted and calculated properties of the trap.

2.3.1 Setup

Overview

The ion trap design from Section 2.2 was built with an electrode separation of 610 μm and used to trap ^{171}Yb$^+$. It was designed to operate with a q_z parameter of 0.23 and secular frequencies of about 700 kHz and 1.4 MHz. At trap parameters $q_z = 0.42$ and $a = 0$, a trapped single ^{171}Yb$^+$ ion repeatedly stayed in the trap without laser cooling for more than 12 hours.

The trap is driven electrically by a resonance transformer. A frequency generator supplies the drive signal via a RF power amplifier. Resonance occurs at 16.255 MHz. The desired amplitude is not set directly as function generator amplitude, but rather by tuning its frequency slightly away from the transformer's resonance to avoid glitches when the function generator switches attenuators. Thus the trap is usually operated with a function generator amplitude of 250 mV peak to peak at a frequency between 16.17 and 16.255 MHz. The transformed voltage applied to the trap is monitored by a capacitive tap in the transformer.

The trap is operated in an ultra high vacuum chamber pumped by an ion getter pump. The setup allows the usage of helium as buffer gas. The pressure was measured by an inverted-magnetron gauge. The ultimate pressure is about $2 \cdot 10^{-10}$ mbar. It quickly rises to above 10^{-8} mbar after turning off the pump, but additional helium must be introduced to achieve a buffer gas pressure of 10^{-6} mbar. Such a pressure is necessary to produce ion clouds with fluorescence count rates of 100 kHz.

Fluorescence of ^{171}Yb$^+$ on the ^{2}S$_{1/2}$–^{2}P$_{1/2}$ transition at 369 nm was excited by a frequency doubled external cavity diode laser delivering about 10 μW of output power. A term scheme is shown in Figure 2.8. This transition is also used for laser cooling of single ions. Because of the second harmonic generation, the beam is not Gaussian; the focus created inside the trap is measured to be 45 μm wide and 28 μm high. The light scattered by the ion is imaged with an objective of 18.8 mm effective focal length onto an intensified CCD camera, with a magnification of 82. Alternatively, by flipping a repositionable mirror, a photomultiplier tube could be used for photon counting.

F=0 —————— $^2\left[1/2\right]_{1/2}$
F=1 ——————

$^2P_{1/2}$

935.2 nm

$^2D_{3/2}$

F=2
F=1 ——————

F=1 ——————
F=0 —————— $^2S_{1/2}$

369.5 nm
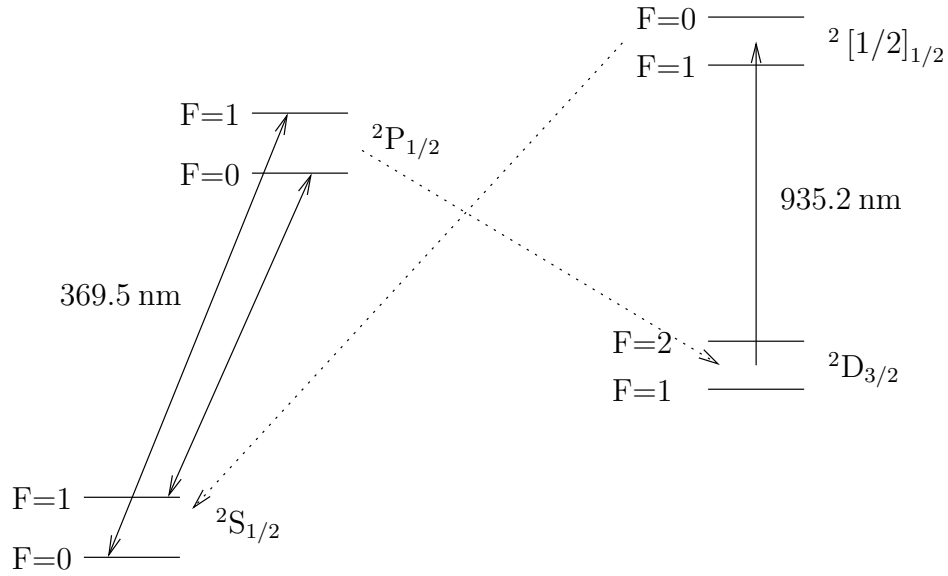
Figure 2.8: Laser cooling of ^{171}Yb$^+$. Both hyperfine components of the $^2S_{1/2}$–$^2P_{1/2}$ transition are driven by a single laser source with a suitable modulation sideband. The $^2D_{3/2}$ state is metastable. Both of its hyperfine sublevels are depopulated with a repumper laser.

To get efficient fluorescence, a small magnetic field is applied to avoid optical pumping to a dark superposition of the ground-state magnetic sublevels. The entire trap and most of the vacuum chamber is enclosed by a magnetic shielding to enable future usage of this setup in a single-ion frequency standard. Further, a repumper laser at 935 nm is needed to depopulate the $^2P_{3/2}$ state, to which the ion decays from the $^2P_{1/2}$ state with a branching ratio on the order of one percent.

Stray Field Compensation

The ion in the trap is offset from the true potential minimum of the trap's quadrupole potential by a static stray field. This results in excess micromotion, increased RF heating, impedes laser cooling and leads to Stark shifts because the ion samples the trapping field outside the field-free region at the trap's centre. The effect on laser cooling can be seen from the spectrum of Figure 2.9. Several methods for stray field compensation have been reported in the literature; for a comparison, see Berkeland et al. (1998).

The stray field can be cancelled by applying the opposite field via external electrodes. In the axial direction, the nominally grounded outer (shielding) electrodes can be set at opposite potentials to create such a field. I will refer to this voltage difference as z-voltage. In the radial direction, a field can be created by applying voltages to the Ytterbium oven and a thin wire also used as electron source. Each of these has a counter-electrode on the other side of the trap, in the shape of a wire with 1 mm diameter. The voltages used are shown in Table 2.5.
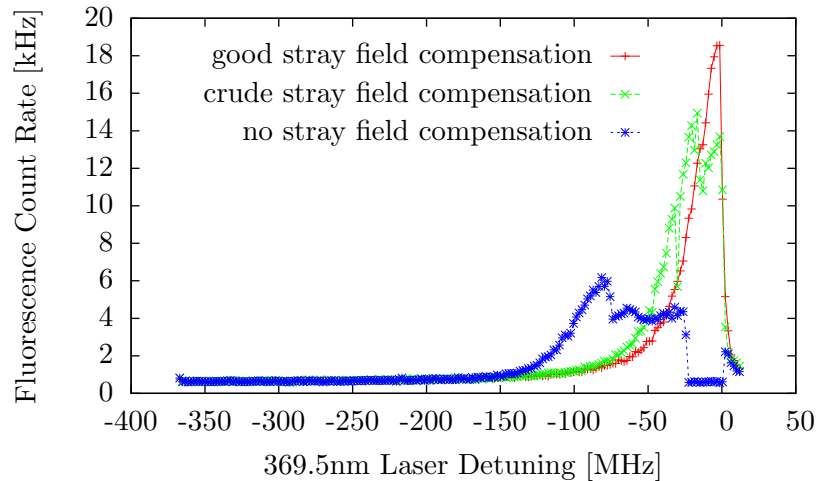
Figure 2.9: Excitation spectra of a single laser-cooled ion on the $S_{1/2}$–$P_{1/2}$ transition. Shown is the fluorescence versus the detuning of the excitation frequency, estimated from the piezo voltage used to detune a cavity that the cooling laser is locked to. For good stray field compensation, the observed spectrum resembles the half-Lorentzian lineshape expected for laser cooling. Increasing the voltage at the counter electrode to the electron gun from 0 to 100 V (crudely compensated curve) reveals motional sidebands at harmonics of the trap drive frequency of 16.25 MHz. These are poorly resolved because of the slightly larger transition linewidth. Without any stray field compensation, this effect leads to significant fluorescence even for a detuning of 100 MHz.

	A	B	C	D
z-voltage	1.7 V	4.3 V	4.3 V	4.3 V
Oven	−150 V	−105 V	−120 V	−69 V
e-Gun	28 V	25 V	25 V	19 V
Oven counter electrode	0 V	0 V	0 V	0 V
e-Gun counter electrode	0 V	0 V	0 V	0 V
Date	8/2008	12/2008		6/2009

Table 2.5: Compensation voltages used in experiments. z-voltage denotes a potential difference applied to the nominally grounded outer electrodes of the trap, initially limited to 1.7 V due to limitations in the driving electronics. The counter electrodes are wire ends located opposite from the named electrodes.

I have determined appropriate compensation voltages for the caps, the oven and the electron gun by observing the position of a single ion with an electron multiplying CCD camera for varying trap parameters. This changes the spring constant of the trap and thus allows the stray field to pull the ion away from the trap centre by a variable distance.
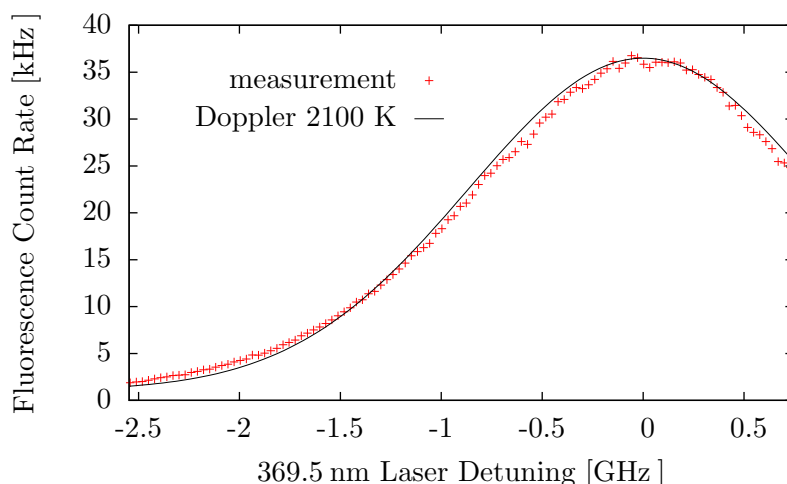
Figure 2.10: Excitation spectrum of the $S_{1/2}$–$P_{1/2}$ transition in an ion cloud cooled by Helium buffer gas. The fluorescence intensity is plotted versus the detuning of the excitation frequency, estimated from the piezo voltage used to detune a cavity that the cooling laser is locked to. By fitting to a Doppler profile, an estimate of 2100 K is obtained for the ion cloud's temperature.

By choosing compensation potentials where no such motion can be seen, the stray field is compensated.

The compensation voltages change over time. This might be due to Ytterbium coating of parts of the electrodes' surface, other impurities getting absorbed or reacting with it and changes in the work function of such patches. Set "A" was found empirically by first optimising the fluorescence from ion clouds in buffer gas and then the trapping of single ions; the z-voltage was intentionally left below the optimal value due to initial limitations in the trap electronics. Set "B" was found by the method outlined above and used to measure secular frequencies for the calibration of the trap parameters. Occasionally, set "C" was used by mistake (an oven voltage set to 48.1 instead of 41.8 in displayed units of 2.5 V). When a fluorescence spectrum as shown in Figure 2.9 revealed sidebands for the compensation set "C", indicating uncompensated stray fields, set "D" was found, again by the method described above.

2.3.2 Secular Motion Frequencies

In the first attempts to operate the trap, operating conditions close to those assumed in the design for single ion storage were used for trapping ion clouds in a buffer gas at a pressure of 10^{-6} mbar. Figure 2.10 shows the fluorescence spectrum of an ion cloud, from which I estimate an ion temperature of 2100 K. Using a method detailed in the following, at trap parameters $q \approx 0.26$ and $a = 0$, the observed radial secular frequencies with all compensation electrodes grounded were 748 and 754 kHz. The difference of 0.8 % comes close to the design value of 0.98 % (0.96 % calculated for the actual dimensions of the

trap).

However, the secular motion frequencies were observed to vary strongly with the potential of compensation electrodes. This section presents further measurements of secular frequencies, all performed at the proper compensation voltages (set "B") for field compensation. As a result, calibration factors to link experimentally chosen operating conditions to trap parameters were found along with a radial frequency splitting of 2.0 % under these conditions.

Trap Parameter Calibration

The DC voltage U applied to the central trap electrodes can be measured directly, but the AC voltage V is only observed indirectly as a proportional monitor voltage v. To determine the calibration factor V/v, I have measured the secular motion frequencies of ion clouds. Secular motion was excited by applying an AC voltage to one of the outer trap electrodes and observed as a reduction in the on-resonance 369 nm fluorescence rate as secular motion increases the ion temperature and decreases the spatial overlap with the laser beam. At excitation amplitudes of a few millivolts, the axial secular motion can be excited at its fundamental frequency and radial secular motion at its second harmonic (parametric oscillation). The radial motion can also be excited at its fundamental frequency by using a larger AC voltage or by applying it to a compensation electrode. These frequencies were fitted to the theoretical values

$$\omega = \frac{1}{2}\beta(q, a)\Omega. \tag{2.24}$$

Three fit parameters were used: The quadrupole strength a_{20} was found to be 0.201 (1) assuming an electrode separation of $2z_0 = 610\,\mu\text{m}$. The radial asymmetry factor was fitted to be ϵ is 0.0102 (26) and the transformation ratio V/v is 1792 (28). As I have measured peak-to-peak voltages v_{pp} the practically relevant transformation ratio is $V/v_{\text{pp}} = 896 \pm 14$. Measurement data and fit curves are shown in Figure 2.11.

The trap parameters and secular frequencies can now be expressed in observed quantities:

$$|q_z| = 4a_{20}\frac{e}{mz_0^2\Omega^2}V = 110\frac{v_{pp}}{[\text{V}]}\left(\frac{\Omega/2\pi}{[\text{MHz}]}\right)^{-2} \approx 0.42\frac{v_{pp}}{[\text{V}]}, \tag{2.25a}$$

$$a_z = 8a_{20}\frac{e}{mz_0^2\Omega^2}U = 0.247\frac{U}{[\text{V}]}\left(\frac{\Omega/2\pi}{[\text{MHz}]}\right)^{-2} \approx 0.00094\frac{U}{[\text{V}]}, \tag{2.25b}$$

$$q_{x,y} = \frac{(1\mp\epsilon)}{2}|q_z|, \tag{2.25c}$$

$$a_{x,y} = -\frac{(1\mp\epsilon)}{2}a_z, \tag{2.25d}$$

$$\omega_{z,y,z} \approx \frac{1}{2}\Omega\sqrt{\frac{1}{2}q_{x,y,z}^2 + a_{x,y,z}}. \tag{2.25e}$$

The maximum voltage applied to the trap creates a 1.0 V peak-to-peak monitor voltage, corresponding to $q_{z,\text{max}} = 0.42$.
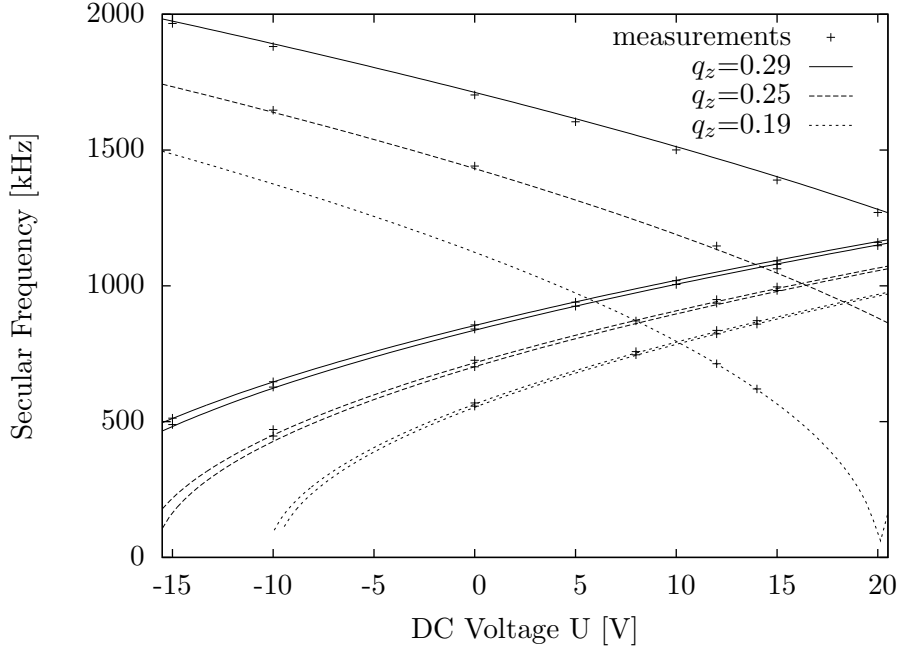
Figure 2.11: Secular frequency measurements at three different q parameters. The lines show a single numerical fit. The q parameters given were calculated from a fit result, the transformation ratio of trapping voltage V to measured monitor voltage v.

Influence of Field Compensation

The trap asymmetry ϵ seen in the radial secular frequencies at compensation "B" (reported in Section 2.3.2) appears to be twice as large as designed. In contrast, an initial measurement at compensation "A" is in reasonable agreement.

But the secular frequencies seen are not caused exclusively by the trapping field: any electric field inside the trap exerts a force on trapped ions. It was found experimentally that voltages applied to compensation electrodes have a large influence on the secular frequencies, see Figure 2.12. This occurs because the potential created by a compensation electrode will, to some degree, create a quadrupole field inside the trap. Trapped ions then see an additional acceleration due to this quadrupole field, which along an axis $\vec{e}_x$ of the secular motion is

$$\Delta(\ddot{x}) = \frac{e}{m} \frac{\partial^2 \Phi(U_{\text{oven}})}{\partial x^2} x. \tag{2.26}$$

The resonance frequency ω_0 is changed to a new value $\omega(U_{\text{oven}})$ with

$$\omega^2(U_{\text{oven}}) = \omega_0^2 - \frac{e}{m} \frac{\partial^2 \Phi(U_{\text{oven}})}{\partial x^2}. \tag{2.27}$$

The $\vec{e}_y$ axis behaves accordingly. The fit shown in Figure 2.12 corresponds to a derivative $v_2 = \partial E_x / \partial x$ of the field component $E_x = -\partial \Phi / \partial x$ along one axis of the radial

29
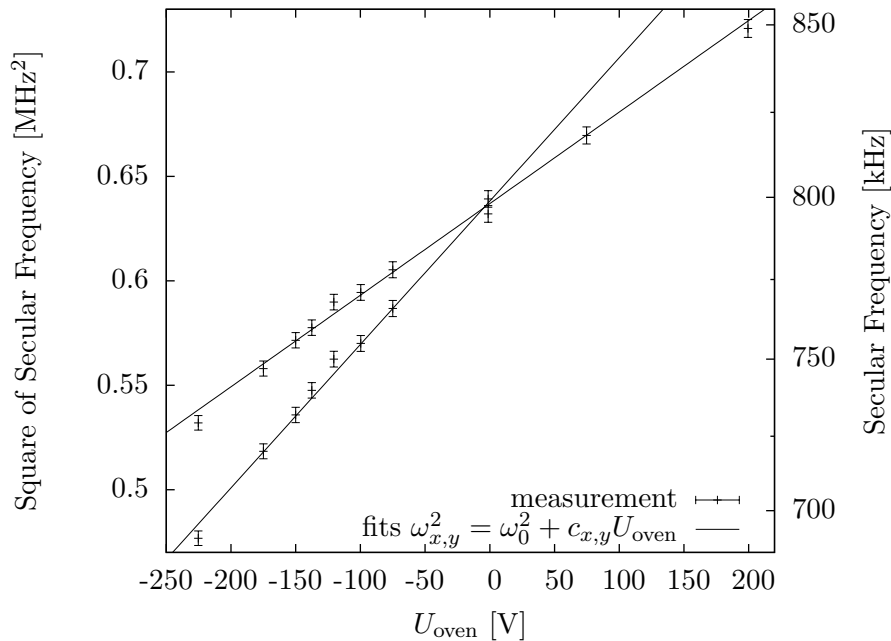
Figure 2.12: Radial secular frequencies as a function of oven potential for trap parameters $q_z = 0.27$, $a_z = 0$. The quadrupole components of the oven potential act as additional parabolic potential terms, adding to the square of the undisturbed secular frequencies, shown on a the linear scale on the left.

secular motion, per oven potential, of $-0.0480(20)$ /mm^2 and along the other axis of $-0.0306(6)$ /mm^2.

Summary

The trap parameters have been expressed in directly observable quantities such as a monitor voltage, which is the down-transformed AC trap drive voltage. The transformation ratio and the quadrupole strength of the trap have been measured. The quadrupole strength agrees with the design: It is 8 % below the designed value, but agrees to within 2 % of that calculated for the actual dimensions of the trap assembly. There is less agreement between design and physical realization in the radial frequency asymmetry factor 2ϵ, which was measured as 2.0 %, twice the design value. I found that this splitting is influenced by choosing compensation voltages applied to electrodes outside the actual trapping electrodes. The observed splitting of radial secular frequencies can easily be doubled or halved by voltages as needed for field compensation. This is a much larger effect than that seen in a more traditional Paul trap in our laboratory (Schneider, 2005). This might explain why, using zero compensation voltages, the frequency splitting appeared to be just below the design target of 1 % in an earlier assessment.

2.3.3 Stray and Compensation Potentials

To investigate the origin of the surprisingly large secular frequency shift with compensation voltage, I have measured the ion displacement caused by compensation potentials to characterise the latter. The compensation electrodes are all located in the plane containing both of the radial principal axes of the trap. This geometry is illustrated in Figure 2.13.
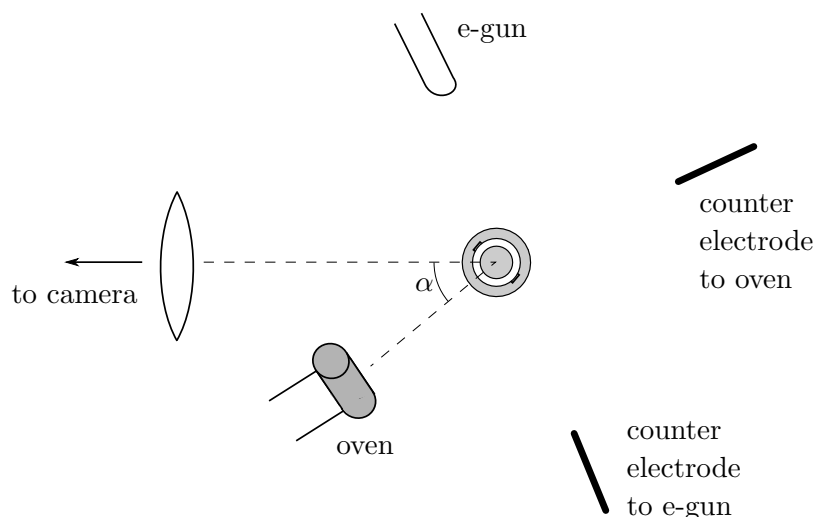
Figure 2.13: Arrangement of compensation electrodes. The axial trap direction points out of the paper. All four compensation electrodes are at the same distance to the trap. The oven is built as a long cylinder, the electron source (e-gun for brevity) is a thin wire and the counter electrodes are simple wire ends. The angle α between image axis and oven electrode exemplifies the corresponding angles for each of the four compensation electrodes. These angles are given in Table 2.6.

Electrode	Angle α	$\sin\alpha$	$\cos\alpha$
oven	27.80°	0.466	0.885
counter oven	207.80°	-0.466	-0.885
e-gun	−62.20°	-0.885	0.466
counter e-gun	109.84°	0.941	-0.339

Table 2.6: Projection factors for compensation electrodes. The design angle α as shown in Figure 2.13 is given for each electrode. In the camera's image plane, a motion towards an electrode has the projection factor $-\sin\alpha$. Out of the image plane, the projection factor for the focal shift is $+\cos\alpha$.
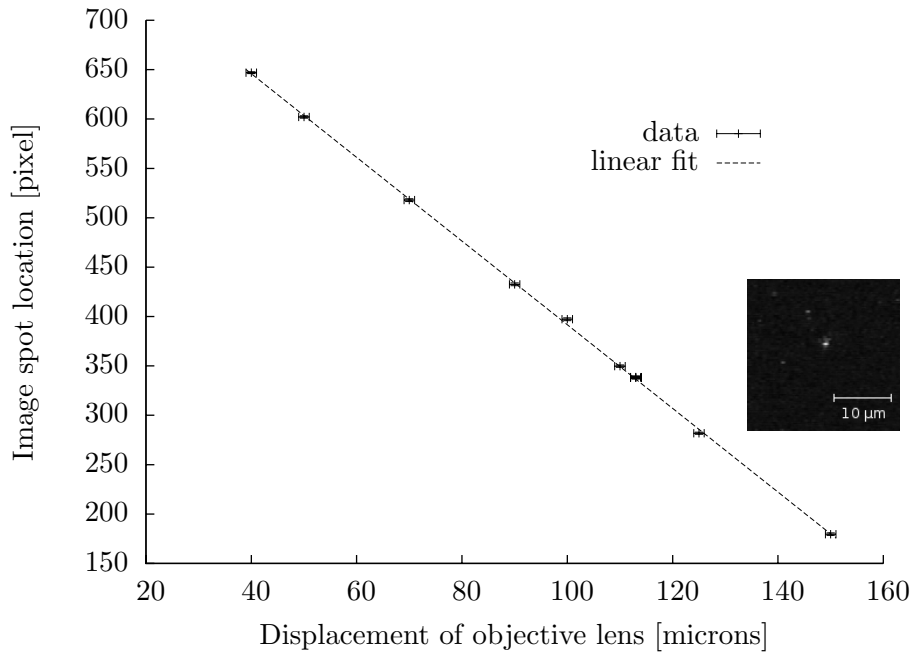
Figure 2.14: Camera spot position versus known lateral displacement of objective lens. The vertical error bars indicate the standard deviation amongst the 21 to 160 camera images evaluated per data point, the horizontal ones correspond to an assumed 1 μm combined positioning accuracy and reading error of the differential micrometer screws moving the objective lens. A sample camera image is shown as inset. Each image pixel corresponds to 236.0 ± 1.4 nm translation of the objective.

Position Detection

The ion's motion was observed in a plane containing the trap axis by camera and perpendicular to this plane by focusing the objective lens with a micrometer screw. The camera image position can be calibrated into an actual displacement by moving the objective lens laterally. The result is shown in Figure 2.14. After digitisation of the analog TV output signal of the camera, one pixel corresponds to a 236 nm translation of the objective lens. As the magnification factor is 82, each pixel covers a size $\frac{82}{82+1}$ times that much, 233 nm, in the trap.

The camera observation only shows a projection of the ion's motion. The motion out of its focal plane is determined from the micrometer screw position for best focussing. Plotting both, as in Figure 2.15, shows the direction of the ion's motion and hence the translation factor between the apparent motion observed in the camera projection to the actual distance travelled by the ion.

Figure 2.15 also demonstrates that the displacement caused by a potential applied to a compensation electrode has the same orientation for different trap depths. This is
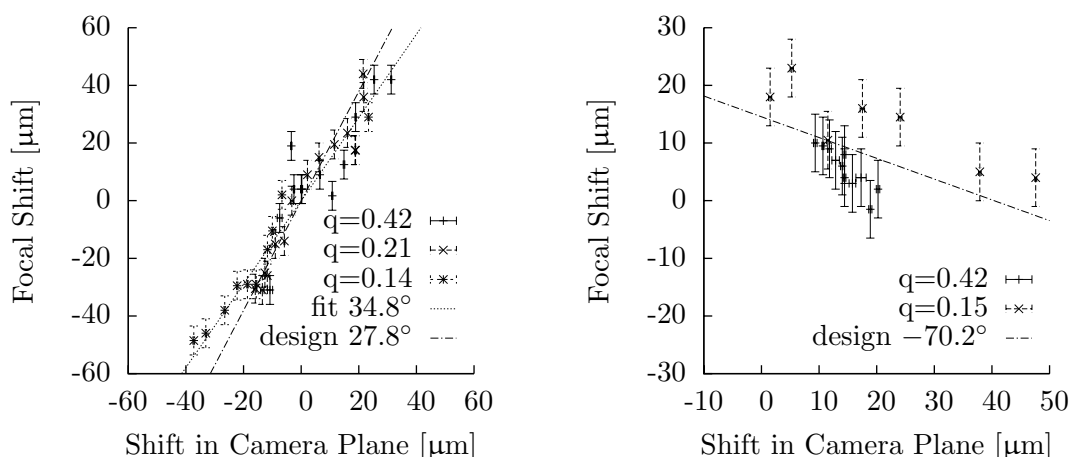
Figure 2.15: Ion motion due to a compensation potential applied to the oven (left) and to the counter electrode to the electron gun (right). In the former case, the actual travel is 1.75 times the apparent motion projected onto the camera plane. In the later case, actual and apparent travel are almost identical.

expected because only traps with $a = 0$, where the radial symmetry breaking is small, were used. Hence the deflection direction is determined only by the location of the compensation electrode, not by the restoring force anisotropy caused by the symmetry breaking.

Field Determination for the Oven used as Compensation Electrode

Along the direction in which the compensation electrode is pulling the ion, the forces acting on it are

$$F = m\omega^2 x + e\left(v_1\left(V_c - U_1\right) + v_2\left(V_c - U_2\right)x + \ldots\right). \tag{2.28}$$

Here $v_1 V_c$ is the field created by applying a voltage V_c to the compensation electrode, causing the total field to vanish when it equals the compensation voltage U_1. Spatial variations of the field are captured by higher order parameters (v_2, U_2), (v_3, U_3), etc. The frequency ω is a measure of the trap stiffness in the direction of ion motion. It will lie between the secular motion frequencies ω_x and ω_y. Using their averages for ω and setting all v_i and U_i for $i \geq 2$ zero (keeping only the field coefficient v_1 and the field compensation voltage U_1), the field can be extracted from ion position measurements. The result is a compensation field coefficient v_1 of -0.008 /mm, and a compensation voltage of -123 V, but the fit residuals are significant.

Extending the fit Eq. (2.28) to also cover the derivative of the field along the motional direction of the ion improves the fit. It is shown in Figure 2.16. The fit model then (up
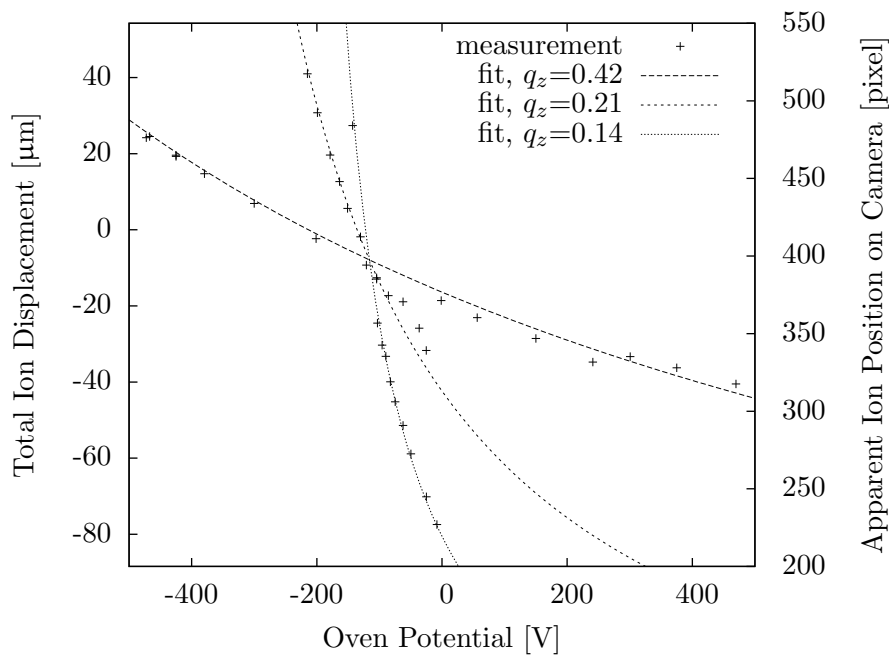
Figure 2.16: Ion motion due to a compensation potential applied to the oven. The single fit assuming a linearly varying stray and compensation field is shown for the three sets of trap parameters used.

to terms v_2, U_2) is

$$x = -\frac{v_1 (V - U_1)}{v_2 (V - U_2) + \frac{m}{e}\omega^2}. \tag{2.29}$$

This fit estimates the compensation field to be $-0.0073(3)$ V_c/mm, and its derivative to be $-0.048(6)$ V_c/mm^2. The stray field is compensated at a voltage of $U_1 = -116(2)$ V, its derivative at $U_2 = -6(17)$ V. The given uncertainties are standard deviations incorporating the correlation between the parameters (75 % between v_2 and U_2, 61 % between v_1 and U_2) by giving the full extent of the standard deviation ellipsoid. At the proper compensation voltage, the ion position is unaffected by the trap's steepness: Here the fit curves for different trap strengths intersect, as seen in Figure 2.16.

Fitting to a yet higher order in the electric potential does not significantly improve the fit and suffers from extremely strong correlation between all of v_2, v_3 and U_3. Constraining the ratio v_3/v_2 to 3 /mm, a value suggested by the calculations of Section 2.3.4, and U_3 to zero, avoids these correlations. In this case, I find that none of the previous parameters move beyond their estimated errors, validating the fit model.

Field Determination for the Counter Electrode to the Electron Gun

The same measurement as described for the oven has also been done for the counter electrode to the electron gun, see Figure 2.17. This electrode moves the ion in a different
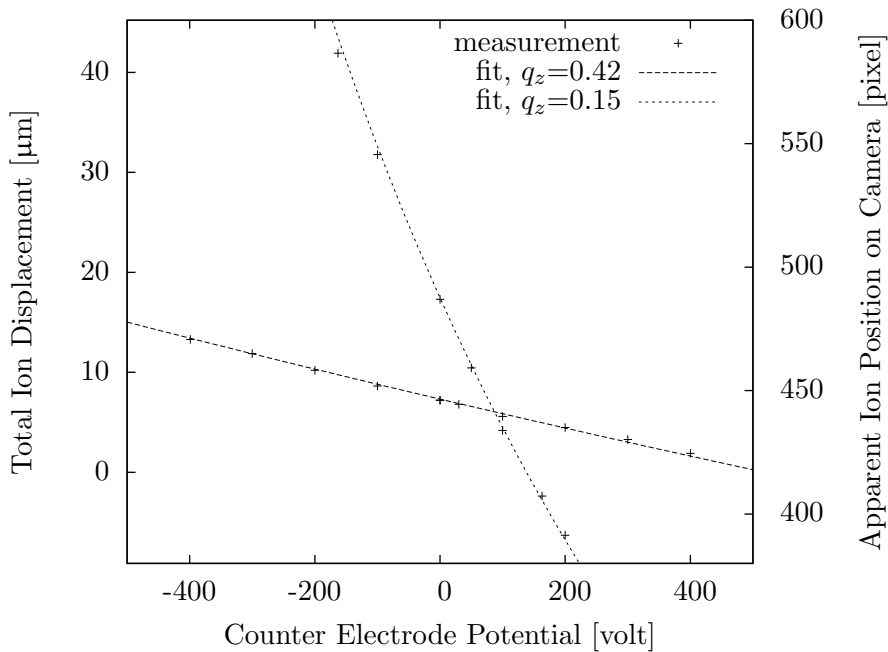
Figure 2.17: Ion motion due to a compensation potential applied to the counter electrode to the electron gun. The single fit assuming a linearly varying stray and compensation field is shown for the two sets of trap parameters used.

direction, thus different values for the stray field can be expected. Its different shape may further cause the compensation field to be different. It is difficult to extract the direction along which the ion moves from Figure 2.15, but the motion is compatible with one towards the intended position of this compensation electrode. As this direction only has a small component out of the focal plane, the total displacement of $|\cot \alpha| \approx 1.06$ times the apparent displacement has a far lower uncertainty than the angle α determining the exact direction of motion.

Assuming the design direction for the ion motion, fitting yields a field coefficient v_1 of $-0.00143(9)$ /mm and a potential U_1 of $84(4)$ V required to compensate the stray field. The field derivative coefficient v_2 is $-0.0084(20)$ /mm^2, compensating the derivative of the stray field at a voltage U_2 of $301(154)$ V.

The surprisingly large derivative of the stray field $-v_2 U_2 \approx 2.5(9)$ V/mm^2 is significant because the correlation between v_2 and U_2 is such that the product has a reduced error. It is probably caused by the other compensation electrodes. Using the lower field derivative found from secular motion dependence on page 29, even the nearly perpendicularly oriented oven contributes $3.6(4)$ V/mm^2. This assumption is well-founded, as the larger of the two values found there must be assumed to act along the direction towards the oven to be consistent with the value found from ion motion towards the oven. The uncertainty in matching the directions determines the error bar. Assuming further that

the electron gun produces, to within 50 %, as much quadrupole potential as the oven does per applied voltage, the expected combined field derivative along the counter electron gun electrode becomes 2.5(7) V/mm^2 for the employed compensation voltage set "C."

A possible effect of the oven potential may also be visible as additional focal shift between the shallow and steep trap setting in the right graph of Figure 2.15. This difference of about 10 µm is not necessarily significant as it barely exceeds the estimated error in determining the focal position. Explaining it also requires assuming that the oven potential applied was too high by about 15 V.

As ion loss occured during the measurement (caused by attempts to achieve ever larger ion displacements from the trap centre), the trap had to be reloaded many times, concurring with Ytterbium vapour coating due to the use of the oven. The shift in compensation voltage required to explain such a difference of 15 V seems possible, considering that the next determination of the oven compensation voltage (set "D") demonstrated a shift of over 50 V compared to the compensation voltage estimated here.

Comparison

Comparing the field produced by the oven and by the e-gun counter electrode, both field and field derivative of the oven are larger by a factor between five and six for the same applied voltage. Regarding the field, this factor is plausible because the e-gun counter electrode is a cylinder pointing to the trap, presenting a small area, whilst the oven is a perpendicularly oriented cylinder with an approximately five times larger area. Both have a diameter of 1 mm and a nearest distance of about 6.4 mm (design value, actual not measured) from the trapping region. The fact that the ratios between the field and the field derivative are similar for both electrode geometries suggests that the shape of the field at the trap might depend less on the external electrode geometry than on the the shielding effect of the trapping electrodes. This possibility will be examined in the following section, which also features a tabular summary of field and field derivative coefficients in Table 2.7 on page 38.

2.3.4 Compensation Potential Calculation

For a simplified geometry, a spherical compensation electrode with 1 mm diameter, the compensation field was calculated with the same finite element method used for the trap field calculations (Section 2.2.2). Here, all trap electrodes were grounded and a potential was applied at the surface of the spherical compensation electrode. For this geometry, the calculation volume for which a solution could be obtained without compromising mesh detail in the trapping region was only marginally sufficient to even include the compensation electrode at the proper distance. Hence, boundary conditions are important.

I have approximated an unbounded, infinite volume by using a layer of boundary infinite elements (Zienkiewicz et al., 1983) implemented in ANSYS as boundary element type "INFIN111." These work by remapping coordinates such that the simulation volume represented by the finite element actually extends to infinity. The boundary condition
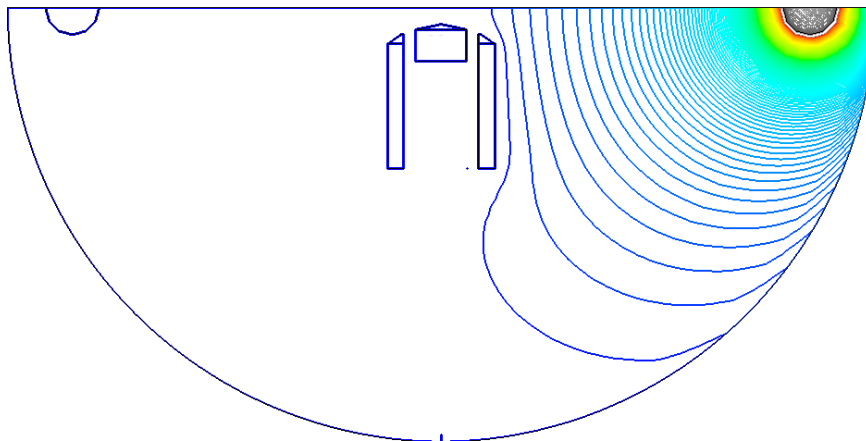
Figure 2.18: Calculated electric potential of a spherical compensation electrode. The trap structure is in the centre of the displayed cross-section containing the trap axis and, on the right, the centre of the compensation electrode. Because of the symmetry of the problem, only part of the volume has been included in the calculation; thus the upper half of the trap is omitted. Drawn are equipotential lines representing a linear scale from ground to compensation electrode potential.

assumed at infinity is a vanishing electric potential. As these boundary elements had to be placed very close to the compensation electrode to avoid exceeding a maximum number of elements for which the problem could be solved, some imperfections occur at the boundary near the electrode. These are evident in the calculated potential shown in Figure 2.18: in the immediate vicinity of the spherical compensation electrode, a spherically symmetric potential is expected, but some deformation of equipotential lines occurs at the boundary. The effect is small and along the interesting direction towards the trap's centre, the calculated potential initially follows the expected r^{-1} scaling. Therefore, I expect the calculated potential at the trapping region to be accurate.

Results for Spherical Electrode

The compensation field created at the trap centre by applying a potential V to the spherical electrode is calculated to be $-0.00122 \cdot V_c$ /mm. Its derivative along the direction to the compensation electrode is $-0.0059 \cdot V_c$ /mm^2, the second derivative $-0.017 \cdot V_c$ /mm^3 and the third derivative $-0.03 \cdot V_c$ /mm^4. These numbers do not capture the entire situation: the quadrupole component of the potential produced by the compensation electrode is oriented more along the trap axis than towards the compensation electrode. Evaluating it like the RF trapping potential with Eq. (2.15) reveals a stronger radial asymmetry of $2\epsilon \approx 30$ %. Table 2.7 summarises the calculated and the experimental results for compensation fields.

Close to the trap structure, the equipotential lines visible in Figure 2.18 are quite

Quantity	Value		Electrode	Direction	Method
v_1	-0.00730	(30)/mm	Oven	motional	ion displacement
v_1	-0.00143	(9)/mm	Counter e-Gun	motional	ion displacement
v_1	-0.00122	/mm	1 mm Sphere	motional	FEM calculation
v_1	-0.043	/mm	z-voltage	motional	FEM calculation
v_2	-0.0306	(6)/mm^2	Oven	strong	secular frequency
v_2	-0.0480	(20)/mm^2	Oven	weak	secular frequency
v_2	-0.0480	(60)/mm^2	Oven	motional	ion displacement
v_2	-0.0084	(20)/mm^2	Counter e-Gun	motional	ion displacement
v_2	-0.0059	/mm^2	1 mm Sphere	motional	FEM calculation
v_2	-0.0043	/mm^2	1 mm Sphere	$\perp$	FEM calculation
v_2	$+0.0102$	/mm^2	1 mm Sphere	trap axis	FEM calculation

Table 2.7: Compensation field and field derivative coefficients. The electric field produced by an electrode potential V_c is $v_1 V_c$, and its derivative $v_2 V_c$, both along a given direction. For experimental data, this direction is either along the observed ion motion or along one of the radial (strong or weak) trap axes. Calculated results are evaluated towards the compensation electrode which coincides with the calculated ion motion, perpendicular ($\perp$) to this direction or along the axial trap direction.

vertical (parallel to the trap axis). This indicates that even for the very inhomogeneous field produced by a small sphere, the inhomogeneity of the field at the trap centre is completely determined by the shielding effect of the trap electrodes. Any compensation electrode shape at a similar distance from the trap can thus be expected to produce a very similar ratio of field, field gradient and higher field derivatives at the trap centre. Thus the calculation results are presumably applicable not just to the comparably shaped counter electrodes each consisting of a wire end of 1 mm diameter, but also to the larger and more complicated oven and electron gun assemblies.

Results for z-voltage

I have also calculated the field for a potential difference V_c applied between the upper and lower of the outer (shield) electrodes of the trap (labelled z-voltage in Table 2.5, page 26 and in Table 2.7). This creates a field of $-0.043 \cdot V_c$ /mm, its derivative along the trap axis vanishes due to the symmetry and the second derivative is $3 \cdot V_c$ /mm^3.

Conclusion

The compensation potentials obtained by experiment in Section 2.3.3 and by calculation in this section are compatible. The spherical electrode used for calculations has less area than any of the real compensation electrodes, but it is a good approximation to the cylindrical ends of the counter electron gun electrode, which it matches in predicted values within $1.8\,\sigma$, where the deviation has the sign expected due to the lower area.

The calculation suggests that the exact shape of the electrodes has influence mostly on the magnitude, but less on the shape of the potential produced in the trapping region. The ratios of field to field gradient are compatible with this: The calculated scale length over which the field varies, $v1/v2$, is 210 to 280 μm, depending on direction. The one found experimentally for the counter electrode to the electron gun is 170 (40) μm and for the very different oven geometry a range of 150 (10) to 240 (10) μm has been observed. That is a deviation in the field shape (as quantised by the length scale) of 30 % where the magnitude of the field differs by a factor of six.

Notably, the compensation electrodes create a much higher field inhomogeneity in the present trap than were observed by Schneider (2005) for comparable electrodes in a trap built to the design of Beaty (1986b). Measured in terms of the quadrupole strengths (field gradients) created by applying the correct compensation voltages, the field inhomogeneity is two orders of magnitude larger in the new trap. With values exceeding $1 \text{ V}/\text{mm}^2$, they are also larger than the quadrupole stray potentials observed. For the intended application in an optical frequency standard, it would be necessary to reduce these static quadrupole potentials. For this purpose, electrode and counter electrodes can be placed at the voltage levels where their quadrupole potentials cancel. If compensation electrodes and their counter electrodes were built as exact mirror images, these potentials would be particularly easy to determine: an opposite potential of equal magnitude would have to be applied to the other.

2.4 Anharmonicity in Secular Motion

The anharmonicity in the trap potential adds a Duffing nonlinearity to the secular motion, as described by Eq. (2.20a) on page 14. Here, I compare theoretical predictions presented in Section 2.4.1 with experimental findings reported in Section 2.4.2.

2.4.1 Duffing Oscillator

The mass-on-a-spring oscillator with a spring that hardens or softens with amplitude (spring constant $k = k_0 + k_2 x^2$) is called Duffing oscillator. Duffing (1918) discussed it for small perturbations from the harmonic case ($k_2 x^2 \ll k_0$), as relevant for the trap design presented in the preceding section. As can be expected from the amplitude-dependent spring constant, he found an amplitude-dependent eigenfrequency and bistability in the driven system. The bistability arises from a sufficiently large amplitude dependence of the resonance frequency, such that the same excitation frequency can be either on or off resonance, depending on the history of the system.

Viscously Damped Duffing Oscillator

To derive a quantitative expression for these effects, I will follow Duffing's ansatz of an iterative solution, as more concisely presented by Enns and McGuire (2001). My parametrisation of the Duffing oscillator's equation of motion is

$$\ddot{x} = -\gamma \dot{x} - \omega_0^2 x - \eta x^3 + F \cos\left(\omega t + \delta\right). \tag{2.30}$$

For a mass m, the viscous damping strength γ leads to a damping force $F = -\gamma m \dot{x}$. The small-amplitude resonance frequency is $\omega_0 = \sqrt{k_0/m}$ and $\eta = k_2/m$ parametrises the nonlinearity in the spring constant. I use δ to describe the phase lag between an oscillatory excitation force of amplitude mF and the resulting motion by constraining the latter's phase. As starting point for an iterative solution, I take the exact solution in the limit of no anharmonicity:

$$x_0 = \lim_{\eta \to 0} x = A \cos(\omega t). \tag{2.31}$$

In this zero-order approximation, the phase lag δ is already determined, but must be kept as variable to capture a higher order effect. The next approximation x_1 is obtained by substituting $x = x_0$ into the right hand side of Eq. (2.30) and $\ddot{x} = \ddot{x}_1$ in the left hand side:

$$x_1 = A_1 \cos(\omega t) + B_1 \sin(\omega t) + \frac{1}{36} \frac{\eta}{\omega^2} A^3 \cos(3\omega t), \tag{2.32}$$

$$A_1 = \omega^{-2} \left(\omega_0^2 A + \frac{3}{4} \eta A^3 - F \cos \delta \right),$$

$$B_1 = \omega^{-2} \left(-\gamma \omega A + F \sin \delta \right).$$

The correct value for the amplitude of the zero-order approximative solution Eq. (2.31) is $A = A_1$ for a phase lag δ such that $B_1 = 0$. Substituting these two equations into Eq. (2.32) yields the relationship between excitation $F \cos(\omega t + \delta)$ and motion $x \approx A \cos \omega t$:

$$F = \sqrt{\left(\left(\omega_0^2 - \omega^2 \right) A + \frac{3}{4} \eta A^3 \right)^2 + (\gamma \omega A)^2}, \tag{2.33a}$$

$$\tan \delta = \frac{\gamma \omega A}{\left(\omega_0^2 - \omega^2 \right) A + \frac{3}{4} \eta A^3}. \tag{2.33b}$$

The amplitude is no longer a unique function of the excitation parameters. There are now up to three positive amplitudes A allowed by Eq. (2.33a), one of which is not stable against perturbations, causing the Duffing oscillator to be bistable. The resonance spectrum $A(\omega; F)$ is shown in Figure 2.19.

The maximum amplitude occurs at a phase lag of $90°$, so the amplitude dependence of the resonance frequency ω_r can be extracted from Eq. (2.33b) by setting the denominator zero:

$$\omega_r = \sqrt{\omega_0^2 + \frac{3}{4} A^2 \eta} \approx \omega_0 + \frac{3}{8} \frac{\eta A^2}{\omega_0}, \tag{2.34a}$$

$$\omega_r \approx \omega_0 + \frac{3}{8} \frac{\eta F^2}{\gamma^2 \omega_0^3}. \tag{2.34b}$$
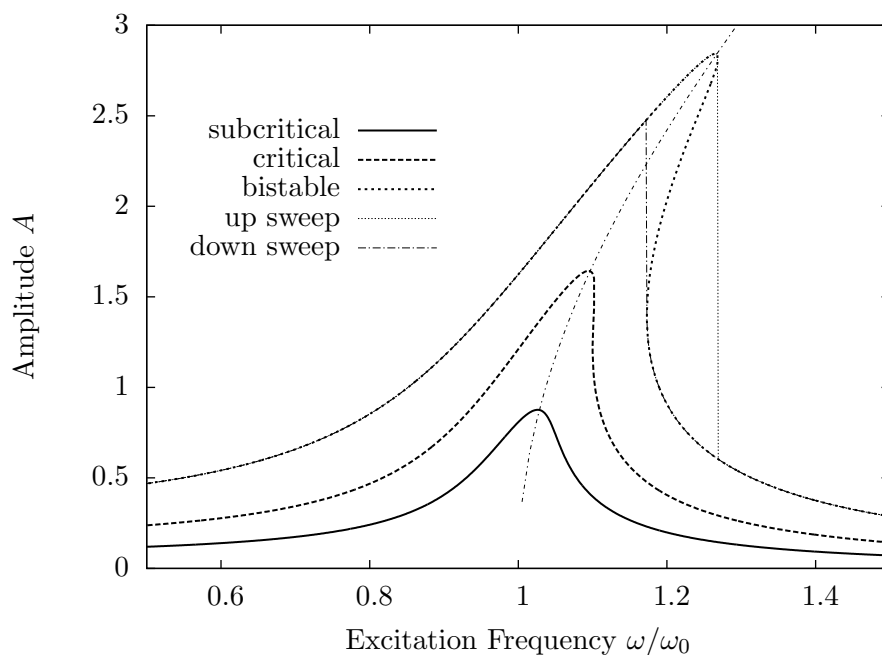
Figure 2.19: Resonance curve $A(\omega; F)$ of a driven Duffing oscillator. Three different strengths F of the driving force are shown, corresponding to subcritical, critical and bistable behaviour. The thick curves show stationary (mathematical) solutions. In an experiment, a spectrum represented by the thin curves might be observed, if the frequency is scanned sufficiently slowly to allow the system to reach its stationary oscillation amplitude at all frequencies.

Nonlinearly Damped Duffing Oscillator

To describe the damping an ion cloud experiences in a buffer gas, I have extended the forced Duffing oscillator Eq. (2.30) with a velocity-squared damping term:

$$\ddot{x} = -\gamma\dot{x} - \gamma_2 \operatorname{sgn}(\dot{x})\, \dot{x}^2 - \omega_0^2 x - \eta x^3 + F\cos(\omega t + \delta). \qquad (2.35)$$

Following the ansatz of the previous section, the first-order solution, Eq. (2.32), must be altered by including a term $-\omega_0^{-2}\omega^2 A^2 |\sin\omega t| \sin\omega t$. Numerically, I found

$$|\sin\alpha|\sin\alpha = 0.848826\ldots \left(\sin\alpha - \frac{\sin 3\alpha}{5} - \frac{\sin 5\alpha}{5\cdot 7} - \frac{\sin 7\alpha}{3\cdot 5\cdot 7} - \frac{\sin 9\alpha}{3\cdot 7\cdot 11} + \ldots \right). \qquad (2.36)$$

Keeping only the first term of this Fourier expansion, the first-order solution to the nonlinearly damped Duffing oscillator Eq. (2.35) is

$$x_1 = A_1 \cos(\omega t) + B_1 \sin(\omega t) + \text{ terms of frequency } 3\omega \text{ and higher,} \qquad (2.37)$$

$$A_1 = \omega^{-2} \left(\omega_0^2 A + \frac{3}{4}\eta A^3 - F \cos\delta \right),$$

$$B_1 = \omega^{-2} \left(-\gamma\,\omega A - 0.848826\gamma_2\,\omega^2 A^2 + F \sin\delta \right).$$

The comparison to the zeroth order solution Eq. (2.31) again sets constraints on A_1 and B_1. These determine the relationship between the excitation amplitude F and the oscillation amplitude A:

$$F = \sqrt{ \left(\left(\omega_0^2 - \omega^2\right) A + \frac{3}{4}\eta A^3 \right)^2 + \left(\gamma\,\omega A + 0.848826\,\gamma_2\,\omega^2 A^2\right)^2 }. \qquad (2.38)$$

Duffing Coefficients for Secular Motion

The leading expected effect of anharmonicities on secular motion is, according to Eq. (2.20a), a Duffing nonlinearity. The coefficients from Eq. (2.30) of my theoretical treatment of the Duffing oscillator are:

$$\omega_0^2 = \omega_{x,y,z}^2 = \frac{1}{8}\Omega^2 \left(q_{x,y,z}^2 + 2a_{x,y,z} \right) \approx \left(q_{x,y,z}^2 + 2a_{x,y,z} \right) \cdot 1.30 \cdot 10^{15} \text{ s}^{-2}, \qquad (2.39a)$$

$$\eta_{x,y} = -\frac{3}{8}\frac{a_{40}}{a_{20}}\frac{\Omega^2}{z_0^2} \left(8q_{x,y}^2 + a_{x,y} \right) \approx -a_{40} \left(8q_{x,y}^2 + a_{x,y} \right)(1{\pm}\epsilon) \cdot 2.09 \cdot 10^{23} \text{ m}^{-2}\text{s}^{-2}, \qquad (2.39b)$$

$$\eta_z = +\frac{1}{2}\frac{a_{40}}{a_{20}}\frac{\Omega^2}{z_0^2} \left(8q_z^2 + a_z \right) \approx a_{40} \left(8q_z^2 + a_z \right) \cdot 2.79 \cdot 10^{23} \text{ m}^{-2}\text{s}^{-2}, \qquad (2.39c)$$

$$F_{x,y} = \frac{e}{m}v_1 V_c \cos\alpha_{x,y} \approx V_c \cdot 8.1(5) \cdot 10^5 \text{ ms}^{-2}\text{V}^{-1} \cdot \cos\alpha_{x,y}. \qquad (2.39d)$$

Eq. (2.39d) assumes a voltage V_c applied to a counter electrode, sitting at an angle $\alpha_{x,y}$ to the axes x and y along which secular motion occurs.

2.4.2 Experimental Lineshapes

I have looked for signatures of a Duffing oscillation by recording resonance spectra for secular motion excited by applying a RF signal to either the counter electrode to the electron gun, or to one of the outer electrodes of the trap. 369 nm fluorescence rates were measured versus excitation frequency for different excitation amplitudes. Figure 2.20 shows such spectra.

For stronger forcing, the lineshape becomes asymmetric. The maximum change in the fluorescence occurs at increasingly higher frequencies for the radial resonances and for the axial frequencies at increasingly lower frequencies. These properties are expected from a Duffing oscillator for a negative octupole strength a_{40}, as predicted for the trap.
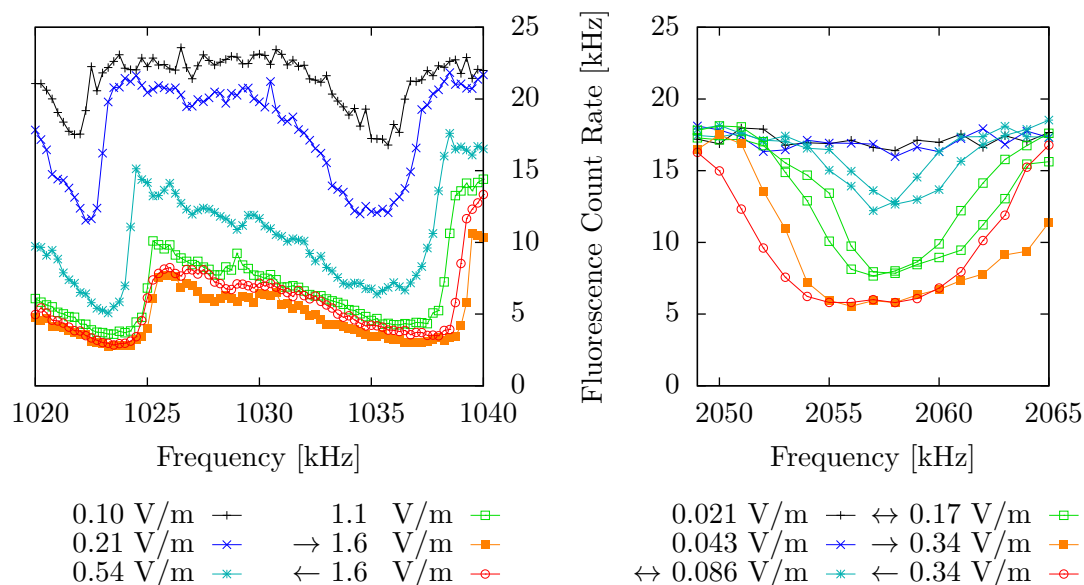
Figure 2.20: Secular motion spectra. The fluorescence count rates were recorded whilst a RF excitation frequency was swept across the resonance. Its strength is given as field amplitude (at the trap centre). The sweep for the axial resonance curve (right plot) was much faster (0.5 s per frequency step of 1 kHz) than for the radial one (left plot, 2 s per frequency step of 0.25 kHz). The difference between up- and down-sweep in the axial resonance curve can thus be explained by slow dynamics even in the absence of bistability.

2.4.3 Model

Viscously Damped Duffing Oscillator Model

Assuming the secular motion to be a Duffing oscillation with the simplest kind of damping, a viscous drag, causes the maximum excitation amplitude to be proportional to the excitation level. As the observed relative change in the fluorescence rate scales inversely to the excitation level, I have used the inverse fluorescence rate as an indicator of oscillation amplitude. A fit to the amplitude of a Duffing oscillator is shown in Figure 2.21. This model at best reproduces the characteristic frequencies where a sudden change of the signal's magnitude occurs and only under the assumption that only the lower branch is relevant. The overall shape of the resonance curves are only reproduced for weak excitation. For stronger excitation, the model then predicts a larger shift in the resonance frequency than seen experimentally. It also predicts bistability, which was not reproduced experimentally.

43
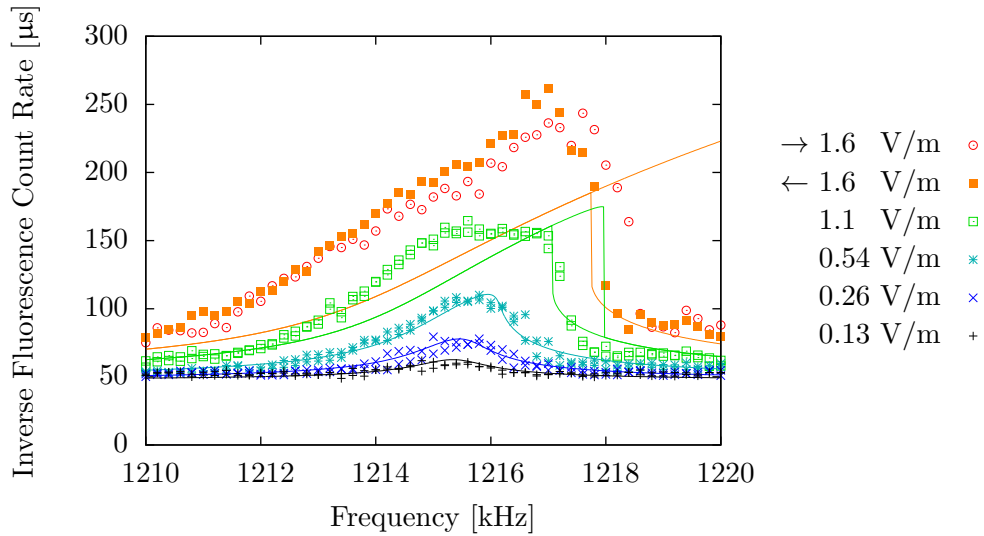
Figure 2.21: Viscously damped Duffing oscillator fit to secular motion. Symbols indicate inverse fluorescence rates, measured at trap parameters $q_z = 0.156$ and $a_z = -0.0188$ with a Helium buffer gas pressure of 10^{-6} mbar. Lines correspond to the resonance spectrum of a Duffing oscillator with parameters fitted to reproduce the measurements at the lowest three excitation strengths. Note the extreme bistability predicted by this model for the larger excitation strengths.

Nonlinearly Damped Duffing Oscillator Model

An effect that reduces both the bistability and the maximum amplitude is nonlinear damping. It is physically plausible, as a velocity-proportional average drag is expected only for motion slow compared to the thermal velocities. At large ion cloud velocities, the average force exerted by collisions with buffer gas becomes proportional to the square of the velocity, as both collision rate and the average momentum transferred in each collision are then proportional to it.

If nonlinear damping is significant in the system, the amplitude will grow less than linearly with the excitation level. The empirical model for the relationship between amplitude and fluorescence must be revised to reflect this. I model the loss of fluorescence as a spatial effect of the ion cloud moving out of a Gaussian laser beam. The probability density function $P(x)$ of a harmonic oscillation $x = A \cos \omega t$ is

$$P(x) = \mathcal{N} \left| \frac{1}{\dot{x}} \right| = \frac{1}{\pi \sqrt{A^2 - x^2}}.$$

The predicted relative fluorescence rate r from a cloud oscillating at the amplitude A in a Gaussian beam profile (or convolution of such a beam profile with a Gaussian cloud
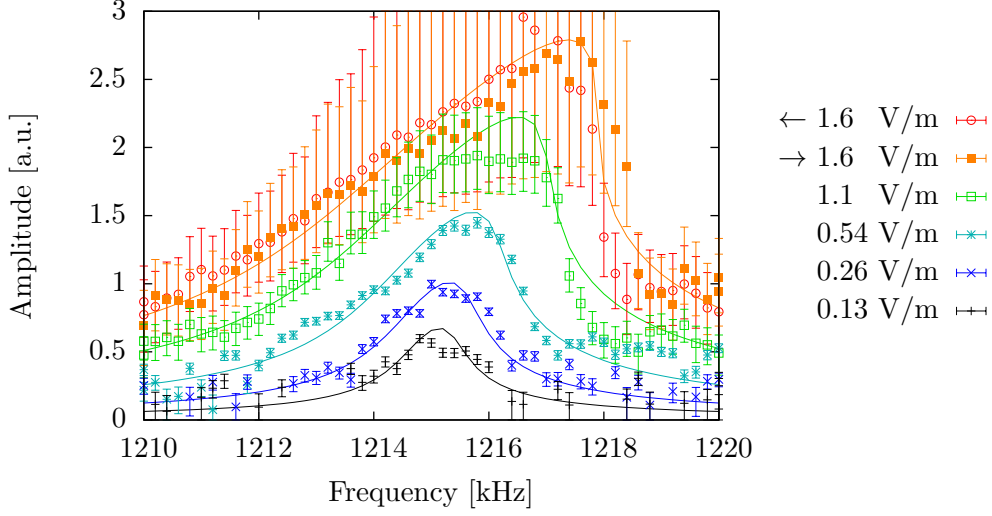
Figure 2.22: Nonlinearly damped Duffing oscillator fit. Secular motion was excited via the counter electrode to the e-gun and measured fluorescence change converted to an amplitude in units of an interaction radius w. Trap parameters were $q_z = 0.156$ and $a_z = -0.0188$. The Helium buffer gas pressure was 10^{-6} mbar. Error bars indicate the effect of uncertainties in background and undisturbed count rate. Curves are drawn for the following parameters: $\omega_0 = 7.6341 \cdot 10^6$ rad/s, $\eta = 1.66 \cdot 10^{21}$ m^{-2}s^{-2} (14.4 times the maximum value expected), $\gamma = 2000$ s^{-1}, $\gamma_2 = 180$ m^{-1}, $w = 4.9$ µm. The driving strength $F = 8.07 \cdot 10^5$ ms^{-2}V^{-1} is that expected if the trap axis points 30° away from the electrode used for excitation.

density) with $1/e$ radius w is

$$r(A) = \frac{1}{\sqrt{\pi}} \int\limits_{-A}^{+A} \mathrm{d}x P(x) e^{-(x/w)^2}. \tag{2.40}$$

I have translated observed fluorescence count rates to amplitudes in units of an interaction radius w (combined beam and cloud size). Fitting the theoretic behaviour of a nonlinearly damped Duffing oscillator to this data results in good agreement between fit and measurement. Both are shown in Figure 2.22.

Quantitative Discussion

The parameters used to obtain the curve in Figure 2.22 can be scaled whilst changing only the resulting amplitude. This scaling by a factor a is:

$$F \to aF \qquad w \to aw \qquad \eta \to a^{-2}\eta \qquad \gamma \to \gamma \qquad \gamma_2 \to a^{-1}\gamma_2 \tag{2.41}$$

Otherwise the parameters are determined by the resonance curve. To obtain values independent of the above scale factor, one of them has to be chosen.

The driving force applied via the counter electrode to the electron gun can be determined from Table 2.7 and measured voltages at the vacuum feedthrough. The resulting other parameters are given in Figure 2.22. They are not plausible: the waist radius is five times smaller than the width of the laser beam employed, and more than ten times smaller than observed cloud sizes, as ion clouds typically extend to or beyond the $130\,\mu\mathrm{m}$ size of a camera image. Further, the cross-over velocity between viscous and velocity-squared damping $\gamma/\gamma_2 \approx 11\,\mathrm{m/s}$ should be on the order of the thermal velocities between collisional partners ($\approx$ km/s for Helium buffer gas atoms). The resulting trap anharmonicity is also too large by at least an order of magnitude compared to calculations.

Assuming the driving level to be twenty times larger would yield somewhat plausible parameters for the same lineshapes as shown in Figure 2.22: the anharmonicity becomes 0.036 times of that calculated for the trap as built, much closer to the calculated anharmonicity of the trap as designed than as built. The cross-over velocity is then $220\,\mathrm{m/s}$ and the Gaussian radius w is $97\,\mu\mathrm{m}$, compatible with actual ion cloud sizes.

Conclusion

An ion trap with reduced anharmonicity has been designed and built for use in a frequency standard. Because of fabrication deviations, the anharmonicity is expected to far exceed that of the original design. This prediction has been verified qualitatively in observed lineshapes of secular motion resonances: lineshape and sign are compatible with the predicted Duffing oscillation under nonlinear damping. But a quantitative agreement with all known conditions could not be achieved.

3 Noise in Resonators

3.1 Introduction

Optical frequency standards rely on highly stable lasers. It is state-of-the-art to reduce their linewidths by frequency-locking to a reference cavity. Fluctuations (noise) of its resonance frequency is transferred to the laser frequency. Figure 3.2 on page 49 gives an overview of different sources of noise; the remainder of this section briefly introduces them.

The noise source that presently limits the performance of optical frequency standards is Brownian motion. Accordingly, I devote the bulk of this chapter to this phenomenon. Section 3.2 discusses the mechanism and the three published calculation methods. Section 3.3 then summaries published material properties needed for the calculation and presents calculation results. My original contribution consists of calculating Brownian motion noise for Gauss-Hermite modes, which is reduced compared to the fundamental Gaussian mode. To realize such a reduction, it is desirable to selectively couple to a single high-order Gauss-Hermite mode. In Section 3.4, I report on the selective experimental excitation of such modes in a resonator.

Reference Resonators

A typical clock laser reference resonator consists of a spacer that holds the two mirrors via an optical contact, see Figure 3.1. Frequency fluctuations $\Delta\nu$ of the resonance frequency $\nu = \nu_0 + \Delta\nu$ of an optical cavity arise because the optical path length $L = L_0 + \Delta L$ of the resonator round-trip varies over time. After one cavity round-trip with optical path length $L_0 + \Delta L$, a monochromatic intracavity light field of frequency ν_0 has accumulated a phase difference $\Delta\phi$ to the resonant condition (zero phase) at the nominal round-trip length L_0. The relation between these fluctuations is, to first order, i.e. for small fluctuations:

$$\frac{\Delta\nu}{\nu} = -\frac{\Delta L}{L} = -\frac{\Delta\phi}{2\pi L/c}$$

Amplitude fluctuations caused by the resonator itself are less important: Amplitude fluctuations affect the frequency stabilisation only indirectly. Further, they are not intrinsically present to the same extent as phase fluctuations. Small unavoidable fluctuations inside a resonator with dielectric mirrors, such as a changing thickness d of individual coating layers, will create phase fluctuation to the first order in Δd, but changes in reflectance, transmittance and absorption only to the second order in Δd.
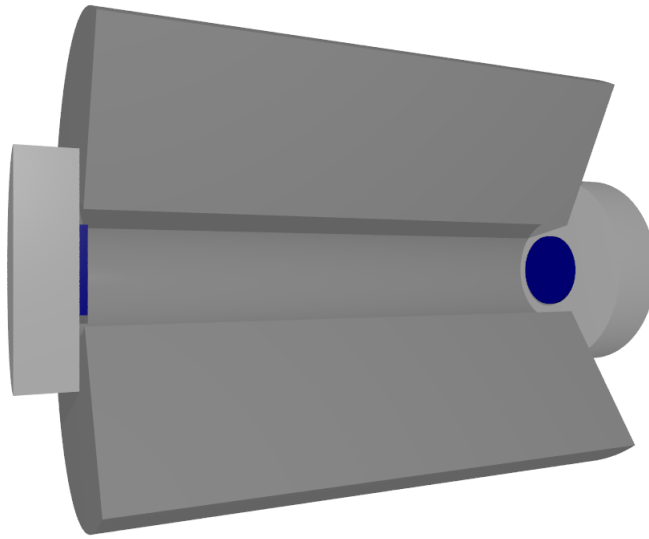
Figure 3.1: Clock laser reference resonator. A spacer (dark grey) is optically contacted to two mirror substrates (light grey). Part of the substrates' inner surfaces is made highly reflective by a dielectric coating (dark blue). For clarity, the Resonator is drawn cut-open with different cuts for the individual constituent parts and the coating's thickness is exaggerated.

3.1.1 Technical Noise

Power Fluctuations

Amplitude fluctuations of the intracavity field can impart phase fluctuations in the resonator by heating the resonator mirrors which then expand thermally, changing the cavity length. The light coupled into the resonator has to be sufficiently power-stabilised to suppress this effect.

Acceleration

Amongst technical noise sources are furthermore mechanical motions of the resonator that are excited by external forces. These can be quasistatic forces such as tidal forces or seismics deforming the resonator, or acoustic vibrations that can additionally excite mechanical resonances in the resonator.

Drifts

There are two important sources of frequency drift in the reference resonators used for laser stabilisation. One is thermal expansion of the entire resonator due to residual temperature changes. A crude estimate for this effect can be obtained from practical limits for the temperature stabilisation: The achievable time constant for thermal equilibration
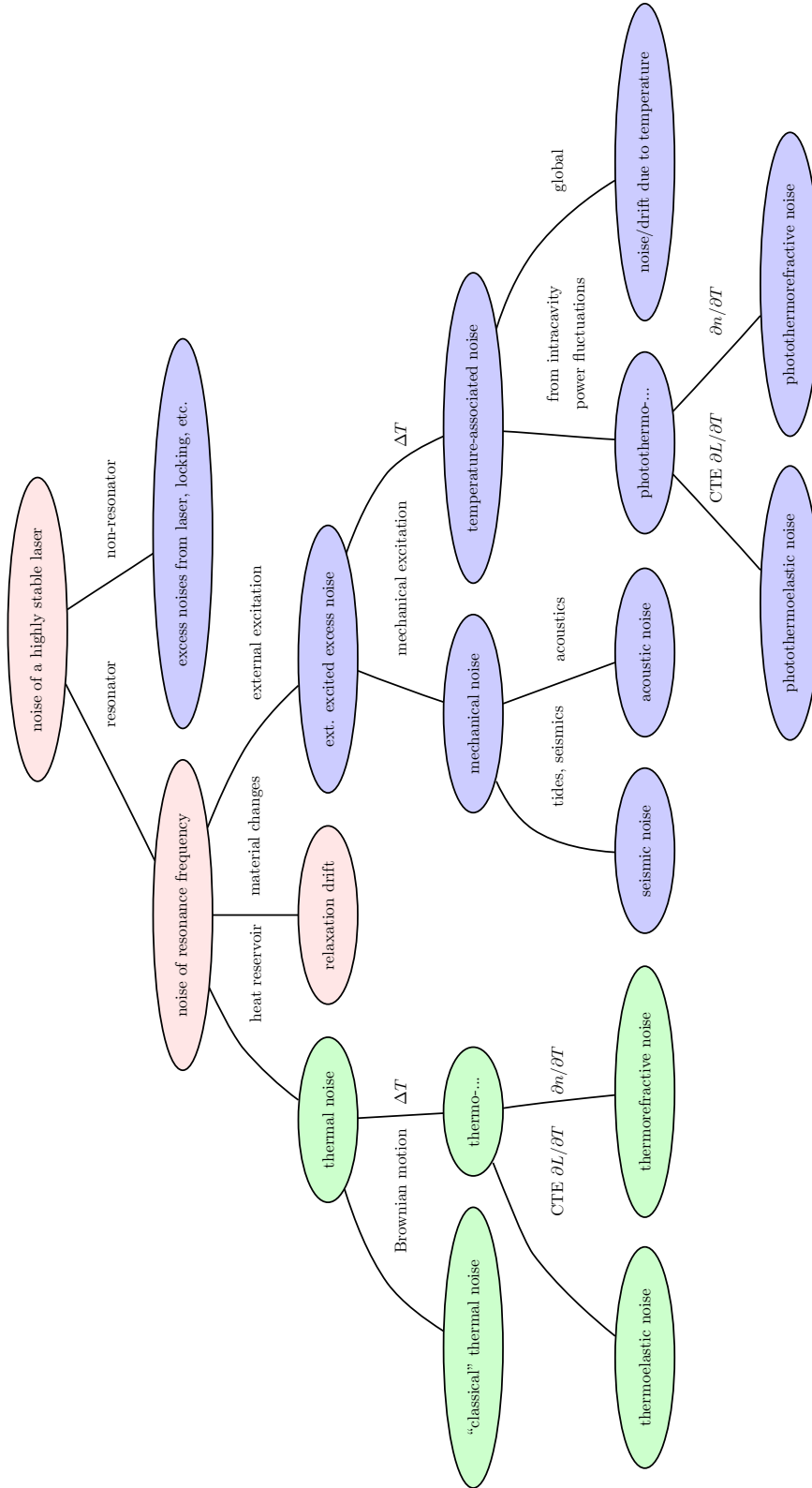
Figure 3.2: Types of noise affecting a highly stable laser. Nodes name particular noise contributions, edges (the connecting lines) name their origins. Excess or technical noise is shaded blue, fundamental thermodynamic noise green.

in a vacuum-flask-type setup is limited to days by the minimum emissivity of metals for room temperature thermal radiation, $\lesssim 0.01$, and the heat capacity (per area) of metal sheets of practical thickness. Temperature stabilisation to within 10 to 15 μK over time periods of days has been reported (Dratler, 1974; Sarid and Cannell, 1974), but more typical values are several times larger for reasonable design complexity (Unni et al., 2003). These results are not from setups for housing a resonator. For such a system, Alnis et al. (2008) reports temperature excursions of $1mK$. To get a crude estimate of the effect of imperfect temperature stabilisation, I will assume a constant temperature difference of $\Delta T = 100\mu K$ between resonator and outer layer of a temperature isolation with time constant of just over a day ($\tau = 10^5$ s). The reference resonator built in my group (Sherstov et al., 2010) has a time constant of at least one day. For Corning ultra-low expansion glass ceramics (ULE$^{©}$) with a thermal expansion of approx. $\alpha = 10^{-8}/K$ when used 10 K away from its zero thermal expansion temperature, this results in a linear drift in resonator length by a factor of

$$\frac{\partial}{\partial t}\frac{\Delta L}{L_0} = \frac{\alpha \Delta T}{\tau} \approx 10^{-17} \text{ /s.} \tag{3.1}$$

For times approaching the thermal equilibration time, the temperature stabilisation's action arrives at the stabilised volume, invalidating the premise of a somewhat constant temperature difference. A linear temperature drift is thus expected for timescales on the order of days for state-of-the-art systems.

The other cause of length drift in a resonator is temporal changes in the material: Recrystallisation, viscous flow or even outgassing may occur in the ULE glass ceramic and joints may creep, relaxing stresses introduced in optical contacting. Berthold III et al. (1977) has characterised these effects by measuring the frequency drift in optically contacted resonators made from different low-expansion materials with as few as possible optical contacts and with additional optical contacts. He finds a total length decrease per optical contact of 2.2 nm, most of which occurs during the first 60 days. This relaxation seems to have essentially stopped after 5 months. Whilst Berthold III et al. (1977) explicitly reports the length changes of six different materials, he omits giving such a numerical result for Corning 7971 ULE glass, but reproduces values ranging from $\dot{L}/L = -1.7(\pm 0.3) \times 10^{-10}/$d to $-3.8(\pm 1.4) \times 10^{-10}/$d from other sources. From his own measurements, a value of $\dot{L}/L \approx -1 \times 10^{-10}/$d can be inferred.

The total frequency drift of the PTB group's 934 nm laser, as reported by Sherstov et al. (2010), corresponds to $\dot{L}/L = -0.9 \cdot 10^{-11}$ /d, Hosaka et al. (2009) reports on a laser at the same wavelength with $\dot{L}/L = -1.3 \cdot 10^{-11}$ /d and Stoehr (2005) found a total frequency drift corresponding to $\dot{L}/L = -1.4 \cdot 10^{-11}$ /d in a 657 nm laser. This observed length change is two orders of magnitude lower than the initial length change inferred from Berthold's measurement of the settling of optical contacting: Two optical contacts in a 7.5 cm long resonator (as used in our 934 nm laser) should lead to an initial cavity length change of $\dot{L}/L \approx -10^{-9}$ /d.

Summary

External influences and shrinking of the material that the resonator is made of change its frequency. In as much as these effects have an unpredictable or uncompensated component (e.g. a deviation from a compensated linear or quadratic drift), they cause technical noise. In theory, it could be eliminated almost completely; in practice, it can be suppressed or compensated sufficiently to be currently negligible for the performance of clock lasers.

3.1.2 Noise Caused by Thermodynamic Fluctuations

There are also internally generated fluctuations acting on the resonator that fundamentally cannot be eliminated or suppressed in the way technical noises can or might be: contact to a heat reservoir causes fluctuations, a situation that can never be avoided completely. Coupling to a heat reservoir implies a dissipative process, a relation that can be quantified in the fluctuation-dissipation theorem to be introduced in Section 3.2.1.

Fluctuations of this kind that are relevant to reference resonators are fluctuations of mechanical displacement (Brownian motion) and of temperature. The former immediately imply cavity length fluctuations, the latter indirectly: temperature changes couple to length via thermal expansion (thermoelastic noise) or to optical path length through the temperature dependence of the index of refraction (thermorefractive noise). Thermoelastic noise vanishes for a material without thermal expansion such as ULE operated at its zero-CTE temperature and thermorefractive noise is only relevant in the coating.

With Levin's calculation method to be introduced in Section 3.2.3, it is possible to separately treat the contributions from different regions of the resonator to each of these classes of noise. As there is a different scaling with beam size for the mirror's coating (it is effectively 2-dimensional), the mirror's substrate (3-dimensional) and the spacer (1-dimensional), it is indeed convenient to divide each noise class into subclasses for each of these regions.

This spatial subdivision leads to an entire "zoo," (Gorodetsky, 2008) of noise sources. The following occur in clock resonators, in approximate order of importance:

- Substrate Brownian Motion Noise

- Coating Brownian Motion Noise

- Spacer Brownian Motion Noise

- Coating Thermoelastic Noise

- Coating Thermorefractive Noise

- Substrate Thermoelastic Noise

- Spacer Thermoelastic Noise

I have omitted from this list technical noise sources such as coating and substrate photothermoelastic noise and coating photothermorefractive noise, all of which Gorodetsky includes in his zoo. Also omitted is the fundamentally present thermoradiative noise caused by blackbody radiation because it is small compared to thermoelastic and thermorefractive noises provided thermal conduction exceeds thermal radiation. At relevant size and time scales, this condition is well fulfilled.

3.2 Brownian Motion: Calculation Methods

The collective motion associated with Brownian motion affects the resonator length. This "Brownian motion" thermal noise is often just called "thermal noise" for historic reasons: although it is only one amongst many thermal noise sources, it was the first one to be identified as relevant in the context of gravitational wave detectors,[1] see e.g. Gorodetsky (2008).

The effect of small axial deformations of the surface of a resonator's mirror has been treated by Gillespie and Raab (1995), finding a phase shift (corresponding to a shift in resonance frequency) as only first-order effect. After displacing points $\vec{r}$ on the mirror surface axially by a distance $x(\vec{r})$, the new field is

$$E_{\text{new}}(\vec{r}) = E(\vec{r})e^{2\imath k x(\vec{r})} = E(\vec{r})\Big(1 + 2\imath k x(\vec{r}) + \dots\Big) \tag{3.2}$$

where $E(\vec{r})$ is the field of the resonating mode for an undeformed mirror and $k = 2\pi\lambda$ is the length of the light's wave vector. Normal incidence on the mirror is assumed. A modal expansion of the new field in terms of the undisturbed modes, of which only the initial mode needs to be considered, yields

$$E_{\text{new}}(\vec{r}) = E(\vec{r})\left(1 + \frac{2\imath k}{I_0}\int\limits_{\text{ms}} x(\vec{r}')E(\vec{r}')E^{\star}(\vec{r}')\mathrm{d}\vec{r}' + \dots\right). \tag{3.3}$$

The integral extends over the mirror surface (ms). The incident power $I_0 = \int\limits_{\text{ms}} I(\vec{r})\mathrm{d}\vec{r}$, expressed using the intensity $I(\vec{r}) = E(\vec{r})E^{\star}(\vec{r})$, arises as normalisation constant in the modal expansion. According to Eq. (3.3), to first order in the small deformation of the mirror surface, the reflected field is the same as if the entire mirror was displaced by an effective distance x, given by the intensity-weighted local mirror deformation as

$$x = \frac{1}{I_0}\int\limits_{\text{ms}} x(\vec{r})I(\vec{r})\mathrm{d}\vec{r}. \tag{3.4}$$

For the effective mirror displacement of Eq. (3.4), mechanical resonances matter, as they filter the noise. The following Section 3.2.1 addresses this issue by deriving a general expression for these fluctuations from the system's conductance and the fluctuation-dissipation theorem. Actual values can be calculated in several ways. The modal expansion method presented in Section 3.2.2 takes individual mechanical modes into account

---

[1]The qualification of known relevancy to interferometry is necessary. A different source of thermal noise, thermoelastic dissipation, had already been predicted by Zener (1937).

and was the first calculation method known. Whilst noise estimates at arbitrary frequencies can be derived, these estimates can be quite inaccurate. A direct calculation method based on the fluctuation-dissipation theorem is known, which does not explicitly involve a modal expansion. For the low-frequency noise (as compared to acoustic resonance frequencies) that is relevant both to clock resonators and gravitational wave detectors, it becomes particularly simple, as then not even an implicit modal expansion is needed. This direct method is introduced in Section 3.2.3. This is the best known method if the effect of a finite sized mirror is to be modelled. However, even for the case of maximum diffraction-limited beam size for a given mirror that occurs for gravitational wave detectors, it can be sufficient to approximate the mirror as infinite. In this case, the effect of beam shape on the low-frequency noise can be expressed in a particularly simple fashion, as shown in Section 3.2.4.

3.2.1 Mechanical Resonances

Dissipation

Consider a point-like mass m in a one-dimensional linear mechanical system, its translation x away from the equilibrium position and an external force F acting on it. Because of the stipulated linearity of the system, in Fourier space, there must be a linear relationship between external force $\tilde{F}(\omega)$ and resulting translation $\tilde{x}(\omega)$ or resulting velocity $\tilde{\dot{x}}(\omega)$:

$$\tilde{x}(\omega) = H(\omega)\tilde{F}(\omega), \tag{3.5a}$$

$$\tilde{\dot{x}}(\omega) = Y(\omega)\tilde{F}(\omega). \tag{3.5b}$$

By considering the external force $\tilde{F}(\omega)$ an input to the system and the resulting translation $\tilde{x}(\omega)$ the system's response, $H(\omega)$ becomes the frequency response function of the system. Then $Y(\omega) = \imath\omega H(\omega)$ is the system's admittance and its inverse, $Z(\omega) = Y^{-1}(\omega)$, is the system's impedance.

The external force does work on the system; the time-average of the transferred power, $P = \left\langle \frac{\partial}{\partial t}(xF) \right\rangle_t$, is in Fourier space:

$$\tilde{P}(\omega) = \tilde{\dot{x}}(\omega)\tilde{F}(\omega) + \tilde{x}(\omega)\tilde{\dot{F}}(\omega) = 2\,\tilde{\dot{x}}(\omega)\tilde{F}(\omega) = 2\,Y(\omega)\tilde{F}^2(\omega). \tag{3.6}$$

This power must be dissipated in the system. The force $F_0\,cos(\omega t)$ leads to a time-averaged dissipation

$$P_0(\omega) = F_0^2\,\mathrm{Re}[Y(\omega)]. \tag{3.7}$$

The real part of the admittance, $\mathrm{Re}[Y(\omega)]$, is called conductance.

Thermal Excitation and Fluctuation Dissipation Theorem

By the equipartition theorem, the total thermal energy averages to $k_B T$ per degree of freedom and thus per mechanical vibration mode. For a harmonic oscillator, the energy in the single oscillation mode divides equally into a kinetic and a potential term of $\frac{1}{2}k_B T$

(time-averaged) each. The resulting deflection, expressed using the spring constant k, is described by

$$\langle x^2 \rangle = k_B T / k. \tag{3.8}$$

But what is the spectral distribution of the deflection caused by thermal excitation? The fluctuation dissipation theorem (Callen and Greene, 1952; Greene and Callen, 1952; Callen and Welton, 1951), hence abbreviated to FDT, allows to calculate these from the system's dissipative properties, which are described by its conductance $\mathrm{Re}[Y(\omega)]$:

$$S_x(\omega) = 4 \frac{k_B T}{\omega^2} \mathrm{Re}[Y(\omega)]. \tag{3.9}$$

An Intuitive Generalisation: From Brownian Motion to FDT

An argument by Saulson (1990) suggests the FDT as generalisation of the more widely known characteristics of Brownian motion. Consider a particle with mass m that experiences a viscous frictional force $-f\dot{x}$. The particle's motion is described by the Langevin equation

$$m\ddot{x} + f\dot{x} = F_{\mathrm{th}}, \tag{3.10}$$

where F_{th} is a random, spectrally white force with

$$S_F(\omega) = 4k_B T f. \tag{3.11}$$

Noting that the system described by Eq. (3.10) has an impedance $Z(\omega) = \imath\omega m + f$ suggests a generalisation for arbitrary dissipation:

$$S_F(\omega) = 4k_B T \, \mathrm{Re}[Z(\omega)] \tag{3.12}$$

This is the fluctuation dissipation theorem for force fluctuations. Its equivalence to the one for displacement fluctuations, Eq. (3.9), can be seen by interchanging the labels "input" and "response" in Eq. (3.5) for force F_{th} and displacement x, respectively. In the following, I will only need the fluctuation dissipation theorem in the form of Eq. (3.9). This requires the mechanical conductance, which, for the Brownian motion described here, is

$$\mathrm{Re}[Y(\omega)] = \frac{f}{f^2 + m^2 \, \omega^2}. \tag{3.13}$$

Internally Damped Oscillation

Introducing a restoring spring force $\Delta F = -kx = -m\,\omega_0^2 \, x$ to the Brownian motion system Eq. (3.10) changes the conductance to

$$\mathrm{Re}[Y(\omega)] = \frac{f}{f^2 + m^2 \left(\omega - \omega_0^2/\omega\right)^2}. \tag{3.14}$$

This describes a harmonic oscillator with viscous damping $-f\dot{x}$. Such damping can be a good model if viscous drag from a surrounding medium is present and exceeds other

damping mechanisms. Such is the case for many pendula and high-Q micromechanical systems operated in air.

To model Brownian motion in a resonator operated in vacuum, a different—or altogether more general—damping must be considered. Replacing the damping coefficient f by a frequency-dependent term $k\,\omega^{-1}\tan\phi(\omega)$ is convenient to model the general case because the internal damping arising inside bulk materials relevant for resonator construction may have a largely constant loss tangent $\tan\phi(\omega)$. The restoring force $F_{\text{restoring}}$, expressed in Fourier space, is then

$$\tilde{F}_{\text{restoring}}(\omega) = -k\left(1 + \imath \tan\phi(\omega)\right)\tilde{x}(\omega). \tag{3.15}$$

This damping results in a quality factor $Q = 1/\tan\phi(\omega_0)$. Expressed using the loss tangent, the mechanical conductance of the oscillator, Eq. (3.14), becomes

$$\mathrm{Re}[Y(\omega)] = \frac{1}{m}\frac{\omega\,\omega_0^2\,\tan\phi(\omega)}{\omega_0^4\,(\tan\phi(\omega))^2 + \left(\omega^2 - \omega_0^2\right)^2}. \tag{3.16}$$

For low noise applications only materials with low loss tangent can be used; I defer discussing actual material values to Section 3.3.1 on page 63. Their low loss allows approximating the loss tangent by the loss angle: $\tan\phi(\omega) \approx \phi(\omega)$. I use this small angle approximation for the remainder of this chapter.

3.2.2 Modal Expansion Method

Multiple Resonances

Real mechanical systems have multiple resonances. The displacement $x(\vec{r})$ at a position $\vec{r}$ is the superposition of modes $\psi_i(\vec{r})$:

$$x(\vec{r}, t) = \sum_i^\infty A_i \psi_i(\vec{r}) \cos(\omega_i t + \delta_i). \tag{3.17}$$

I assume the mode functions to be dimensionless and normalised according to

$$\int\limits_{\text{system}} \psi_i^2(\vec{r})\,\mathrm{d}^3\vec{r} = 1. \tag{3.18}$$

Thus the conductance pertaining to the motion $x(\vec{r})$ is also a superposition of each mode's conductance, Eq. (3.16), weighted by each mode's normalised mean square displacement $\psi_i^2(\vec{r})$:

$$\mathrm{Re}[Y(\omega; \vec{r})] = \sum_i^\infty \frac{1}{m}\frac{\psi_i^2(\vec{r})\,\omega_i^2\,\phi_i(\omega)\,\omega}{\omega_i^4\,\phi_i^2(\omega) + \left(\omega^2 - \omega_i^2\right)^2} \tag{3.19}$$

Here m is the system's total mass and ϕ_i is the loss angle of mode i. The reasons why the modal expansion method is largely abandoned for calculating thermal noise from mirrors will become clear in applying it.

Application

Consider the specialised but relevant case of a fundamental Gaussian mode in the exact centre of a mirror on a cylindrical substrate. The following arguments are again based on the review by Saulson (1990). The effective mirror displacement may be approximated by the displacement $x(\vec{r_0})$ at the central location $\vec{r_0}$ on the mirror surface. As modes with circumferential nodes also have a node at $\vec{r_0}$, only modes of circumferential order zero contribute. These have a somewhat constant weight $\psi_i^2(\vec{r_0}) \approx 2$. With this approximation, Eq. (3.19) and Eq. (3.9) result in an analytic estimate for the displacement noise:

$$S_{x(\vec{r_0})}(\omega) \approx 8\,\frac{k_B T}{\omega}\sum_{i=1}^{\infty}\frac{\phi_i(\omega)}{m\,\omega_i^2}. \qquad (3.20)$$

For describing the thermal noise in a resonator mode, the sum in Eq. (3.20) should be restricted to mechanical modes $\psi_i(\vec{r})$ that vary more slowly with $\vec{r}$ about $\vec{r_0}$ than the optical mode (e.g. Gillespie and Raab, 1995). The noise contribution of higher order mechanical modes will largely cancel as the optical mode samples both their hills and valleys (the integral in the exact Eq. (3.4) would be small). This consideration leads to one of the problems encountered in applying this method to optical clock resonators: unlike mirrors in gravitational wave detectors, which are not much larger than the optical modes incident on them, the mirrors and indeed connected mechanical structures of optical clock resonators are much larger than the resonant optical mode. Consequently, Eq. (3.20) would have to be evaluated for high-order modes $\psi_i(\vec{r})$ to become accurate. This aggravates the problem of accurately determining these modes and their loss tangents ϕ_i as boundary effects become increasingly important for short mechanical wavelengths. Yamamoto et al. (2002) have numerically shown good agreement with the direct method discussed in the following Section 3.2.3 for the case of homogeneous losses in the mirror substrate, whilst losses at the mirrored surface caused their modal expansion to severely underestimate thermal noise.

3.2.3 Direct Method

For rigid resonators or resonator mirrors, the mechanical resonance frequencies are much higher than the frequencies at which thermal noise is relevant. In this case, no modal expansion is necessary to determine the mechanical conductance for the effective displacement x of Eq. (3.4): it can be calculated for a quasi-static deformation.

González and Saulson (1994) used such a "direct" approach for calculating thermal noise in a wire suspension, albeit without a quasi-static approximation. González and Saulson (1995) then found excellent agreement between this prediction and a measurement in a pendulum. Levin (1997) adapted this method for mirror substrates, including an almost correct (Liu and Thorne, 2000) result for the length noise seen by a Gaussian mode. Levin's publication appears to be the cornerstone for further developments (e.g. Bondu et al., 1998; Braginsky et al., 1999; Liu and Thorne, 2000).

Estimation of the Mechanical Conductance from Deformation Energy

Levin's method calls for determining the elastic deformation energy W_E of the mirror when a force F_0 acts on it. Of this energy, a fraction given by $\phi\,W_E$ will be dissipated, if the force is applied quasistatically (slowly compared to the lowest mechanical resonance frequency). In a cyclic process with an applied force of $F = F_0 \cos \omega t$, the dissipated power is $P = \phi(\omega)\,\omega\,\pi^{-1}\,W_E$ and the conductance can be calculated from Eq. (3.7) as

$$\mathrm{Re}[Y(\omega)] = \phi(\omega)\frac{\omega}{\pi}\frac{W_E}{F_0^2}. \tag{3.21}$$

To use Eq. (3.21) with Eq. (3.9), the applied force needs to be the conjugate variable to the effective (intensity-weighted) mirror displacement x. As every localised displacement $x(\vec{r})$ has a force $F(\vec{r})$ localised at the same point $\vec{r}$ as its conjugate variable, the appropriate force F_0 has a pressure profile $p(\vec{r}_{\mathrm{ms}}) \propto I(\vec{r}_{\mathrm{ms}})$ with the same spatial distribution as the light intensity $I(\vec{r}_{\mathrm{ms}})$ used to weight the mirror displacement according to Eq. (3.4).

Rewriting the quantity W_E/F_0^2 in Eq. (3.21) using Eq. (3.5a) reveals it as equal to the frequency transfer function H. It is independent of the applied force F_0. In fact, $\phi(\omega)H$ expresses the strength of the coupling between translative motion x and the heat reservoir, and thus also the back action of the heat reservoir exerting a displacement (Brownian motion).

Some Theory of Elasticity

Here I present a few well-known aspects of elasticity to establish a notation for calculations to be performed in the next section. All of the stated relations can be found in textbooks on elasticity, such as Bisplinghoff et al. (2002); Atanackovic and Guran (2000); Landau and Lifshitz (1986).

To determine the elastic deformation energy W_E of a body, the force $\vec{F}(\vec{r})$ and displacement $\vec{u}(\vec{r})$ of each point $\vec{r}$ of the body must be determined. It is convenient to express these quantities as two tensors σ_{ij} and γ_{ij}. The stress tensor σ_{ij} denotes the force component along Cartesian coordinate j per area A_i normal to Cartesian coordinate i:

$$\sigma_{ij} = \lim_{A_i \to 0} \frac{F_j}{A_i}. \tag{3.22}$$

The strain tensor γ_{ij}, expresses the change in displacement along coordinate j per unit distance along coordinate i:

$$\gamma_{ij} = \partial_i u_j. \tag{3.23}$$

The deformation energy for infinitesimal strain is

$$W_E = \frac{1}{2}\int\limits_{\mathrm{material}} \mathrm{d}^3\vec{r}\,\sigma_{ij}\gamma_{ij} = \frac{1}{2}\int\limits_{\mathrm{material}} \mathrm{d}^3\vec{r}\,E_{ijkl}\gamma_{ij}\gamma_{kl}. \tag{3.24}$$

The second integral (again) uses the premise of a linear system (infinitisemial strain), which has a linear relationship between stress and strain known as generalised Hooke's law:

$$\sigma_{ij} = E_{ijkl}\gamma_{kl}. \tag{3.25}$$

The fourth-order tensor of elasticity E_{ijkl} has 81 components, 21 of which are independent in the general case of an anisotropic material. For isotropic materials, the tensor of elasticity can be parametrised by only two material constants. Two different parametrisations are particularly common. Theoreticians often use the Lamé parameters λ and μ:

$$E_{ijkl} = \lambda\delta_{ij}\delta_{jk}\delta_{kl} + 2\mu\delta_{ik}\delta_{jl}. \tag{3.26}$$

Expressed using the modulus of elasticity E and Poisson's ratio σ, the tensor of elasticity is

$$E_{ijkl} = \frac{E\,\sigma}{(1+\sigma)\,(1-2\sigma)}\delta_{ij}\delta_{jk}\delta_{kl} + \frac{E}{1+\sigma}\delta_{ik}\delta_{jl}. \tag{3.27}$$

Calculation of Elastic Deformation Energy in the Substrate

Although Eq. (3.24) gives an expression for the deformation energy, it is still necessary to determine either the strain tensor $\gamma_{ij}(\vec{r})$ or the displacement vector $\vec{u}(\vec{r})$. If the applied pressure $p(\vec{r})$ (i.e., the optical mode) is applied on a small central area of the mirror, the substrate can be approximated as an infinite half-plane. A slightly more general problem (with a vectorial force profile $\vec{p}(\vec{r})$ applied) was already solved by Boussinesq in 1885, as Landau and Lifshitz (1986) point out in presenting their solution using a Green's function $\vec{G}(\vec{r})$. After simplification to the case of a normal pressure application, it is

$$\vec{u}(\vec{r}) = \int_{\text{ms}} \mathrm{d}^2\vec{r'}\,\vec{G}(\vec{r}-\vec{r'})\,p(\vec{r'}), \tag{3.28a}$$

$$\text{with}\quad \vec{G}(x,y,z) = \frac{1+\sigma}{2\pi E}\left\{\begin{array}{c} \frac{xz}{r^3} - x\frac{1-2\sigma}{r(r+z)} \\ \frac{yz}{r^3} - y\frac{1-2\sigma}{r(r+z)} \\ \frac{2(1-\sigma)}{r} + \frac{z^2}{r^3} \end{array}\right\}\quad\text{where}\quad r = \sqrt{x^2+y^2+z^2}. \tag{3.28b}$$

The mirror surface is the $z = 0$ plane. The deformation energy W_E from this generic solution could be calculated directly via Eq. (3.24). But it also equals the work done by the pressure $p(\vec{r}_{\text{ms}})$ in deflecting the surface a distance $-u_z(\vec{r}_{\text{ms}})$:

$$W_E = \frac{1}{2}\int_{\text{ms}} \mathrm{d}^2\vec{r}\,p(\vec{r})\int_{\text{ms}} \mathrm{d}^2\vec{r}_{\text{ms}}\,G_z(\vec{r}-\vec{r}_{\text{ms}})\,p(\vec{r}_{\text{ms}}). \tag{3.29}$$

As the location vectors $\vec{r}$ and $\vec{r}_{\text{ms}}$ stay on the mirror surface, their z-component is always zero. Thus the explicit form of Eq. (3.29) simplifies to

$$W_E = \frac{(1+\sigma)(1-\sigma)}{2\pi E}\iint_{\text{ms}} \mathrm{d}x\,\mathrm{d}y \iint_{\text{ms}} \mathrm{d}x'\,\mathrm{d}y'\,\frac{p(x',y')\,p(x+x',y+y')}{\sqrt{x^2+y^2}}. \tag{3.30}$$

This can be calculated analytically for the fundamental Gaussian optical mode of waist radius w_0 or rather the corresponding pressure profile $p(\vec{r}_{\mathrm{ms}})$:

$$I(\vec{r}_{\mathrm{ms}}) = I_0 \frac{2}{\pi w_0^2} e^{-2r_{\mathrm{ms}}^2/w_0^2}, \tag{3.31a}$$

$$p(\vec{r}_{\mathrm{ms}}) = \frac{F_0}{I_0} I(\vec{r}_{\mathrm{ms}}). \tag{3.31b}$$

Levin (1997) performed such a calculation for an infinite half-space as substrate, but his result differs from that of all later publications and is identified as erroneous in a footnote of Liu and Thorne (2000). In my numerical calculation of this value in Section 3.3.2, I discovered that by neglecting the deformation energy from shearing stresses ($\sigma_{ij}\gamma_{ij}$ terms with $i \neq j$), Levin's result is reproduced. Bondu et al. (1998) gives the correct result for the infinite half-space, where w_0 is the Gaussian waist radius as defined above:

$$\frac{W_E}{F_0^2} = \frac{1 - \sigma^2}{2\sqrt{\pi}Ew_0}. \tag{3.32}$$

Spacer and Joint Contribution

For arbitrary mechanical and optical geometries, the elastic dissipation energy W_E can be calculated numerically. For this kind of mechanical problem, the finite element method is well suited. It has been used by Numata et al. (2004a) to refine and validate analytical noise estimates he calculated for optical clock resonators.

With a simplifying assumption, the relevant contributions from the mirror-supporting structure can be estimated analytically: for a uniform axial compression across a slab of constant cross sectional area A, the energy dissipated along a length l is

$$\frac{W_E}{F_0^2} = \phi(\omega)\frac{l}{2\,A\,E}. \tag{3.33}$$

This gives the noise contribution of a cylindrical spacer or an upper bound for a spacer of non-uniform cross-section by substituting its minimum cross-section for A. As the length scale A/l is usually large compared to the length scale given by the beam radius w_0, spacers from the same material as the mirror substrate have negligible contribution to thermal noise (see Numata et al., 2004a, for numerical examples).

The joints between substrate and spacer require attention: as glues may have a dissipation factor $\phi_{\mathrm{glue}} \gtrsim 10^4\,\phi_{\mathrm{spacer}}$ for the common ULE spacers, even a single 10 µm thin layer of glue as hard (same E) as the spacer would contribute the same amount of thermal noise as a typical 10 cm long spacer of the same cross-sectional area. Consequently, optical contacting is the preferred method for joining mirror and spacer in clock resonators.

Additional Dissipation in the Coating

If the finite element method is used, arbitrary known inhomogeneities in the substrate can be modelled easily: regions can be assigned different elastic properties (E and σ)

and different loss factors $\phi(\vec{r};\omega)$ can be considered by rewriting Eq. (3.21) using Eq. (3.24) as

$$\mathrm{Re}[Y(\omega)] = \frac{\omega}{2\pi F_0^2} \int\limits_{\text{material}} \mathrm{d}^3\vec{r}\, \phi(\vec{r};\omega)\, \sigma_{ij}\gamma_{ij}. \tag{3.34}$$

This is a trivial integral, as the stress σ_{ij} and strain γ_{ij} tensors are available as results of the finite element method.

There is, however, a more convenient approach to the inhomogeneity presented by the dielectric coating on the mirror. As it is typically much thinner than the size scale w_0 on which the light intensity $I(\vec{r})$ varies,[2] the coating can be treated as 2-dimensional. Using the deformation of an infinite substrate Eq. (3.28a) and restricting the volume integral in Eq. (3.34) to a coating of thickness d, the elastic deformation energy of the coating becomes (Nakagawa et al., 2002)

$$W_E = d\, \frac{(1+\sigma)(1-2\sigma)}{E} \iint\limits_{\text{ms}} \mathrm{d}x\, \mathrm{d}y\, p^2(x,y) \tag{3.35}$$

in the limit of an infinitesimally thin coating. Such a two-dimensional, flat membrane has identical stresses on either side: the underlying substrate will be exposed to the same pressure profile as the mirror's surface. It is therefore sufficient to compute the bulk (substrate) contribution to the conductance for an uncoated substrate and the surface (coating) contribution can readily be determined by the above integral.

These arguments are strictly valid only if the modulus of elasticity E and the Poisson's ratio σ are identical for the substrate and for each of the coating layers. Such an assumption is not entirely unreasonable: the deformation energy is quite insensitive to the exact value of the Poisson ratio and both coatings and substrates are invariably made of hard, glass-like materials with roughly similar moduli of elasticity. Indeed, Numata et al. (2004a) use this assumption in their prediction of thermal noise contributions in clock resonators. If material data for the coating layers are available, a better estimate can be made (Crooks et al., 2002; Harry et al., 2002; Vyatchanin, 2004; Harry et al., 2006).

Total Noise Estimate

The energies $\phi(\omega)W_E$ that are dissipated in each part of the resonator can be added. From this sum, the mechanical conductance can be deduced via Eq. (3.21). For a resonator with two identical mirrors separated by a spacer, one finds

$$\mathrm{Re}[Y(\omega)] = \frac{\omega}{\pi F_0^2} \left(\phi_d(\omega)\, W_{E,d} + 2\, \phi_c(\omega)\, W_{E,c} + 2\, \phi_s(\omega)\, W_{E,s} \right). \tag{3.36}$$

Here the subscripts "d," "c" and "s" denote spacer (distance), coating and substrate, respectively.

---

[2]Typical coatings consist of up to 40 quarter-wave stacks. Due to the refractive index of the coating layers, this is considerably thinner than 10 μm at a wavelength of 1 μm. Typical $\text{TEM}_{0,0}$ waist radii range from 200 μm for clock resonators to several cm for gravitational wave detectors.

Eq. (3.36) can be used to calculate the displacement noise via Eq. (3.9). Substituting the contribution of the spacer from Eq. (3.33), that of the coating from Eq. (3.35) and that of the substrate from Eq. (3.30), the noise in cavity length L as sampled by an intensity profile $I(\vec{r})$ results as

$$S_L(\omega) = 4\frac{k_B T}{\pi\,\omega}\left\{\phi_d(\omega)\,\frac{l}{2\,A\,E_d} + 2\,\phi_c(\omega)\,d\,\frac{(1+\sigma_c)(1-2\sigma_c)}{E_c\,I_0^2}\int\limits_{\mathrm{ms}} I^2(\vec{r})\,\mathrm{d}^2\vec{r}\right.$$
$$\left. +2\,\phi_s(\omega)\frac{1-\sigma_s^2}{2\,\pi\,E_s\,I_0^2}\int\limits_{\mathrm{ms}}\int\limits_{\mathrm{ms}}\frac{I(\vec{r})\,I(\vec{r'})}{\|\vec{r}-\vec{r'}\|}\,\mathrm{d}^2\vec{r}\mathrm{d}^2\vec{r'}\right\}. \qquad (3.37)$$

The spacer's dimensions are its cross section A and length l, the coating's thickness is d, the integrals run over the entire surface of a mirror with incident beam intensity profile $I(\vec{r})$ and total incident power I_0. The coating term (first integral) implicitly assumes $E_c \approx E_d$ and $\sigma_c \approx \sigma_d$. Although I have indicated the integrals to run only over the mirror surface "ms," this expression is derived from the deformation Eq. (3.28) of an infinite-half space and as such only applicable if the substrate is large compared to the beam.

In the literature, S_L or parts of it are usually given for a $\mathrm{TEM}_{0,0}$ mode only (Levin, 1997; Bondu et al., 1998; Harry et al., 2002; Numata et al., 2004a) and this specialisation is invariably applied early in the derivation. Often the coating contribution is expressed as fractional correction to that of the substrate. Written as Eq. (3.37), the length noise in a resonator with a $\mathrm{TEM}_{0,0}$ mode of identical waist radius w on each of two resonator mirrors is (e.g. Numata et al., 2004a, with the factor $3\pi R^2$ in the denominator of the spacer term corrected and trivially generalised to $2A = 2\pi R^2$):

$$S_L(\omega) = 4\frac{k_B T}{\pi\,\omega}\left\{\phi_d\,\frac{l}{2\,A\,E_d} + 2\,\phi_c\,d\,\frac{(1+\sigma_c)(1-2\sigma_c)}{\pi\,E_c\,w_0^2} + \phi_s\frac{1-\sigma_s^2}{\sqrt{\pi}E_s\,w_0}\right\}. \qquad (3.38)$$

In comparing Eq. (3.38) to Numata's expressions, note that Numata considers a single mirror and writes the spectral density in units of m^2/Hz despite expressing it using only angular frequencies. For peculiarities of earlier publications, see the notes in Liu and Thorne (2000).

The different dependence of the spacer, coating and substrate terms in Eq. (3.38) on the waist radius w_0 is caused by their different dimensionality. As the entire force applied by a beam-mimicking pressure profile is evenly distributed across the spacer cross-section, the first (spacer) term does not depend on the beam size (or shape) at all. The next (coating) term strongly depends on the waist radius ($\propto w_0^{-2}$) because the dissipation in a thin layer scales inversely with the area over which a constant force is applied. For the final (substrate) term, dissipation in underlying layers of material must be considered also, where the stress profile spreads out to infinity, thus reducing the scaling with waist radius to $\propto w_0^{-1}$. The ensuing section will extend this analysis of size dependence to shape dependence.

3.2.4 Integral Method

The dependence of thermal noise on beam shape can be expressed as a scaling with spatial frequency $\vec{k}$ in the Fourier-transformed beam intensity

$$\tilde{I}(\vec{k}) = \frac{1}{2\pi} \int\limits_{\mathbb{R}^2} \mathrm{d}^2\vec{r}\, I(\vec{r})\, e^{-\imath\vec{k}\vec{r}} \tag{3.39}$$

by rewriting Eq. (3.28a) in terms of $\vec{k}$. Such an approach was first employed by O'Shaughnessy et al. (2004) for the similar case of substrate thermoelastic noise and has since been applied to other types of noise, see Lovelace (2007). The substrate Brownian motion term Eq. (3.29) takes the form

$$W_E = \frac{1}{2} \int\limits_{\mathbb{R}^2} \mathrm{d}^2\vec{k}\, \tilde{G}_z(\vec{k})\, \tilde{p}^2(\vec{k}) \tag{3.40}$$

for a Fourier transformed pressure profile $\tilde{p}(\vec{k}) = F_0\, \tilde{I}(\vec{k})/I_0$. This can be simplified to

$$W_E = \frac{(1+\sigma)(1-\sigma)}{E} \int\limits_{\mathbb{R}^2} \mathrm{d}^2\vec{k}\, \frac{1}{\|\vec{k}\|}\, \tilde{p}^2(\vec{k}), \tag{3.41}$$

as done by Vinet (2005) for a rotationally symmetric beam profile. The coating contribution Eq. (3.35), can be expressed accordingly (Vyatchanin, 2004; O'Shaughnessy, 2006):

$$W_E = d\, \frac{(1+\sigma)(1-2\sigma)}{E} \int\limits_{\mathbb{R}^2} \mathrm{d}^2\vec{k}\, \tilde{p}^2(\vec{k}). \tag{3.42}$$

Scaling Law

Eq. (3.41) and Eq. (3.42) can be generalised in the following scaling law for noise contributions as sampled by a beam profile $\tilde{I}(\vec{k})$ with total power I_0, see Lovelace (2007). As the length noise S_L is proportional to the mechanical admittance $\mathrm{Re}[Y]$, which in turn is proportional to the elastic deformation energy W_E, the scaling law can be given as

$$S_x \propto \frac{1}{I_0^2} \int\limits_{\mathbb{R}^2} \mathrm{d}^2\vec{k}\, \|k\|^{\gamma-1} \tilde{I}^2(\vec{k}). \tag{3.43}$$

Exponents γ for the noise sources for which this law is applicable are listed in Table 3.1.

In Eq. (3.31), I have already given results for the noise of the $\mathrm{TEM}_{0,0}$ mode with intensity distribution $I_{0,0}(\vec{r})$. This makes it convenient to express the noise power spectral density S_I seen by an arbitrary intensity profile $I(\vec{r})$ as a fraction of that seen by the $\mathrm{TEM}_{0,0}$ mode. Because of the different scaling, one such fraction is needed for each noise contribution. I use s_c and s_s for the coating and the substrate contribution, respectively

Type of Noise	Origin	Exponent γ
Brownian motion	Substrate	0
	Coating	1
Thermoelastic noise	Coating	1
(low frequency tail)	Substrate	2

Table 3.1: Exponents for noise scaling with spatial frequency.

(the spacer contribution is independent of the mode profile). For simplicity assuming that both intensity distributions $I(\vec{r})$ and $I_{0,0}(\vec{r})$ contain the same total power, these fractions are

$$s_c = \frac{\int\limits_{\mathbb{R}^2} \mathrm{d}^2\vec{k}\, \tilde{I}^2(\vec{k})}{\int\limits_{\mathbb{R}^2} \mathrm{d}^2\vec{k}\, \tilde{I}_{0,0}^2(\vec{k})}, \tag{3.44a}$$

$$s_s = \frac{\int\limits_{\mathbb{R}^2} \mathrm{d}^2\vec{k}\, \|k\|^{-1} \tilde{I}^2(\vec{k})}{\int\limits_{\mathbb{R}^2} \mathrm{d}^2\vec{k}\, \|k\|^{-1} \tilde{I}_{0,0}^2(\vec{k})}. \tag{3.44b}$$

Result

Eq. (3.41) and Eq. (3.42) allow to express the length noise Eq. (3.37) seen by an arbitrary mode profile in a resonator in a computationally easier way:

$$S_L(\omega) = 4\frac{k_B T}{\pi\,\omega}\left\{\phi_d(\omega)\,\frac{l}{2\,A\,E_d} + 2\,\phi_c(\omega)\,d\,\frac{(1+\sigma_c)(1-2\sigma_c)}{E_c I_0^2}\int\limits_{\mathbb{R}^2} \mathrm{d}^2\vec{k}\,\tilde{I}^2(\vec{k})\right.$$
$$\left. +2\,\phi_s(\omega)\frac{1-\sigma_s^2}{E_s I_0^2}\int\limits_{\mathbb{R}^2} \mathrm{d}^2\vec{k}\,\frac{1}{\|\vec{k}\|}\,\tilde{I}^2(\vec{k})\right\}. \tag{3.45}$$

If the integrals are calculated separately as the scale factors s_c and s_s from Eq. (3.44), then this result can be expressed as a modification of the TEM$_{0,0}$ result:

$$S_L(\omega) = 4\frac{k_B T}{\pi\,\omega}\left\{\phi_d\,\frac{l}{2\,A\,E_d} + 2\,s_c\,\phi_c\,d\,\frac{(1+\sigma_c)(1-2\sigma_c)}{\pi\,E_c\,w_0^2} + s_s\,\phi_s\,\frac{1-\sigma_s^2}{\sqrt{\pi}E_s\,w_0}\right\}. \tag{3.46}$$

3.3 Values of Brownian Motion Thermal Noise

3.3.1 Material Properties

Mechanical Losses of Mirror Substrates

I list a selection of measured Q factors for some materials of potential interest for optical clock resonators in Table 3.2. Early observations of low loss tangents $\tan\phi$ of mate-

Material	Q-Factor	T [K]	T_A [°C]	$\frac{\omega}{2\pi}$ [kHz]	Source
Zerodur	3 100			few–100	Numata et al. (2004a)
ULE	61 000			few–100	Numata et al. (2004a)
BK7	3 600				Numata et al. (2003)
Si	300 000	300		26	Tittonen et al. (1999)
Si	4 000 000	4		26	Tittonen et al. (1999)
Si	90 000 000	300		15	Nawrodt et al. (2008)
Si (100)	450 000 000	6		15	Nawrodt et al. (2008)
Herasil 1	720 000			30–100	Numata et al. (2004b)
Herasil 1	970 000		900	30–100	Numata et al. (2004b)
7980 5F	10 000 000			30–100	Numata et al. (2004b)
7980 5F	21 000 000		900	30–100	Numata et al. (2004b)
7980 5F	33 000 000		980	30–100	Numata et al. (2004b)
Suprasil 312	34 000 000			30–100	Numata et al. (2004b)
Suprasil 312	43 000 000		980	30–100	Numata et al. (2004b)
Suprasil 312	82 000 000			0.4	Ageev et al. (2004)
Suprasil 312	170 000 000		950	1.2; 2.8	Ageev et al. (2004)
Suprasil 312	203 000 000		950	0.4	Ageev et al. (2004)
Suprasil 312 SV	120 000 000			11.2	Willems and Bushy (2003)
Sapphire	200 000 000			14; 16	Willems and Bushy (2003)

Table 3.2: Mechanical Q-factors measured in bulk samples (selection). Zerodur and ULE are glass ceramics with low thermal expansion made by Schott and Corning, respectively. BK7 is a borosilicate glass made by Schott. The other brand names label fused silica glasses: Herasil 1 and Suprasil 312 is produced by Heraeus; 7980 by Corning. The experiments were performed at a temperature T and were in some cases preceded by a heat-treatment at a temperature of T_A.

rials suitable as mirror substrate indicated that their intrinsic losses were frequency-independent for acoustic and low frequencies, although it was known that the loss tangent must approach zero in the mathematical limit of zero frequency, see Saulson (1990). The constancy of the loss tangent appears to be a good approximation provided that the Q factor of the sample does not exceed 10^6.

On the other hand, fundamentally unavoidable intrinsic losses have a predicted $\phi \propto \omega$ dependence. One example is the thermoelastic loss mechanism postulated by Zener (1937): elastic compression and expansion causes essentially adiabatic heating and cooling. The adiabaticity is not perfect as heat conduction occurs, causing a loss tangent that scales with the inverse characteristic distance between expansion and compression regions, $\omega/(\pi c)$, where c is the speed of sound. The other two intrinsic loss mechanisms that have since been identified as fundamental even in perfect crystals are phonon-phonon and phonon-electron interaction. These also lead to a $\phi \propto \omega$ dependence (Braginsky et al., 1986).

When samples reached Q factors on the order of 10^7, a frequency dependence of the loss tangent did become measurable (Numata et al., 2004b). But the observed levels still exceed the values expected (Braginsky et al., 1986) from the unavoidable intrinsic dissipation mechanism noted above by many orders of magnitude. A plausible mechanism is the relaxation of thermally excited internal degrees of freedom, such as conformational changes. The relaxation time $\tau^\star$ of such a process is described by Arrhenius' law (Zener, 1948; Braginsky et al., 1986):

$$\frac{1}{\tau^\star} = \frac{1}{\tau_0} \exp\left(-\frac{E_a}{k_B T}\right). \tag{3.47}$$

The process is parametrised by an activation energy E_a and a rate constant τ_0. From the relaxation time given in the above equation, a loss tangent can be calculated. For low loss materials, this is (Zener, 1948; Braginsky et al., 1986):

$$\phi(\omega) = \frac{E_\mathrm{i} - E}{\sqrt{E_\mathrm{i} E}} \frac{\omega \tau^\star}{1 + (\omega \tau^\star)^2}. \tag{3.48}$$

The first fraction is called the intensity of the relaxation, a further process parameter. In the context of Zener's theory of standard linear solids, E_i is an instantaneous modulus of elasticity which relaxes back to the steady-state value E with time constant $\tau^\star$. The Debye peak of maximum loss at $\omega\tau^\star = 1$ occurs at interdependent temperature and frequency. Measuring loss tangents at cryogenic temperatures allows identification of relaxation processes by determining the activation energy and its time constant τ_0, see Fine et al. (1954); Nowick and Berry (1972); Braginsky et al. (1986).

Penn et al. (2006) have evaluated measured Q factors to separate surface, thermoelastic and non-thermoelastic bulk loss angles. They predict a bulk Q factor of 2.5×10^9 at 100 Hz for the mirror substrates used in Advanced LIGO, with a frequency scaling of the loss angle $\phi \propto \omega^{0.77\pm0.02}$. This frequency scaling for low-loss silica is consistent with other findings: Numata et al. (2004b) finds exponents x for $\phi \propto \omega^x$ between 0.7 ± 0.1 and 1.0 ± 0.1 for different annealed silica samples with Q factors in excess of 10^7, a wider range for unannealed samples and $x \approx 0$ for unannealed samples with Q factors on the order of 10^6.

Whilst there is no experimental verification of such high Q factors as predicted by Penn et al., values exceeding 10^8 have been observed, as listed in Table 3.2. Such Q factors are comparable to those long known to be exhibited by sapphire. Amongst materials with zero thermal expansion coefficient at room temperature, ULE has the highest Q factor, but it is orders of magnitude below those available in other materials.

Mechanical Losses of Dielectric Coatings

The large loss tangent of the dielectric coatings of the mirrors in clock resonator can potentially be improved upon. Currently, quarter-wave stacks of SiO_2 (low index material) and Ta_2O_5 (high index material) are used, enabling optical losses to approach 1 ppm. A combination of low absorption, low scattering, good surface quality of the deposited

films and large refractive index contrast is necessary to achieve such performance. But Ta_2O_5 has been shown to significantly limit the Q factor of coatings, see measurements of the coating loss angle ϕ summarised in Table 3.3.

Materials		N	$d/\mu m$	$\phi_d \times 10^4$	Reference
SiO_2 /	Ta_2O_5	14	2.4	4.2(3)	Harry et al. (2002, commercial polish)
SiO_2 /	Ta_2O_5	38	24.36	1.0(3)	Harry et al. (2002, superpolish)
SiO_2 /	Ta_2O_5	40	5.4	3–10	Gröblacher et al. (2008, bare $50 \times 50\,\mu m^2$)
SiO_2 /	TiO_2	16	2.4	1.1	Böhm et al. (2006, bare $520 \times 120\,\mu m^2$)
— /	Ta_2O_5			3.8(2)	Crooks et al. (2006, from SiO_2/Ta_2O_5, LMA)
SiO_2 /	—			1.0(2)	Crooks et al. (2006, from SiO_2/Ta_2O_5, LMA)
Al_2O_3/	—			3.1(2)	Crooks et al. (2006, from Al_2O_3/Ta_2O_5, MLD)
Al_2O_3/	—			1.6(4)	Crooks et al. (2006, from Al_2O_3/Ta_2O_5, WP)
SiO_2 /	Ta_2O_5	30		2.6(7)	Harry et al. (2006, LMA)
SiO_2 /TiO_2:Ta_2O_5		30		1.8(2)	Harry et al. (2006, LMA, "low" doping)
SiO_2 /TiO_2:Ta_2O_5		30		1.6(2)	Harry et al. (2006, LMA, "high" doping)
SiO_2 /	—			0.5(3)	Harry et al. (2006, from SiO_2/Ta_2O_5, LMA)
— /	Ta_2O_5			4.4(2)	Harry et al. (2006, from SiO_2/Ta_2O_5, LMA)
SiO_2 /	Ta_2O_5	30	4.5	3.0(2)	Harry et al. (2007)
— /TiO_2:Ta_2O_5		1	4.73	3.5(4)	Harry et al. (2007, 6 % doping)
SiO_2 /TiO_2:Ta_2O_5		30	4.5	2.7(3)	Harry et al. (2007, 8 % doping)
SiO_2 /TiO_2:Ta_2O_5		30	4.5	1.7(1)	Harry et al. (2007, 23 % doping)

Table 3.3: Mechanical loss angles ϕ_d for highly reflective dielectric layers. TiO_2:Ta_2O_5 refers to titania doped tantalum oxide. N denotes the number of layers and d the total thickness. Coatings were manufactured at LMA/Virgo Lyon, MLD Technologies and Wave Precision (WP). Bare coatings refer to free-standing coatings obtained by removal of the mirror substrate.

Despite the low index contrast, disadvantageous for constructing highly reflective mirrors, the combination of SiO_2 and Al_2O_3 has been investigated because of otherwise promising properties, yet not found to be advantageous (Crooks et al., 2006). The combination of SiO_2 and TiO_2 does offer high index contrast and lower mechanical loss tangent. A free-standing quarter-wave stack made from this combination has been used as intentionally moderately high-reflective mirror and its Q factor was measured (Böhm et al., 2006). The loss tangent is about three times lower than that observed in traditional SiO_2/Ta_2O_5 quarter-wave stacks and might be lower yet, as the authors made no attempt at separating the observed loss tangent into the intrinsic loss of the quarter-wave stack and attachment-related "clamping losses," which were cited as responsible for a strong reduction in the Q factor of higher acoustic modes. The dissipation in quarter-wave stacks with a mixture of Ta_2O_5 and a TiO_2 "doping" (up to about 50 %) as high-index material has been measured by Crooks et al. (2006); Harry et al. (2006). The later source's claim that the optical absorption in these coatings is about 1 ppm suggests that these are suitable for mirrors in optical clock resonators, but the demonstrated

gain is slightly more modest than for pure TiO_2 as high index material.

3.3.2 Calculation of Beam Shape Effect

Modes

In optical resonators, spherical mirrors are usually used and the beam can be treated paraxially, as done by Kogelnik and Li (1966). The resulting intensity pattern is the same everywhere along the beam, except for a varying overall diameter that can be parametrised by the waist radius w of the fundamental mode. In the absence of astigmatism, there is a cylindrical symmetry and the supported modes are called Gauss-Laguerre modes. With mode indices p and l, the Laguerre polynomial $L_p^l(x)$ and in cylindrical coordinates, the intensity distribution of a Gauss-Laguerre mode is

$$I_{\text{Gauss-Laguerre}}(r,\theta) = \left(2\frac{r^2}{w^2}\right)^l \left(L_p^l\left(2\frac{r^2}{w^2}\right)\right)^2 \exp\left(-2\frac{r^2}{w^2}\right). \tag{3.49}$$

In practice the cylindrical symmetry is broken: reference resonators tend to have astigmatism, presumably arising from slight cylindrical shape deviations of nominally spherical resonator mirrors. In Cartesian coordinates aligned with the principal axes of the resonator, the resulting Gauss-Hermite modes $\text{TEM}_{m,n}$ have an intensity distribution

$$I_{\text{Gauss-Hermite}}(x,y) = \left(H_m\left(\sqrt{2}\frac{x}{w}\right) H_n\left(\sqrt{2}\frac{y}{w}\right)\right)^2 \exp\left(-2\frac{r^2}{w^2}\right), \tag{3.50}$$

where $H_m(x)$ is a Hermite polynomial.

Integral Method

I have calculated the relative thermal noise content in $\text{TEM}_{m,n}$ beams using the integral method Eq. (3.44) reviewed by Lovelace (2007). Using Eq. (3.44), the ratio between the thermal noise spectral density of an arbitrary intensity pattern $I(\vec{k})$ and that of a $\text{TEM}_{0,0}$ beam, $I_{0,0}$, of same waist radius w is

$$s_\gamma = \frac{\int_{\mathbb{R}^2} \mathrm{d}^2\vec{k}\,\|k\|^{\gamma-1}\tilde{I}^2(\vec{k})}{\int_{\mathbb{R}^2} \mathrm{d}^2\vec{k}\,\|k\|^{\gamma-1}\tilde{I}_{0,0}^2(\vec{k})} \frac{\left(\int_{\mathbb{R}^2} \mathrm{d}^2\vec{k}\,\tilde{I}_{0,0}(\vec{k})\right)^2}{\left(\int_{\mathbb{R}^2} \mathrm{d}^2\vec{k}\,\tilde{I}(\vec{k})\right)^2}. \tag{3.51}$$

The second fraction in Eq. (3.51) is a normalisation factor for beam intensity. It becomes unity if beams of equal total power are compared. The noise exponent γ was given in Table 3.1 on page 63. I present the results from Eq. (3.51) in Table 3.4 and in Figure 3.3.

Beyond comparing noise in modes of the same resonator (sharing the same Gaussian waist radius w), it may be of interest to realize the impact of changing the waist radius,

Mode	s_0	s_1	s_2
TEM$_{0,0}$	1	1	1
TEM$_{1,1}$	0.6226	0.5625	0.7905
TEM$_{2,2}$	0.4880	0.4104	0.6880
TEM$_{3,3}$	0.4143	0.3297	0.6232
TEM$_{4,4}$	0.3662	0.2787	0.5770
TEM$_{5,5}$	0.3317	0.2430	0.5416
TEM$_{6,6}$	0.3054	0.2165	0.5132
TEM$_{7,7}$	0.2845	0.1959	0.4898
TEM$_{8,8}$	0.2674	0.1793	0.4700
TEM$_{9,9}$	0.2530	0.1657	0.4528
TEM$_{10,10}$	0.2407	0.1542	0.4378
TEM$_{15,15}$	0.1983	0.1163	0.3830
TEM$_{20,20}$	0.1725	0.0946	0.3471
TEM$_{25,25}$	0.1547	0.0804	0.3211
TEM$_{30,30}$	0.1415	0.0703	0.30
TEM$_{40,40}$	0.122	0.0567	
TEM$_{50,50}$	0.11	0.0579	

Mode	s_0	s_1	s_2
TEM$_{1,0}$	0.7813	0.7500	0.9063
TEM$_{2,0}$	0.6830	0.6406	0.8656
TEM$_{3,0}$	0.6222	0.5742	0.8411
TEM$_{4,0}$	0.5792	0.5279	0.8240
TEM$_{5,0}$	0.5464	0.4930	0.8112
TEM$_{6,0}$	0.5202	0.4653	0.8011
TEM$_{7,0}$	0.4985	0.4426	0.7928
TEM$_{8,0}$	0.4800	0.4235	0.7859
TEM$_{9,0}$	0.4641	0.4070	0.7799
TEM$_{10,0}$	0.4502	0.3927	0.7747
TEM$_{15,0}$	0.3990	0.3410	0.7561
TEM$_{18,0}$	0.3774	0.3196	0.7483
TEM$_{20,0}$	0.3654	0.3076	0.7441

Mode	s_0	s_1	s_2
TEM$_{4,2}$	0.4212	0.3382	0.6344
TEM$_{4,3}$	0.3892	0.3031	0.6004

Table 3.4: Noise scaling factors for Gauss-Hermite TEM$_{m,n}$ modes on an infinite substrate. The scaling factor for a noise source with noise exponent γ, calculated using the integral method Eq. (3.51), is given in the column s_γ. For Brownian motion noise, the substrate scaling factor is $s_s = s_0$ and the coating scaling factor is $s_c = s_1$.

as this allows comparing modes with individually optimised waist radii. If a beam's waist radius is scaled by a factor x, its intensity distribution changes as $\tilde{I}(\vec{k}) \to I(x\vec{k})$. From Eq. (3.51), scaling the beam waist radius by a factor of x results in a noise scaling of

$$s_\gamma = x^{-1-\gamma}. \tag{3.52}$$

Direct Method

I have further calculated noise scaling factors for Gauss-Hermite TEM$_{m,n}$ modes on finite substrates with Levin's direct approach introduced in Section 3.2.3 on page 56. The scaling factor s_s for substrate Brownian motion noise is then given by the ratio of elastic deformation energy of the TEM$_{m,n}$ mode on a finite substrate to the deformation energy of a TEM$_{0,0}$ mode on an infinite substrate. Because of the rectangular nature of Gauss-Hermite modes, I chose a box as shape for the finite substrate. Its surface is rectangular with edge length $2a$; the depth is a. I performed the calculations using the commercial finite element program COMSOL. The substrate sizes that could be readily modelled are, in relation to the mode size, far smaller than those used in optical clocks. I constrain all except for the mirrored surface of the substrate to be immovable. This is equivalent to assuming the limit of an infinite modulus of elasticity for the surrounding
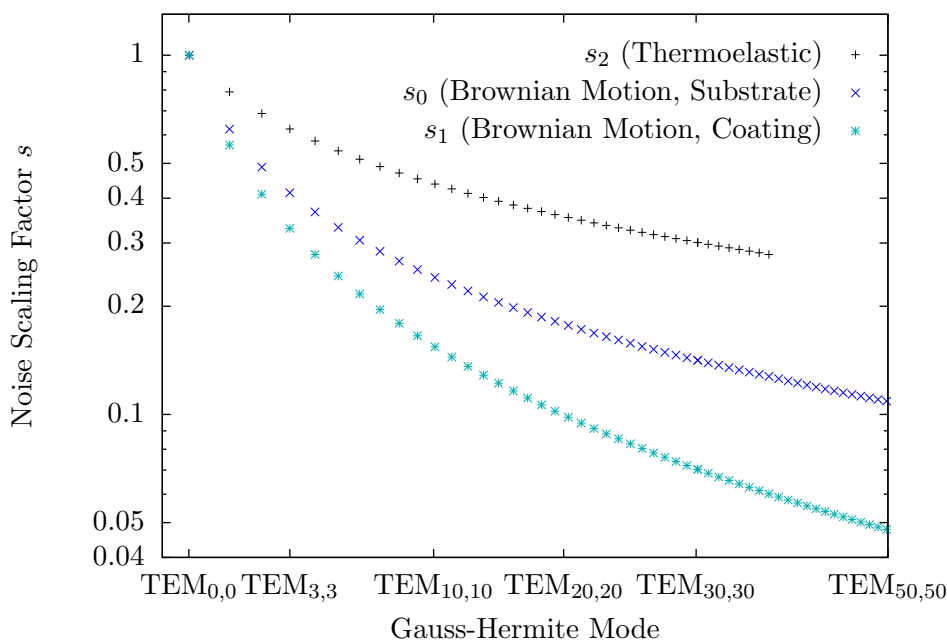
Figure 3.3: Noise scaling factors for Gauss-Hermite $\text{TEM}_{m,n}$ modes on an infinite substrate. The noise scaling factors s_0, s_1 and s_2 of Table 3.4 are plotted, with Gauss-Hermite modes spaced according to the edge size of a rectangular substrate for 1 ppm clipping loss.

media, which then does not move and does not contribute to Brownian motion noise. The results for various substrate sizes are given in Table 3.5.

Discussion

As could be expected intuitively, I find that the thermal noise in the frequency of a resonator's mode is reduced for Gauss-Hermite modes $\text{TEM}_{m,n}$ compared to the fundamental $\text{TEM}_{0,0}$ mode. Existing high-finesse resonators used in clock lasers may support rather high order modes, as for example the aperture required by a $\text{TEM}_{30,30}$ mode to limit diffraction losses to 1 ppm is only 2.6 times larger than that needed for the $\text{TEM}_{0,0}$ mode on a rectangular aperture. The coated areas on mirrors are usually much larger than this.

For a $\text{TEM}_{30,30}$ mode, the power spectral density of substrate Brownian noise is reduced to 14 % compared to the $\text{TEM}_{0,0}$ mode on an infinite substrate. The finite size of real resonator mirrors is unimportant for clock applications, as even an unrealistically tiny substrate of 40 waist radii edge length would still lead to 11 % of the $\text{TEM}_{0,0}$ noise level. Comparing Gauss-Hermite modes with individually chosen waist radii such that all have 1 ppm diffraction loss on the same aperture, I find only a modest improvement in substrate Brownian noise spectral density, to 55 % of the $\text{TEM}_{0,0}$ value for the $\text{TEM}_{3,3}$

Mode	a_{ppm}/w	s_0 for a_{ppm}	s_0 for $a = 20w$	s_0, $a \to \infty$	$\frac{a_{\mathrm{ppm}}}{2.51w}s_0$
$\mathrm{TEM}_{0,0}$	2.51	0.77	0.96	1	1
$\mathrm{TEM}_{1,1}$	2.83	0.42	0.59	0.6226	0.70
$\mathrm{TEM}_{2,2}$	3.09	0.30	0.45	0.4880	0.60
$\mathrm{TEM}_{3,3}$	3.31	0.24	0.38	0.4143	0.55
$\mathrm{TEM}_{4,4}$	3.51	0.20	0.33	0.3662	0.52
$\mathrm{TEM}_{5,5}$	3.69	0.18	0.29	0.3317	0.49
$\mathrm{TEM}_{7,7}$	4.03	0.14	0.24	0.2845	0.45
$\mathrm{TEM}_{10,10}$	4.46	0.11	0.20	0.2407	0.43
$\mathrm{TEM}_{20,20}$	5.62	0.06	0.14	0.1725	0.38
$\mathrm{TEM}_{30,30}$	6.54	0.05	0.11	0.1415	0.37
$\mathrm{TEM}_{40,40}$	7.33	0.04	0.09	0.122	0.36
$\mathrm{TEM}_{50,50}$	8.04	0.03	0.09	0.11	0.35

Table 3.5: Noise scaling factors for Gauss-Hermite $\mathrm{TEM}_{m,n}$ modes for different substrate sizes. The second column shows the required size for a $2a_{\mathrm{ppm}} \times 2a_{\mathrm{ppm}}$ rectangular aperture to limit diffraction losses to 1 ppm. The next three columns list the substrate noise scaling $s_0 = s_s$ for different substrate sizes $2a \times 2a \times a$. The first two of these come from finite element calculations of deformation energy using the direct method; the third one is taken from the results of the integral method of Table 3.4 for an infinitely large substrate. The final column lists the noise ratio between the $\mathrm{TEM}_{m,n}$ mode and a scaled fundamental Gaussian mode (with different waist radius), both on infinite substrates but with beam radii chosen such that both would have 1 ppm clipping loss on the same quadratic aperture.

and to 37 % for the $\mathrm{TEM}_{30,30}$ mode.

The improvement for the coating noise (both Brownian and thermoelastic) is better, to $s_c = 7.0$ % of the $\mathrm{TEM}_{0,0}$ value for the $\mathrm{TEM}_{30,30}$ if both have the same waist radius. Scaled for 1 ppm loss on the same rectangular aperture, the coating noise reduction factor becomes $s_c \left(\frac{6.54}{2.51}\right)^2 = 47$ %.

Thermoelastic substrate noise is reduced only slightly by using Gauss-Hermite modes instead of the fundamental Gaussian mode, with the $\mathrm{TEM}_{30,30}$ having about 30 % of the thermoelastic substrate noise of the $\mathrm{TEM}_{0,0}$. Scaled for 1 ppm loss on the same rectangular aperture, this noise contribution actually increases, by a factor of $s_2 \left(\frac{6.54}{2.51}\right)^3 \approx$ 5 for a $\mathrm{TEM}_{30,30}$ mode compared to the $\mathrm{TEM}_{0,0}$.

3.3.3 The Magnitude of Brownian Motion Noise

I make the same assumptions about material data as were made in the thermal noise prediction of Numata et al. (2004b): both coating and substrate has an elastic modulus of $E = 67.6$ GPa, a Poisson's ratio of $\sigma = 0.18$ and the loss angles correspond to Q factors of $6 \cdot 10^4$ for the ULE substrate and $2.5 \cdot 10^3$ for the coating.

Allan Variance

The power spectral density of relative frequency fluctuations, $S_{\Delta\nu/\nu}(\omega) = (2L)^{-2}S_L(\omega)$, can be used to measure frequency noise. But a more usual measure is the Allan variance $\sigma_y^2(t)$ (Allan, 1966; Allan et al., 1997). In our case, power spectral density and Allan variance are related by

$$\sigma_y^2(\tau) = 2 \int\limits_0^{\omega_{\max}} \mathrm{d}\omega \, \frac{S_L(\omega)}{(2L)^2} \frac{\sin^4 \frac{\omega\tau}{2}}{\left(\frac{\omega\tau}{2}\right)^2}, \tag{3.53}$$

where $2L$ is the round-trip length of the resonator. The frequency $\omega_{\max}$ describes a high-frequency cut-off of the measuring system. This cut-off is unimportant for optical clocks in practice: at relevant time scales of $\tau \gtrsim 1\,\mathrm{s}$, the Allan variance converges to within 3×10^{-3} even at the extremely low cut-off frequency $\omega_{\max} = 2\pi \times 3\,\mathrm{Hz}$. In the limit $\omega_{\max} \to \infty$, the Allan variance resulting from thermal noise with constant loss tangent ($S_L \propto \omega^{-1}$) is constant in τ: (Numata et al., 2004a)

$$\sigma_y^2(\tau) = 4\pi \,(\ln 2)\, S_{\Delta\nu/\nu} \left(\frac{2\pi}{\tau}\right). \tag{3.54}$$

Experimentally, Brownian motion noise is routinely seen in clock laser comparisons for times between 1 s and 100 s. For example, the instability of the NIST clock laser reported by Young et al. (1999), corresponding to an Allan deviation of ca. 4×10^{-16}, is largely accounted for by thermal noise, which corresponds to an Allan deviation of ca. 3×10^{-16}. (Numata et al., 2004a) Other examples are Sherstov et al. (2010); Alnis et al. (2008); Nazarova (2007). Allan variances, like power spectral densities, are additive for uncorrelated noise sources. Different noise contributions such as those from two lasers being compared or those from different mirrors in a single laser or one mirror's coating and substrate, can thus be calculated separately and added afterwards.

State-of-the-Art Clock Lasers: Brownian Motion Noise Levels

I consider two resonator geometries. Geometry A is the NIST laser (Young et al., 1999) treated by Numata et al. (2004a). The latter reference gives its spacer length as $L = 24\,\mathrm{cm}$ and its on-mirror waist radius as $w = 240\,\mathrm{\mu m}$. Geometry B is used in groups at PTB, NPL and MPQ (Alnis et al., 2008; Sherstov et al., 2010). Here the spacer length is $L = 7.75\,\mathrm{cm}$ (MPQ data; others are similar) and the on-mirror waist radius varies with wavelength. With one flat mirror and one concave mirror with a radius of curvature of $R = 500\,\mathrm{mm}$ and assuming a wavelength of $\lambda \approx 934\,\mathrm{nm}$, twice that of the octupole $^2\mathrm{S}_{1/2}(\mathrm{F} = 0) \to {}^2\mathrm{F}_{7/2}(\mathrm{F} = 3)$ clock transition in $^{171}\mathrm{Yb}^+$, the on-mirror waist radii follow (Kogelnik and Li, 1966) as $232\,\mathrm{\mu m}$ and $252\,\mathrm{\mu m}$.

Calculation results for these geometries, using different Gauss-Hermite modes are given in Table 3.6. In obtaining these values, the spacer contribution was ignored because it has negligible effect: Numata et al. (2004a) found it to contribute only 1 % to the power spectral density S_L in the analytic approach of Eq. (3.38) and still only 3 % in a finite element calculation taking into account the actual geometry. The difference to that

assumed in the analytic expression is the varying cross section of the spacer, in particular at the transition between substrate and spacer, where substrate thickness and contact area matter.[3] My result, $\sqrt{S_L} = 59 \, \mathrm{am}/\sqrt{\mathrm{Hz}}$ without spacer contribution, matches the analytic result of Numata et al. (2004a) that includes the spacer contribution and closely approximates their finite element result of $\sqrt{S_L} = 60 \, \mathrm{am}/\sqrt{\mathrm{Hz}}$. Note, however, that for a $\mathrm{TEM}_{10,10}$ mode in this geometry, the spacer contribution as obtained by Numata et al. by finite element calculation for the $\mathrm{TEM}_{0,0}$ mode exceeds the coating contribution. For a $\mathrm{TEM}_{30,30}$ mode, it would add 20 % to the power spectral density S_L and 10 % to the Allan deviation.

The $\mathrm{TEM}_{0,0}$ Allan deviations of Table 3.6 tend to be about 30 % below those obtained by comparing two identical (or similar) clock lasers. For geometry A, the experimental Allan devation, given by Young et al. (1999) in graphical form, is approximately $4 \cdot 10^{-16}$ for gate times between 1 s and 300 s, as Numata et al. (2004a) point out, whilst the calculated value is $2.9 \cdot 10^{-16}$, as shown in Table 3.6. A similar discrepancy is seen for geometry B (Sherstov et al., 2010) and also for a different geometry with almost identical thermal noise level (Nazarova, 2007). But it is improbable that significant additional noise is present in the clock laser beams beyond that present in the resonator: locking of otherwise independent lasers to different longitudinal modes of a single cavity has been

---

[3]Numata et al. (2004a) also point out that the finite element calculation correctly treats noise correlations, whilst the analytic approach just assumes uncorrelated noise contributions from substrate and spacer.

	$S_{L,c}$ $[\mathrm{am}^2/\mathrm{Hz}]$	$S_{L,s}$ $[\mathrm{am}^2/\mathrm{Hz}]$	$\sqrt{S_L}$ $[\mathrm{am}/\sqrt{\mathrm{Hz}}]$	σ_y $[10^{-16}]$
A, $\mathrm{TEM}_{0,0}$	520	2940	59	2.9
A, $\mathrm{TEM}_{3,3}$	170	1220	37	1.8
A, $\mathrm{TEM}_{5,5}$	130	980	33	1.6
A, $\mathrm{TEM}_{10,10}$	80	710	28	1.4
A, $\mathrm{TEM}_{30,30}$	40	420	21	1.0
B, $\mathrm{TEM}_{0,0}$	510	2920	59	8.9
B, $\mathrm{TEM}_{3,3}$	170	1210	37	5.7
B, $\mathrm{TEM}_{5,5}$	120	970	33	5.0
B, $\mathrm{TEM}_{10,10}$	80	700	28	4.2
B, $\mathrm{TEM}_{30,30}$	40	410	21	3.2

Table 3.6: Noise in state-of-the-art reference resonators. The power spectral density of length fluctuations, S_L, is calculated using Eq. (3.38) where the spacer term is neglected and the coating and substrate terms are explicitly given as $S_{L,c}$ and $S_{L,s}$. The necessary parameters are mentioned in the text and in Table 3.4. Because of nearly identical waist radii, these values vary little between the two geometries A and B (see text). Due to the longer length of geometry A, the same length fluctuations translate into lower relative length or frequency fluctuations, given in terms of their Allan deviation σ_y (final column).

demonstrated at a noise level one order of magnitude better in Allan deviation than needed to explain this discrepancy (Salomon et al., 1988). Unless technical noise sources account for it, it must be assumed that material constants such as the loss angles are not sufficiently accurate to predict the noise level of ULE resonators to better than 30 %.

Effect of Gauss-Hermite Modes

As seen in Table 3.6, the effect of higher-order Gauss-Hermite modes becomes appreciable even for moderate mode indices. Using a $TEM_{3,3}$ instead of a $TEM_{0,0}$ reduces the noise spectral density S_L and hence also the Allan variance σ_y^2 by 60 %. A $TEM_{10,10}$ more than halves the Allan deviation σ_y and a $TEM_{30,30}$ reduces it by a factor of 2.8.

For pure noise reduction, these factors should be compared to other options. Elongating the resonator by a factor of three achieves a better noise improvement in a ULE resonator as using a $TEM_{30,30}$ mode instead of a $TEM_{0,0}$ mode because the on-mirror waist radii increase also (without this effect, the improvement would be approximately equal). Another option with similar potential gains is a moderate increase in the radius of curvature of the resonator's mirrors, further increasing the $TEM_{0,0}$ mode radius. Finding ways of replacing the mirror substrate with one of the lower-loss materials of Table 3.2 on page 64 promises much larger improvements.

However, it could be argued that the use of higher-order modes has other scientific advantages. Because spacer, coating and substrate contribution scale differently, measuring the thermal noise level might allow to experimentally determine these values individually. This may be helpful, as there is still some discrepancy in published loss angle measurements, see e.g. Table 3.3 on page 66. Further, the loss angle of the glass ceramic ULE used in reference resonators for optical clocks has not been investigated as extensively as was done for materials of interest to the gravitational wave detector community, see Table 3.2. In the same manner, issues that are not yet understood theoretically, such as the question if additional noise originates in the optical contact between substrate and spacer, could be investigated.

Experimental Investigations on Thermal Noise

It is not difficult to measure thermal noise directly. In fact, as many clock laser setups achieve performance at the thermal noise level, measuring their instability constitutes a measurement of the thermal noise in their reference resonators. Particularly convincing results can be achieved by measuring the noise from a resonator built to have increased thermal noise, either by comparing the resonance frequencies of two such resonators or a single one to the more stable frequency of a resonator optimised for low thermal noise. Brownian motion thermal noise in terms of absolute length fluctuations is increased by decreasing the beam spot size on a mirror. In terms of frequency fluctuations, thermal noise can also be increased by decreasing the cavity length. This also helps to create small waist radii. The thermal noise interferometer built at Caltech for direct optical noise measurements such as that of coating Brownian motion by Black et al. (2004), has beam spot sizes similar to those used in optical clock resonators and hence similar total

levels of length fluctuations.

Thermal Noise Measurements in Rigid Cavities

The choice of mirror suspension divides the measurement of thermal noise into two classes. Either one builds a rigid cavity in the style of a state-of-the-art stabilisation resonator for clock lasers, as shown in Figure 3.1 on page 48. Then this setup is suitable for very low frequency measurements if sufficiently vibrationally isolated. This approach was used by Notcutt et al. (2006) to measure the noise in the $\text{TEM}_{0,0}$ mode of several resonator configurations by comparison to a more stable resonator. To increase thermal noise, he chose short Zerodur spacers for the noise resonators and, in some cases, for their mirrors. Notcutt also recorded an Allan variation for the $\text{TEM}_{2,4}$ mode in one of these resonators. In his measurement, an improvement in Allan variation is visible for times above 1 s where a significant increase of Allan variation with time, as if by drift, is evident.

Thermal Noise Measurements in Suspended Cavities

A wire suspension of resonator mirrors complicates noise measurements at low frequencies, where the suspension transfers vibrations. But for high frequencies, such a setup provides additional isolation, enabling optical noise measurements in the frequency range of interest to gravitational wave detectors.

In a milestone experiment of this type, Numata (2002); Numata et al. (2003) have measured fluctuations in the length difference of two 10 mm cavities from about 5 Hz to 100 kHz. By choosing appropriate mirror substrates—fused silica for coating Brownian noise, BK7 for substrate Brownian noise and CaF_2 for substrate thermoelastic noise—they were able to demonstrate good agreement with theory for three noise sources spanning from a few 100 Hz to 100 kHz. Numata assumed frequency-independent loss factors for the theoretical noise values that his experiment reproduced.

Comparison with Theory

By combining results from a VIRGO laser (Bondu et al., 1996) and a NIST clock laser (Young et al., 1999) experiments, Numata et al. (2004a) extended the frequency range over which thermal noise theory was confirmed experimentally to almost span from 10^{-3} Hz to 10^4 Hz. They find good agreement between the theory and data from the clock laser and reasonable agreement for the data from the VIRGO laser in the sense that the measurement repeatedly reaches and follows the predicted noise level but peaks consdierably higher at several frequencies.

Prospects of Using Modes Other Than the Gaussian $\text{TEM}_{0,0}$

Because of the potential reduction in thermal noise level, using other modes than the Gaussian $\text{TEM}_{0,0}$ has raised considerable interest in the gravitational wave detector community. Two different approaches are being considered: the use of Gauss-Laguerre

modes using spherical mirrors and the use of engineered mirror shapes to generate an optimal mode shape.

The use of Gauss-Laguerre modes has been proposed by Mours et al. (2006), who calculated a noise improvement over the $TEM_{0,0}$ mode on an infinite substrate when both are scaled for a 1 ppm loss on the same circular aperture. Chelkowski et al. (2009) considers practical issues connected with the hypothetical use of a Gauss-Laguerre $TEM_{3,3}$ mode in a gravitational wave detector. He concludes that using such a mode offers less thermal noise and is less sensitive to misalignment than using an enlarged $TEM_{0,0}$ with the same clipping loss of 1 ppm on a circular aperture.

Prior to the interest in Gauss-Laguerre modes, the quest for an optimal mode shape had already started the development of the integral method I presented in Section 3.2.4 to investigate the influence of mode shape. Because a larger illuminated area implies averaging noise contributions, many researchers started with the intuition that a uniform intensity profile would be optimal. Mirror shapes ("Mexican hats") that support such a "flat-topped" or "mesa" mode were found (D'Ambrosio, 2003; D'Ambrosio et al., 2004) and tested experimentally (Tarallo et al., 2007). As the integral calculation method for thermal noise of an infinite substrate were developed (see Lovelace, 2007), it was realized that at least mathematically, only the coating Brownian motion noise is minimised by a flat beam profile. Substrate Brownian Motion noise can be further minimised by reducing intensity components with low spatial frequencies, as evident from the scaling law Eq. (3.43). This approach leads to a profile with reduced intensity in the centre and increased intensity at the edges.

3.4 Selective Excitation of Gauss-Hermite Modes

Higher-order modes of a resonator are less affected by thermal noise, but they are less readily generated than the fundamental Gaussian mode available from a fibre output or even directly from many lasers. The resonators used in optical frequency standards tend to have sufficient astigmatism to only support Gauss-Hermite modes. This astigmatism is not present by design but by small imperfections in the shape of the nominally spherical (non-astigmatic) mirrors.

Degeneracy Lifting

A resonator with rotational symmetry about the optical axis (possibly after unfolding of the optical path) has Gauss-Laguerre eigenmodes. For a two-mirror resonator such as used in optical clocks, this is only nominally the case. In practice, one observes Gauss-Hermite modes which require only Cartesian symmetry. Their existence in clock resonators hints at slight cylindrical deformations of the mirrors from the nominally spherical or flat shape.

The Gauss-Hermite modes $TEM_{m,n}$ with $m + n =$ const would be degenerate in a resonator with perfect cylindrical symmetry. In actual clock resonators, this degeneracy is lifted. Stoehr (2005) has observed frequency splittings in two resonators, finding 0.54 MHz in one and values between 0.8 and 1.5 MHz for the other, depending on the

value of $m + n$. At the Max-Planck-Institut für Quantenoptik in Garching, Janis Alnis and I have observed a frequency-splitting of only 22 kHz in a 486 nm cavity.

As it is desirable to generate a Pound-Drever-Hall error signal (Drever et al., 1983; Black, 2001) with a modulation frequency above 1 MHz for frequency-locking, using Gauss-Hermite TEM$_{mn}$ modes other than the fundamental TEM$_{00}$ requires good mode-matching to keep the error-signal free from contributions of neighbouring modes.

3.4.1 Spatial Light Modulation

Holography

Recreating a beam of light not only regarding its intensity pattern, but entirely, including the light's wavefront or phase pattern, is called holographic reconstruction. Hence creating arbitrary phase and amplitude patterns is a form of holography. The most straight-forward approach would be to simultaneously effect the desired spatial amplitude and phase modulation in a beam of light. This can be expressed as a complex modulation $M(\vec{r}_m)$ if the electric field is also considered complex. I use $\vec{r}_m$ for locations in the modulator's plane. The unmodulated field of amplitude $A(\vec{r}_m)$ and phase $\delta(\vec{r}_m)$ is

$$E_0(\vec{r}_m) = A(\vec{r}_m) \exp\left(-\imath\delta(\vec{r}_m) - \omega t\right). \tag{3.55}$$

The real, physical field can be obtained by taking the real component. After the modulation, the complex field is

$$E_M(\vec{r}_m) = M(\vec{r}_m) E_o(\vec{r}_m). \tag{3.56}$$

To generate fully arbitrary beams of light, both phase modulation $\arg\left(M(\vec{r}_m)\right)$ and amplitude modulation $|M(\vec{r}_m)|$ are necessary. To my knowledge, no practical realization of truly complex modulators exist. Instead, a single real quantity—phase, amplitude or some combination thereof—is modulated. Practical holograms achieve the desired output pattern with a single real modulation by relaxing the requirement for arbitrary modulation into a spatially slowly varying modulation $m(\vec{r}_m)$, corresponding to a limited maximum diffraction angle.

Holographic Reconstruction in the First Diffraction Order

Traditionally, a hologram is created by the interference between two beams crossing at an angle α, where one beam corresponds to the unmodulated "reference beam" with field $E_0(\vec{r}_m)$ and the other one to the "object beam" with field $E_m(\vec{r}_m) = E_0(\vec{r}_m)m(\vec{r}_m)$. The total modulation can be thought of as a diffraction into the first order of a grating with a modulation $P(x)$ periodic in 2π, creating the angular separation between the two beams, followed by the desired slowly-varying modulation $m(\vec{r}_m)$:

$$M(\vec{r}_m) = m\left(\vec{r}_m\right) P\left(\vec{k}_\alpha \vec{r}_m\right). \tag{3.57}$$

The grating's wave vector $\vec{k}_\alpha$ corresponds to a diffraction angle $\tan\alpha = k_\alpha/k_\lambda$, where $k_\lambda = 2\pi\lambda$ is the length of the wave vector of the incident light, assuming normal incidence.

In the far field, the modulated field $\tilde{E}_M(\tan\alpha)$ is a function of the propagation angle α instead of spatial coordinates:

$$\tilde{E}_M(\tan\alpha) = \int_{\mathbb{R}^2} \mathrm{d}\vec{r}_m \, \exp\left(-\imath\,\vec{r}_m\,\vec{k}_\lambda\tan\alpha\right)\, m\left(\vec{r}_m\right) P\left(\vec{k}_\alpha\vec{r}_m\right) E_0(\vec{r}_m). \qquad (3.58)$$

Because the desired modulation is slowly varying compared to P, it can be treated as locally constant for the purpose of finding a real modulation function. In that approximation, $\tilde{E}_M(\tan\alpha)$ is just the diffraction of the grating P, multiplied by $m = A_m\exp(-\imath\,\delta_m)$ to give the desired amplitude $A_m = |m|$ and phase $\delta_m = \arg m$. By Fourier transform, I find this alternative total modulation function with the same desired effect:

$$M'(\vec{r}_m) = |m(\vec{r}_m)|\, P\left(\vec{k}_\alpha\vec{r}_m + \arg m(\vec{r})\right). \qquad (3.59)$$

For a blazed grating $P(x) = \exp(\imath\,x)$, alternative and original total modulation are identical. In general, they differ in high-spatial-frequency components. These are irrelevant to the desired slowly-varying modulation.

Amplitude Holograms

Eq. (3.59) allows driving amplitude modulators by choosing a real-valued grating function P. The maximum diffraction efficiency is achieved using $P(x) = \sin x$. This is also the optimum result from traditional amplitude hologram production using a photographic recording of the interference pattern of reference and object beam. As at least half of the incident light is either absorbed in the modulator or remains in the zeroth order and the rest splits evenly into positive and negative first order, the diffraction efficiency of such a hologram is limited to 25 %.

Phase Holograms

With a slight modification, Eq. (3.59) also allows describing phase modulators. To this end, a phase grating $P = \exp\left(\vec{k}_\alpha\vec{r}_m + \arg m(\vec{r})\right)$ is used and the desired amplitude $|m(\vec{r}_m)|$ is obtained by scaling the phase modulation range by a suitable factor $g\left(|m(\vec{r}_m)|\right)$. The total phase modulation is

$$\arg M'(\vec{r}_m) = g\left(|m(\vec{r}_m)|\right)\left(\vec{k}_\alpha\vec{r}_m + \arg m(\vec{r})\right). \qquad (3.60)$$

The function $g(x)$ needs to be chosen to modulate the diffraction efficiency of the programmed phase pattern to produce the desired amplitude modulation $x = |m(\vec{r}_m)|$:

$$g^{-1}(x) = \int_{-\pi}^{+\pi} \mathrm{d}\alpha\exp\left(-\imath\alpha\right)\exp\left(\imath\alpha x\right). \qquad (3.61)$$

It is important that only this amplitude, but not additional phase modulation in the desired diffraction order is effected by g. This can be achieved by the usual choice for the span of $\arg m(\vec{r})$ in Eq. (3.60), i.e. $-\pi$ to $+\pi$. Then the scaling effected by g does not change the effective (averaged) phase but only the diffraction amplitude.

Phase holograms offer an increased diffraction efficiency compared to amplitude holograms: no light is absorbed in the modulator and all of it can be diffracted into the first order. Thus there is no principal limit to the diffraction efficiency apart from the desired spatial attenuation given by the desired field amplitude $|m(\vec{r}_m)|$.

Aliasing

As a pixel-based device, a spatial light modulator is prone to produce aliasing: spatial frequencies in the desired modulation pattern which exceed the maximum spatial frequency $(2b)^{-1}$ supported by the pixel pitch b get aliased into the supported range of frequencies. This is not a problem for the presented amplitude modulation scheme using a sine grating, as this does not include high-spatial-frequencies. But the phase modulation scheme Eq. (3.60) describes a phase ramp that periodically wraps back over 2π. This wrapping is a discontinuity that contains high-spatial-frequencies and can lead to a deviation between programmed and desired phase modulation. To avoid these, I determine the average of the phase modulation Eq. (3.60) over the area covered by a pixel and use this value instead of a value for the centre of the pixel. This constitutes a low-pass filtering with anti-aliasing effect.

3.4.2 Setup

Equipment

I have used a two-dimensional, high-resolution spatial light modulator based on liquid crystal technology, the model LC-R 1080 produced by HOLOEYE Photonics AG in Berlin. It is a reflective liquid crystal display without polarisers, essentially an array of 1920×1200 pixels with programmable birefringence. By choosing linear polarisation directions for incoming and outgoing beam (using a polarisation analyser), it can be used both as an amplitude or a "phase-mostly" modulator, meaning less than 10 % residual amplitude modulation. This device offers only about 1.2π phase modulation, limiting its diffraction efficiency. Not spanning a full wavelength of phase retardation is a severe disadvantage regarding wavefront correction and general versatility of operation. Experimentally, I have exclusively used the phase-mostly mode of operation shown in Figure 3.4.

Wavefront Correction

The wavefront reflected from the SLM is distorted, presumably due to non-planarity of its surface and variations in the thickness of each pixel's liquid crystal layer. If not corrected by including the opposite wavefront distortion in the modulation programmed
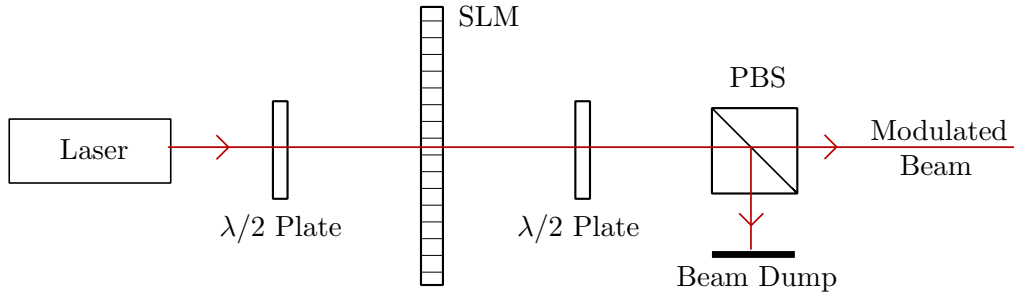
Figure 3.4: Phase modulation setup. The linear polarisation of a laser beam is rotated into the correct direction with a $\lambda/2$ waveplate before the spatial light modulator (SLM). The beam is then analysed using a polarising beam splitter (PBS). A further waveplate is used to tune the polarisation analyser. The actual setup includes beam expansion optics and the spatial light modulator used is reflective rather than transmissive.
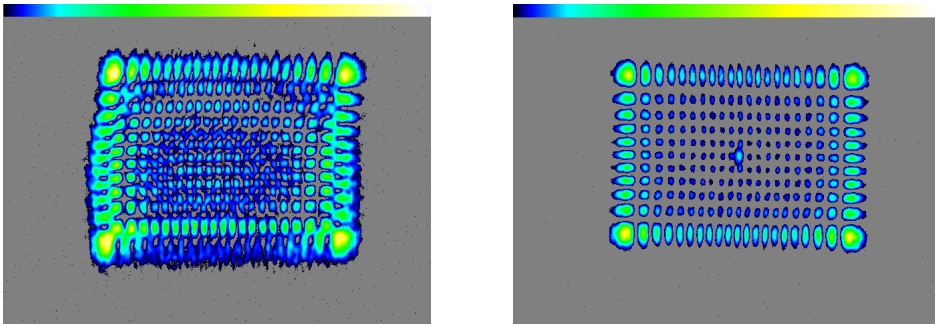

Figure 3.5: Generated Gauss-Hermite $TEM_{20,10}$ beams. Shown is the intensity as recorded by a camera for a beam generated without (left) and with (right) approximate wavefront correction. The false-colour intensity scale is given on top of each image. Grey corresponds to zero intensity, black to infinitesimal intensity and white to full scale intensity.

into the SLM, this causes severe distortion of generated beams, as illustrated for Gauss-Hermite beams in Figure 3.5.

I have measured the wavefront distortion interferometrically with the setup shown in Figure 3.6. By taking interferograms for different positions of the piezo-mounted mirror in one arm of the interferometer, the phase of the modulated beam can be estimated from the mirror position at which the intensity at the interferometer output assumes a minimum. Imaging the SLM plane onto the CCD camera used to observe the interferogram allows performing this for the entire SLM at once. The procedure is repeated for different programmed phase values, yielding the translation function between programmed and actually effected phase.

Following the approach by Matsumoto et al. (2008), I model the actual phase modu-
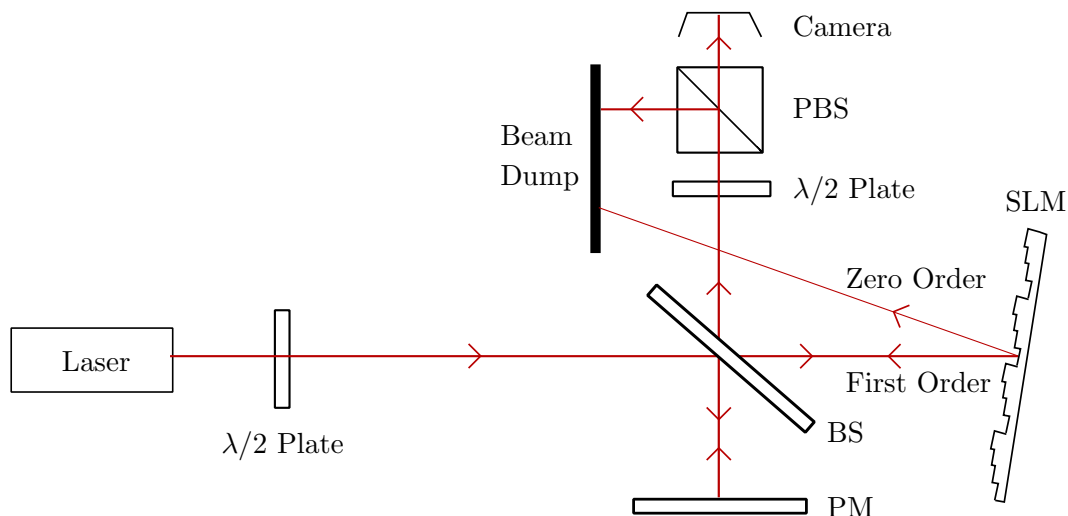
Figure 3.6: Wavefront interferometer setup. A Michelson interferometer is formed around a beamsplitter (BS). The spatial light modulator (SLM) is in one arm, where its first diffraction order is used. The other arm is formed by a piezo-actuated mirror (PM). The polariser-analyser setup of Figure 3.4 is used for the SLM to operate as phase-mostly modulator. The generated interferogram is digitised by a CCD camera. For clarity, I omit lenses used for beam expansion and imaging of the SLM plane onto the CCD plane.

lation ψ as a linear function of the programmed modulation value M:

$$\psi(M) = \psi_0 + aM \tag{3.62}$$

Figure 3.7 shows interferometrically measured phases and linear fits according to Eq. (3.62) for four different positions on the SLM. The total phase modulation achieved in my setup is approximately π, but differs across the modulator, requiring that values for phase offset ϕ_0 and modulation range a in Eq. (3.62) are measured for each location on the spatial light modulator. The result is shown in Figure 3.8. The phase variation across the modulator's surface corresponds to a wavefront distortion of more than two wavelengths, explaining the severe distortion seen without wavefront correction in Figure 3.5. Even the modulation range is not uniform which, if uncorrected, causes spatial deviations in the amplitude of generated beams.

Mode Analysation

I have coupled Gauss-Hermite modes generated by the SLM into a ring resonator to analyse the actually generated mode content. The setup is shown in Figure 3.9. I reused HR mirrors from a 486 nm ULE cavity as partially reflective coupling mirrors at 532 nm.
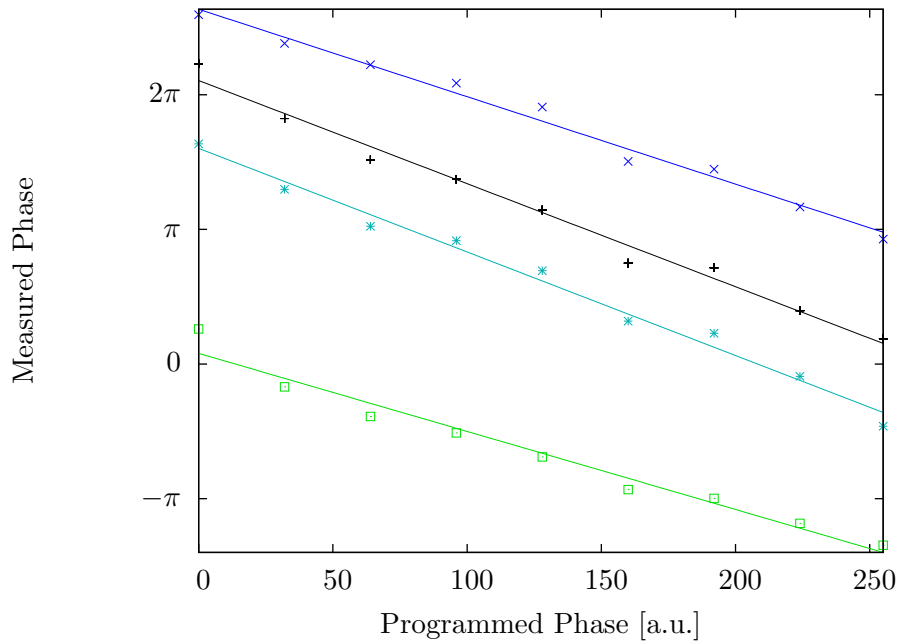
Figure 3.7: Phase modulation measurement. The interferometrically measured phase is plotted versus programmed modulation for four different locations on the SLM. Lines are linear fits according to Eq. (3.62).
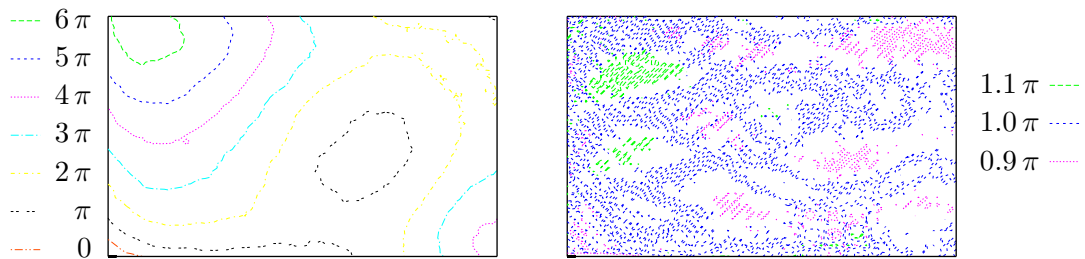
Figure 3.8: Phase modulation over SLM surface. The left graph shows the phase offset ϕ_0 and the right one the modulation range a over the entire camera image using the setup shown in Figure 3.6. Drawn are lines of constant phase, which are very jagged due to measurement noise.

At this wavelength, I measured a transmission of 110 ppm at normal incidence; as used in the resonator, the actual transmission may be larger because of the nonzero angle of incidence in the ring resonator. The transmission of the two highly reflective mirrors

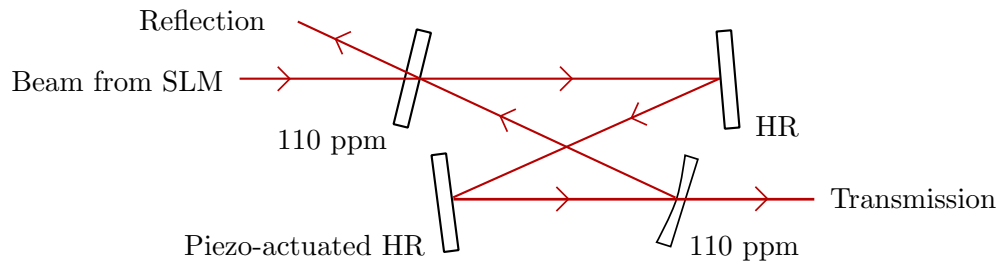Figure 3.9: Mode analyser setup. This ring resonator was used to analyse the fidelity of generated Gauss-Hermite modes. The single curved mirror has a radius of curvature of 500 mm. The free spectral range is approximately 500 MHz.

is orders of magnitude below that of the partially reflective mirrors. I recorded the transmission through the resonator as its length was scanned using the piezo-mounted mirror. This procedure carries the risk of slightly tilting the mirror and thus affecting the position of the resonator's modes.

3.4.3 Generation of Linear Gauss-Hermite Modes

Gauss-Hermite modes with nodes only along one axis ($TEM_{m,0}$ and $TEM_{0,n}$) could be generated with reasonably high fidelity. Figure 3.10 illustrates the fidelity for generated $TEM_{0,0}$ and $TEM_{18,0}$ modes. The $TEM_{18,0}$ excitation was manually optimised by adjusting the four degrees of freedom in the beam direction and waist location as well as five degrees of freedom in cylindrical focusing and cylindrical waist size, where a common orientation angle was used. All of these degrees of freedom are accessible by changing the beam-generating hologram. The four beam-steering degrees of freedom are further accessible by mirror adjustments. For crude adjustments including the entire mode-matching to the $TEM_{0,0}$ mode, I found mirror adjustment to be the faster and more convenient option. The adjustment of higher-order modes requires more angular resolution as spots with 180° optical phase difference become both more closely spaced and, more importantly, parts of the incident beam which are more distant from the beam axis must be matched. Thus adjustment by means of the mirror mounts can be difficult. The slower and more cumbersome alteration of the hologram can be helpful in this situation because small, test-wise applied changes can be precisely undone.

The generated beam's deviation from the resonator's $TEM_{18,0}$ mode is observed mostly as a $TEM_{17,1}$ resonator mode. This might be due to a remaining misadjustment in the adjusted degrees of freedom. It could also be due to a deviation between the generated mode shapes and the actual shape of the resonator's modes which would require additional degrees of freedom to correct.
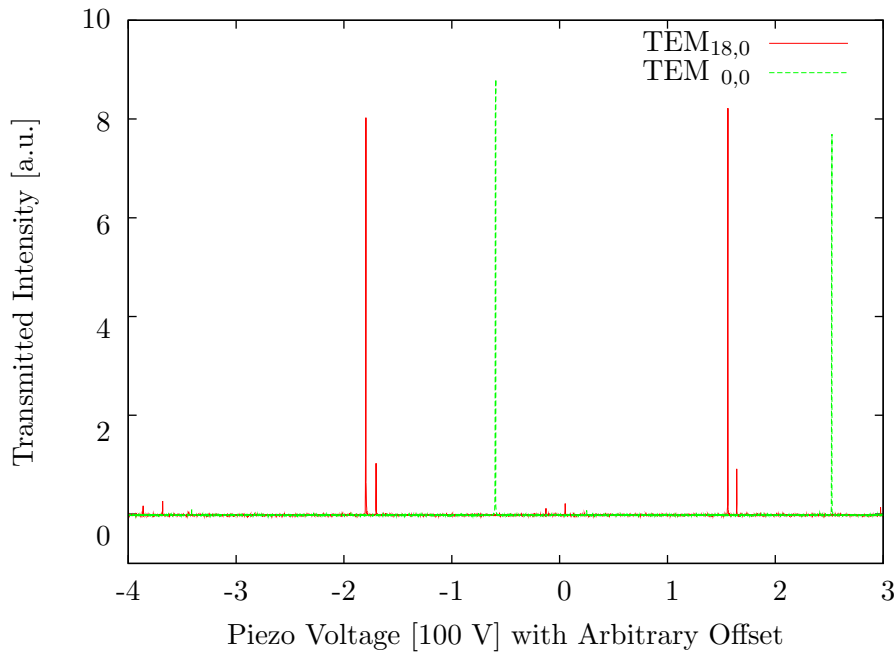
Figure 3.10: Mode content in generated linear Gauss-Hermite modes.

3.4.4 Generation of Rectangular Gauss-Hermite Modes

My attempts at generating Gauss-Hermite $TEM_{m,n}$ modes with $m > 0$ and $n > 0$ resulted in excitation of the desired as well as neighbouring $TEM_{m-1,n+1}$ or $TEM_{m+1,n-1}$ modes. Figure 3.11, a transmission scan for a generated $TEM_{4,3}$ mode, illustrates this effect. For the $TEM_{8,8}$, these neighbouring modes are excited as strongly as the actually desired mode.

The undesired mode content in the generated $TEM_{8,8}$ beam can be greatly reduced by generating an appropriately chosen superposition of modes with $m + n = 16$, such that the undesired mode content destructively interferes with the intentionally created correction. For the $TEM_{8,8}$ beam, this results in the improved generation fidelity shown in Figure 3.12.

Compared to the generation of uncorrected $TEM_{m,n}$ beams, there is an additional contribution to undesired mode content in my realization of the corrected $TEM_{8,8}$ beam: In anti-aliasing the programmed phase hologram by interpolating between phase values for adjacent pixels, phase discontinuities cause problems. The optical $180°$ phase flips in Gauss-Hermite are handled correctly by implementing these as changes in the sign of the amplitude at a fixed phase, but this treatment does not work for superpositions of modes with arbitrary phase. Hence numerical phase discontinuities arise, which are seen as thin grey lines in Figure 3.13, a visualisation of the phase hologram for the corrected $TEM_{8,8}$ generation. Since overall only small areas are affected, the effect of this irregularity is small. As the difference to the perfect desired hologram is localised in thin lines, the
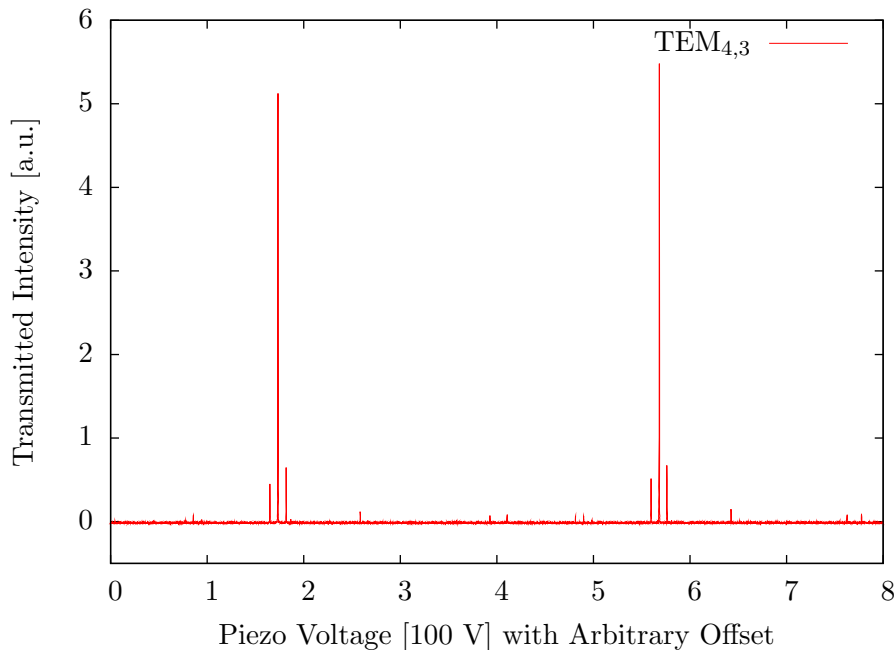
Figure 3.11: Mode content in the generated Gauss-Hermite mode $TEM_{4,3}$. The strongest peak corresponds to the resonator's $TEM_{4,3}$ mode, the neighbouring peaks to its $TEM_{3,4}$ and $TEM_{5,2}$ modes.

difference to the desired diffraction pattern (the corrected $TEM_{8,8}$ mode) will be spread out into large diffraction angles and blocked by an aperture around the generated mode, further reducing the impact of this antialiasing artefact.

The correction scheme can be extended to compensate arbitrary undesired $TEM_{m',n'}$ content. I express the complex amplitudes $p_{(m,n)}$ of the programmed $TEM_{m,n}$ modes in terms of complex amplitudes $r_{(m',n')}$ of actual resonator eigenmodes $TEM_{m',n'}$. By considering the tuples (m,n) and (m',n') as single indices, this is a simple matrix equation:

$$\vec{r} = \mathbf{M}\vec{p}. \tag{3.63}$$

Creating a desired mode combination (which can be a single mode) $\vec{r}$ requires knowledge of the inverse $\mathbf{M}^{-1}$:

$$\vec{p} = \mathbf{M}^{-1}\vec{r}. \tag{3.64}$$

The programmed modes are (nominally) an orthogonal basis system for arbitrary patterns of light, although it differs from the basis system formed by the resonator's modes. Even accounting for imperfections, it should remain a good basis system for expressing arbitrary light patterns. This leads me to expect that the matrix $\mathbf{M}$ is usually (or to very good numerical approximation) invertible. Thus indeed arbitrary undesired mode content can in principle be compensated.
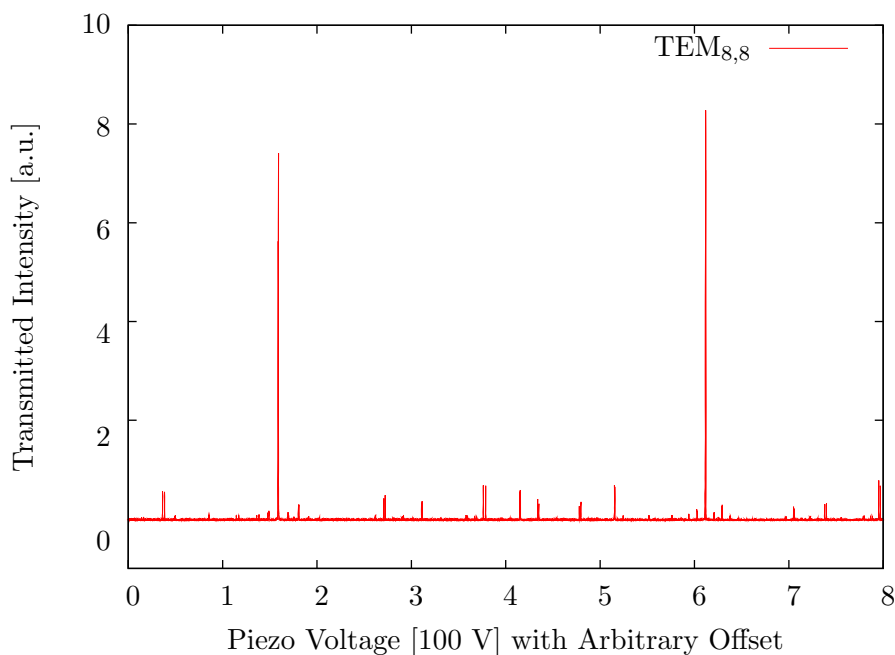
Figure 3.12: Mode content in a generated $\text{TEM}_{8,8}$ Gauss-Hermite mode.

In practice, only the amplitude but not the phase of the matrix elements $M_{(m',n'),(m,n)}$ can be extracted from a cavity transmission scan. The phases would have to be determined by test-wise superimposing $\text{TEM}_{m,n}$ modes with different phases, for hundreds of relevant modes. This ordeal is further complicated by the fact that these test-wise superpositions require a way of generating the $\text{TEM}_{m,n}$ with reasonable fidelity in the first place. For my setup, this requirement is only met for linear $\text{TEM}_{m,0}$ or $\text{TEM}_{0,n}$ and for moderately low order rectangular Gauss-Hermite modes ($m + n \lesssim 10$). The demonstrated improvement of a $\text{TEM}_{8,8}$ generation by trial-and-error superposition of modes with $m + n = 16$ constitutes a proof of principle for this scheme.

3.4.5 Results

I have demonstrated the selective generation of $\text{TEM}_{m,n}$ Gauss-Hermite modes using a liquid crystal spatial light modulator. The linear $\text{TEM}_{18,0}$ mode of a ring resonator could be generated with nearly 90 % fidelity by programming the spatial light modulator to produce the theoretical $\text{TEM}_{18,0}$ light pattern. Almost all of the error matched the resonator's $\text{TEM}_{17,1}$ mode.

Using the same approach for rectangular modes, the fidelity drops quickly with the mode sum $m + n$, with about 90 % fidelity demonstrated for the TEM_{43}. The error is mostly in the $\text{TEM}_{m+1,n-1}$ and $\text{TEM}_{m-1,n+1}$ modes. These modes can be suppressed by adapting the generated mode pattern. By generating a suitable superposition of some theoretical mode patterns, I demonstrated the generation of a TEM_{88} resonator mode

Figure 3.13: Phase hologram for $\text{TEM}_{8,8}$ generation. This hologram is corrected by the addition of several other nominal $\text{TEM}_{m,n}$ patterns with suitable amplitude and phase. Phase values are depicted as greyscale. The full scale (black to white) is the full actuator range of the spatial light modulator in the setup used. It corresponds to slightly less than π. A problem with the anti-aliasing algorithm, arising from numerical phase discontinuities, is evident in thin lines as seen e.g. in the spot in the top left corner.

with about ten times more intensity than the most strongly excited one of all other resonator modes, but the fidelity is only about 60 %. Possible limits to better mode adaption by this scheme are the temporal variation in generated light pattern as the light modulation is periodically refreshed in the device used and a possible shift in the resonator's optical axis as its resonances are scanned mechanically by a piezo-translator.

Bibliography

M. Abramowitz and I. A. Stegun (eds.). *Handbook of Mathematical Functions.* U.S. Department of Commerce, 10th edn. (1972).

A. Ageev, B. C. Palmer, A. D. Felice, S. D. Penn and P. R. Saulson. Very high quality factor measured in annealed fused silica. *Classical and Quantum Gravity*, **21**, 3887 (2004).

D. Allan. Statistics of atomic frequency standards. *Proceedings of the IEEE*, **54**, 221 (1966).

D. W. Allan, N. Ashby and C. Hodge. The science of timekeeping. App. Note 1289, Hewlett Packard (1997).

J. Alnis, A. Matveev, N. Kolachevsky, T. Wilken, R. Holzwarth and T. W. Hänsch. Stable diode lasers for hydrogen precision spectroscopy. *The European Physical Journal Special Topics*, **163**, 89 (2008).

T. M. Atanackovic and A. Guran. *Theory of elasticity for scientists and engineers.* Springer (2000).

E. C. Beaty. Calculated electrostatic properties of ion traps. *Phys. Rev. A*, **33**, 3645 (1986a).

E. C. Beaty. Simple electrodes for quadrupole ion traps. *Journal of Applied Physics*, **61**, 2118 (1986b).

D. J. Berkeland, J. D. Miller, J. C. Bergquist, W. M. Itano and D. J. Wineland. Minimization of ion micromotion in a paul trap. *Journal of Applied Physics*, **83**, 5025 (1998).

J. W. Berthold III, S. F. Jacobs and M. A. Norton. Dimensional stability of fused silica, invar, and several ultra-low thermal expansion materials. *Metrologia*, **13**, 9 (1977).

H. R. Böhm, S. Gigan, F. Blaser, A. Zeilinger, M. Aspelmeyer, G. Langer, D. Bauerle, J. B. Hertzberg and K. C. Schwab. High reflectivity high-Q micromechanical bragg mirror. *Applied Physics Letters*, **89**, 223101 (2006).

R. L. Bisplinghoff, J. W. Mar and T. H. H. Pian. *Statics of Deformable Solids.* Courier Dover Publications (2002).

E. D. Black. An introduction to Pound–Drever–Hall laser frequency stabilization. *Am. J. Physics*, **69**, 79 (2001).

Bibliography

E. D. Black, A. Villar, K. Barbary, A. Bushmaker, J. Heefner, S. Kawamura, F. Kawazoe, L. Matone, S. Meidt, S. R. Rao, K. Schulz, M. Zhang and K. G. Libbrecht. Direct observation of broadband coating thermal noise in a suspended interferometer. *Physics Letters A*, **328**, 1 (2004).

P. Blythe. *Optical frequency measurement and ground state cooling of single trapped Yb$^+$ ions.* Ph.D. thesis, University of London (2005).

F. Bondu, P. Fritschel, C. N. Man and A. Brillet. Ultrahigh-spectral-purity laser for the VIRGO experiment. *Opt. Lett.*, **21**, 582 (1996).

F. Bondu, P. Helo and J.-Y. Vinet. Thermal noise in mirrors of interferometric gravitational wave antennas. *Physics Letters A*, **246**, 227 (1998).

V. B. Braginsky, M. L. Gorodetsky and S. P. Vyatchanin. Thermodynamical fluctuations and photo-thermal shot noise in gravitational wave antennae. *Physics Letters A*, **264**, 1 (1999).

V. B. Braginsky, V. P. Mitrofanov and V. I. Panov. *Systems with small dissipation.* University of Chicago Press (1986).

H. B. Callen and R. F. Greene. On a theorem of irreversible thermodynamics. *Physical Review*, **86**, 702 (1952).

H. B. Callen and T. A. Welton. Irreversibility and generalized noise. *Physical Review*, **83**, 34 (1951).

S. Chelkowski, S. Hild and A. Freise. Prospects of higher-order Laguerre-Gauss modes in future gravitational wave detectors. *Physical Review D*, **79**, 122002 (2009).

D. R. M. Crooks, G. Cagnoli, M. M. Fejer, G. Harry, J. Hough, B. T. Khuri-Yakub, S. Penn, R. Route, S. Rowan, P. H. Sneddon, I. O. Wygant and G. G. Yaralioglu. Experimental measurements of mechanical dissipation associated with dielectric coatings formed using SiO_2, Ta_2O_5 and Al_2O_3. *Classical and Quantum Gravity*, **23**, 4953 (2006).

D. R. M. Crooks, P. Sneddon, G. Cagnoli, J. Hough, S. Rowan, M. M. Fejer, E. Gustafson, R. Route, N. Nakagawa, D. Coyne, G. M. Harry and A. M. Gretarsson. Excess mechanical loss associated with dielectric mirror coatings on test masses in interferometric gravitational wave detectors. *Classical and Quantum Gravity*, **19**, 883 (2002).

E. D'Ambrosio. Nonspherical mirrors to reduce thermoelastic noise in advanced gravitational wave interferometers. *Physical Review D*, **67**, 102004 (2003).

E. D'Ambrosio, R. O'Shaugnessy, K. Thorne, P. Willems, S. Strigin and S. Vyatchanin. Advanced ligo: non-gaussian beams. *Classical and Quantum Gravity*, **21**, S867 (2004).

H. Dehmelt. Mono-ion oscillator as potential ultimate laser frequency standard. In: *Thirty Fifth Annual Frequency Control Symposium. 1981*, pp. 596 – 601 (1981).

L. Deslauriers, S. Olmschenk, D. Stick, W. K. Hensinger, J. Sterk and C. Monroe. Scaling and suppression of anomalous heating in ion traps. *Physical Review Letters*, **97**, 103007 (2006).

J. Dratler, Jr. A proportional thermostat with 10 microdegree stability. *Review of Scientific Instruments*, **45**, 1435 (1974).

R. W. P. Drever, J. L. Hall, F. V. Kowalski, J. Hough, G. M. Ford, A. J. Munley and H. Ward. Laser phase and frequency stabilization using an optical resonator. *Applied Physics B: Lasers and Optics*, **31**, 97 (1983).

G. Duffing. *Erzwungene Schwingungen bei veränderlicher Eigenfrequenz und ihre technische Bedeutung*. Vieweg (1918).

S. Earnshaw. On the nature of the molecular forces which regulate the constitution of the luminiferous ether. *Transactions of the Cambridge Philosophical Society*, **7**, 97 (1842).

R. H. Enns and G. McGuire. *Nonlinear physics with Mathematica for scientists and engineers*. Birkhäuser (2001).

M. E. Fine, H. V. Duyne and N. T. Kenney. Low-temperature internal friction and elasticity effects in vitreous silica. *Journal of Applied Physics*, **25**, 402 (1954).

J. Franzen, R.-H. Gabling, M. Schubert and Y. Wang. Nonlinear ion traps. In: R. E. March and J. F. J. Todd (eds.), *Fundamentals of ion trap mass spectrometry*, vol. 1 of *Practical aspects of ion trap mass spectrometry*, chap. 3, pp. 49–167. CRC Press, Boca Raton (1995).

A. Gillespie and F. Raab. Thermally excited vibrations of the mirrors of laser interferometer gravitational-wave detectors. *Physical Review D*, **52**, 577 (1995).

G. I. González and P. R. Saulson. Brownian motion of a mass suspended by an anelastic wire. *Journal of the Acoustical Society of America*, **96**, 207 (1994).

G. I. González and P. R. Saulson. Brownian motion of a torsion pendulum with internal friction. *Physics Letters A*, **201**, 12 (1995).

M. L. Gorodetsky. Thermal noises and noise compensation in high-reflection multilayer coating. *Physics Letters A*, **372**, 6813 (2008).

S. Gröblacher, S. Gigan, H. R. Böhm, A. Zeilinger and M. Aspelmeyer. Radiation-pressure self-cooling of a micromirror in a cryogenic environment. *Europhysics Letters*, **81**, 54003 (2008).

Bibliography

R. F. Greene and H. B. Callen. On a theorem of irreversible thermodynamics II. *Physical Review*, **88**, 1387 (1952).

G. M. Harry, M. R. Abernathy, A. E. Becerra-Toledo, H. Armandula, E. Black, K. Dooley, M. Eichenfield, C. Nwabugwu, A. Villar, D. R. M. Crooks, G. Cagnoli, J. Hough, C. R. How, I. MacLaren, P. Murray, S. Reid, S. Rowan, P. H. Sneddon, M. M. Fejer, R. Route, S. D. Penn, P. Ganau, J.-M. Mackowski, C. Michel, L. Pinard and A. Remillieux. Titania-doped tantala/silica coatings for gravitational-wave detection. *Classical and Quantum Gravity*, **24**, 405 (2007).

G. M. Harry, H. Armandula, E. Black, D. R. M. Crooks, G. Cagnoli, J. Hough, P. Murray, S. Reid, S. Rowan, P. Sneddon, M. M. Fejer, R. Route and S. D. Penn. Thermal noise from optical coatings in gravitational wave detectors. *Appl. Opt.*, **45**, 1569 (2006).

G. M. Harry, A. M. Gretarsson, P. R. Saulson, S. E. Kittelberger, S. D. Penn, W. J. Startin, S. Rowan, M. M. Fejer, D. R. M. Crooks, G. Cagnoli, J. Hough and N. Nakagawa. Thermal noise in interferometric gravitational wave detectors due to dielectric optical coatings. *Classical and Quantum Gravity*, **19**, 897 (2002).

J. Horn. *Gewöhnliche Differentialgleichungen beliebiger Ordnung.* Göschen (1905).

K. Hosaka, S. A. Webster, A. Stannard, B. R. Walton, H. S. Margolis and P. Gill. An optical frequency standard based on the electric octupole transition in $^{171}yb^+$. *Physical Review A*, **79**, 033403 (2009).

W. M. Itano, J. C. Bergquist, J. J. Bollinger, J. M. Gilligan, D. J. Heinzen, F. L. Moore, M. G. Raizen and D. J. Wineland. Quantum projection noise: Population fluctuations in two-level systems. *Phys. Rev. A*, **47**, 3554 (1993).

H. Katori, M. Takamoto, V. G. Pal'chikov and V. D. Ovsiannikov. Ultrastable optical clock with neutral atoms in an engineered light shift trap. *Phys. Rev. Lett.*, **91**, 173005 (2003).

H. Kogelnik and T. Li. Laser beams and resonators. *Applied Optics*, **5**, 1550 (1966).

L. D. Landau and E. M. Lifshitz. *Theory of elasticity.* Elsevier, 3rd edn. (1986).

Y. Levin. Internal thermal noise in the LIGO test masses: A direct approach. *Physical Review D*, **57**, 659 (1997).

Y. T. Liu and K. S. Thorne. Thermoelastic noise and homogeneous thermal noise in finite sized gravitational-wave test masses. *Physical Review D*, **62**, 122002 (2000).

G. Lovelace. The dependence of test-mass thermal noises on beam shape in gravitational-wave interferometers. *Classical and Quantum Gravity*, **24**, 4491 (2007).

F. G. Major, V. N. Gheorghe and G. Werth. *Charged Particle Traps.* Springer (2005).

R. E. March and J. F. J. Todd (eds.). *Practical Aspects of Ion Trap Mass Spectrometry*, vol. I. CRC Press (1995).

E. Mathieu. Mémoire sur le mouvement vibratoire d'une membrane de forme elliptique. *Journal de Mathématiques Pures et Appliquées*, **13**, 111 (1868).

N. Matsumoto, T. Ando, T. Inoue, Y. Ohtake, N. Fukuchi and T. Hara. Generation of high-quality higher-order laguerre-gaussian beams using liquid-crystal-on-silicon spatial light modulators. *Journal of the Optical Society of America A*, **25**, 1642 (2008).

N. W. McLachlan. *Theory and application of Mathieu functions*. Clarendon Press (1951).

J. Meixner and F. W. Schäfke. *Mathieusche Funktionen und Sphäroidfunktionen*. Springer (1954).

B. Mours, E. Tournefier and J.-Y. Vinet. Thermal noise reduction in interferometric gravitational wave antennas: using high order TEM modes. *Classical and Quantum Gravity*, **23**, 5777 (2006).

N. Nakagawa, A. M. Gretarsson, E. K. Gustafson and M. M. Fejer. Thermal noise in half-infinite mirrors with nonuniform loss: A slab of excess loss in a half-infinite mirror. *Physical Review D*, **65**, 102001 (2002).

R. Nawrodt, A. Zimmer, T. Koettig, C. Schwarz, D. Heinert, M. Hudl, R. Neubert, M. Thürk, S. Nietzsche, W. Vodel, P. Seidel and A. Tünnermann. High mechanical q-factor measurements on silicon bulk samples. *Journal of Physics: Conference Series*, **122**, 012008 (2008).

T. Nazarova. *Towards the quantum noise limit in Ramsey-Bordé atom interferometry*. Ph.D. thesis, Universität Hannover (2007).

M. Notcutt, L.-S. Ma, A. D. Ludlow, S. M. Foreman, J. Ye and J. L. Hall. Contribution of thermal noise to frequency stability of rigid optical cavity via Hertz-linewidth lasers. *Physical Review A*, **73**, 031804 (2006).

A. S. Nowick and B. S. Berry. *Anelastic relaxation in crystalline solids*. Academic Press (1972).

K. Numata. *Direct measurement of the mirror thermal noise*. Ph.D. thesis, University of Tokyo (2002).

K. Numata, M. Ando, K. Yamamoto, S. Otsuka and K. Tsubono. Wide-band direct measurement of thermal fluctuations in an interferometer. *Physical Review Letters*, **91**, 260602 (2003).

K. Numata, A. Kemery and J. Camp. Thermal-noise limit in the frequency stabilization of lasers with rigid cavities. *Physical Review Letters*, **93**, 250602 (2004a).

Bibliography

K. Numata, K. Yamamoto, H. Ishimoto, S. Otsuka, K. Kawabe, M. Ando and K. Tsubono. Systematic measurement of the intrinsic losses in various kinds of bulk fused silica. *Physics Letters A*, **327**, 263 (2004b).

R. O'Shaughnessy. A note on coating thermal noise for arbitrary-shaped beams. *Classical and Quantum Gravity*, **23**, 7627 (2006).

R. O'Shaughnessy, S. Strigin and S. Vyatchanin. The implications of Mexican-hat mirrors: calculations of thermoelastic noise and interferometer sensitivity to perturbation for the Mexican-hat-mirror proposal for advanced LIGO. *Physical Review D* (2004). Submitted, as yet unpublished. arXiv:gr-qc/0409050v1.

W. Paul. Electromagnetic traps for charged and neutral particles. *Reviews of Modern Physics*, **62**, 531 (1990).

W. Paul, E. Fischer and O. Osberghaus. *Ein Ionenkäfig*. Forschungsberichte des Wirtschafts- und Verkehrsministeriums Nordrhein-Westfalen (1958).

S. D. Penn, A. Ageev, D. Busby, G. M. Harry, A. M. Gretarsson, K. Numata and P. Willems. Frequency and surface dependence of the mechanical loss in fused silica. *Physics Letters A*, **352**, 3 (2006).

C. Salomon, D. Hils and J. L. Hall. Laser stabilization at the millihertz level. *J. Opt. Soc. Am. B*, **5**, 1576 (1988).

G. Santarelli, P. Laurent, P. Lemonde, A. Clairon, A. G. Mann, S. Chang, A. N. Luiten and C. Salomon. Quantum projection noise in an atomic fountain: A high stability cesium frequency standard. *Phys. Rev. Lett.*, **82**, 4619 (1999).

D. Sarid and D. S. Cannell. A ±15 microdegree temperature controller. *Review of Scientific Instruments*, **45**, 1082 (1974).

P. R. Saulson. Thermal noise in mechanical experiments. *Physical Review D*, **42**, 2437 (1990).

T. Schneider. *Optical Frequency Standard with a Single $^{171}Yb^+$ Ion*. Ph.D. thesis, Universität Hannover (2005).

C. A. Schrama, E. Peik, W. W. Smith and H. Walther. Novel miniature ion traps. *Optics Communications*, **101**, 32 (1993).

I. Sherstov, M. Okhapkin, B. Lipphardt, C. Tamm and E. Peik. Diode-laser system for high-resolution spectroscopy of the $^2S_{1/2} \rightarrow {}^2F_{7/2}$ octupole transition in $^{171}Yb^+$. *Phys. Rev. A*, **81**, 021805 (2010).

H. Stoehr. *Diodenlaser mit Hertz-Linienbreite für ein optisches Calcium-Frequenznormal*. Ph.D. thesis, Universität Hannover (2005).

H. Straubel. Zum Öltröpfchenversuch von Millikan. *Die Naturwissenschaften*, **18**, 506 (1955).

J. E. P. Syka. Commercialization of the quadrupole ion trap. In: R. E. March and J. F. J. Todd (eds.), *Fundamentals of ion trap mass spectrometry*, vol. 1 of *Practical aspects of ion trap mass spectrometry*, chap. 4, pp. 169–205. CRC Press, Boca Raton (1995).

M. G. Tarallo, J. Miller, J. Agresti, E. D'Ambrosio, R. DeSalvo, D. Forest, B. Lagrange, J. M. Mackowsky, C. Michel, J. L. Montorio, N. Morgado, L. Pinard, A. Remilleux, B. Simoni and P. Willems. Generation of a flat-top laser beam for gravitational wave detectors by means of a nonspherical Fabry-Perot resonator. *Applied Optics*, **46**, 6648 (2007).

I. Tittonen, G. Breitenbach, T. Kalkbrenner, T. Müller, R. Conradt, S. Schiller, E. Steinsland, N. Blanc and N. F. de Rooij. Interferometric measurements of the position of a macroscopic body: Towards observation of quantum limits. *Physical Review A*, **59**, 1038 (1999).

P. K. M. Unni, M. K. Gunasekaran and A. Kumar. $\pm$ 30 µK temperature controller from 25 to 103 °C: Study and analysis. *Review of Scientific Instruments*, **74**, 231 (2003).

J.-Y. Vinet. Mirror thermal noise in flat-beam cavities for advanced gravitational wave interferometers. *Classical and Quantum Gravity*, **22**, 1395 (2005).

S. Vyatchanin. FDT approach calculations of Brownian noise in thin layer. Tech. Rep. T040242-00-Z, LIGO (2004).

S. Weyers, B. Lipphardt and H. Schnatz. Reaching the quantum limit in a fountain clock using a microwave oscillator phase locked to an ultrastable laser. *Phys. Rev. A*, **79**, 031803 (2009).

P. Willems and D. Bushy. Report to the April 25, 2003 Core optics downselect committee meeting. Tech. Rep. T030087-00-R, LIGO (2003).

K. Yamamoto, M. Ando, K. Kawabe and K. Tsubono. Thermal noise caused by an inhomogeneous loss in the mirrors used in the gravitational wave detector. *Physics Letters A*, **305**, 18 (2002).

B. C. Young, F. C. Cruz, W. M. Itano and J. C. Bergquist. Visible lasers with subhertz linewidths. *Phys. Rev. Lett.*, **82**, 3799 (1999).

C. Zener. Internal friction in solids. *Physical Review*, **52**, 230 (1937).

C. Zener. *Elasticity and anelasticity of metals.* University of Chicago Press (1948).

O. C. Zienkiewicz, C. Emson and P. Bettess. A novel boundary infinite element. *International Journal for Numerical Methods in Engineering*, **19**, 393 (1983).

List of Publications

Articles in Refereed Journals

C. Gohle, B. Stein, A. Schliesser, T. Udem and T. W. Hänsch. Frequency comb vernier spectroscopy for broadband, high-resolution, high-sensitivity absorption and dispersion spectra. *Physical Review Letters*, **99**, 263902 (2007).

D. R. Walker, T. Udem, C. Gohle, B. Stein and T. W. Hänsch. Frequency dependence of the fixed point in a fluctuating frequency comb. *Applied Physics B: Lasers and Optics*, **89**, 535 (2007).

Conference Proceedings

J. Rauschenberger, A. Ozawa, C. Gohle, B. Stein, R. Graf, A. Fernandez, A. Apolonski, T. Udem, F. Krausz and T. W. Hänsch. Enhancement resonators for frequency combs. In: *Lasers and Electro-Optics Society, LEOS 2006 (IEEE Conference Proceedings)*, pp. 64–65. IEEE (2006).

I. Sherstoy, C. Tamm, B. Stein, B. Lipphardt, H. Schnatz, R. Wynands, S. Weyers, T. Schneider and E. Peik. ^{171}Yb$^+$ single-ion optical frequency standards. In: *Proceedings of the 2007 IEEE International Frequency Control Symposium—Jointly with the 21st European Frequency and Time Forum*, pp. 405–406. IEEE (2007).

E. Peik, B. Lipphardt, H. Schnatz, I. Sherstov, B. Stein, C. Tamm, S. Weyers and R. Wynands. ^{171}Yb$^+$ single-ion optical frequency standards and search for variations of the fine structure constant. In: *Quantum-Atom Optics Downunder*. Optical Society of America (2007). Paper QTuD4.

C. Tamm, B. Lipphardt, T. E. Mehlstaeubler, M. Okhapkin, I. Sherstov, B. Stein and E. Peik. ^{171}Yb$^+$ single-ion optical frequency standards. In: L. Maleki (ed.), *Proceedings of the 7th Symposium Frequency Standards and Metrology*, pp. 235–240. World Scientific (2009).

B. Stein, T. E. Mehlstäubler, I. Sherstov, M. Okhapkin, B. Lipphardt, C. Tamm and E. Peik. High-order modes for reference cavities in optical clocks. In: *Verhandlungen der deutschen physikalischen Gesellschaft*, vol. 44, 6 (2009). Talk Q 24.9.

Invited Talk

B. Stein, T. Mehlstäubler, I. Sherstov, M. Okhapkin, B. Lipphardt, C. Tamm and E. Peik. Ytterbium single-ion optical clock. Symposium for young researchers: Quantum manipulation of atoms and photons. Beijing and Shanghai, October 14–22 (2008).

Poster Presentations

C. Gohle, A. Ozawa, J. Rauschenberger, B. Stein, M. Herrmann, R. Holzwarth, A. Fernandez, A. Apolonskiy, F. Krausz, T. Udem and T. W. Hänsch. Extreme ultraviolet frequency comb. Implementation and results. 16. Norddeutscher Lasertag. Hannover, December 6th (2006).

B. Lipphardt, E. Peik, H. Schnatz, T. Schneider, I. Sherstov, B. Stein and C. Tamm. Search for a temporal variation of the fine structure constant in optical frequency comparisons. 16. Norddeutscher Lasertag. Hannover, December 6th (2006).

B. Lipphardt, E. Peik, H. Schnatz, T. Schneider, I. Sherstov, B. Stein and C. Tamm. ^{171}Yb$^+$ single-ion optical frequency standards. Atomic Clocks and Fundamental Constants. 388. WE-Heraeus-Seminar. Bad Honnef, June 4th–June 7th (2007).

B. Lipphardt, E. Peik, H. Schnatz, T. Schneider, I. Sherstov, B. Stein and C. Tamm. ^{171}Yb$^+$ single-ion optical frequency standards. Optical Supercontinua and Frequency Combs. International Wilhelm and Else Heraeus Summerschool. Wittemberg, June 24th–July 5th (2007).

B. Stein, T. Mehlstäubler, I. Sherstov, M. Okhapkin, B. Lipphardt, C. Tamm and E. Peik. ^{171}Yb$^+$ single-ion optical frequency standards. Modern Applications of Trapped Ions. Les Houches, May 18th–23rd (2008).

B. Stein, T. Mehlstäubler, I. Sherstov, M. Okhapkin, B. Lipphardt, C. Tamm and E. Peik. ^{171}Yb$^+$ single-ion optical frequency standards. Summer School of Metrology. Braunschweig International Graduate School of Metrology. Goslar, September 1st–4th (2008).

B. Stein, B. Lipphardt, T. Mehlstäubler, M. Okhapkin, T. Schneider, I. Sherstov, C. Tamm and E. Peik. Ytterbium single-ion optical frequency standards. International Symposium for Young Researchers: Quantum Manipulation of Photons and Atoms. Beijing and Shanghai, October 14th–22nd (2008).

Curriculum Vitae

28.01.1979	Birth in Salzgitter, Germany. Parents: Erika and Siegfried Stein.
01.07.1986–30.06.1990	Grundschule Othfresen. Gemeinde Liebenburg, Germany
01.07.1990–30.06.1992	Orientierungsstufe Liebenburg. Liebenburg, Germany
01.07.1992–30.06.1996	Christian-von-Dohm Gymnasium Goslar. Goslar, Germany
01.07.1996–30.06.1997	Berkshire School. Berkshire, MA, USA
01.07.1997–29.06.1999	JCS Braunschweig, Germany. Graduation: Abitur.
01.06.1999–31.07.2002	Fraunhofer Institut and TU Braunschweig. Scientific Assistant.
01.07.1999–30.04.2000	German Airforce. Grundwehrdienst (mandatory military service).
15.10.1999–08.11.2006	LMU München, Germany. Graduation: Diplomphysiker.
01.02.2002–30.11.2002	University of Queensland, Brisbane, Australia. Exchange student with DAAD scholarship.
15.11.2006–30.06.2009	Universität Hannover. Scientific Employee.
01.07.2009–31.07.2009	Physikalisch-Technische Bundesanstalt, Braunschweig, Germany. Scientific Employee.
Since 01.10.2010	University of Sussex.